

# **Optical Wire Antennas: Near-Field Imaging, Modeling and Emission Patterns**

THÈSE N° 4707 (2010)

PRÉSENTÉE LE 30 SEPTEMBRE 2010

À LA FACULTÉ SCIENCES DE BASE

LABORATOIRE DE SCIENCE À L'ÉCHELLE NANOMÉTRIQUE

PROGRAMME DOCTORAL EN PHYSIQUE

ÉCOLE POLYTECHNIQUE FÉDÉRALE DE LAUSANNE

POUR L'OBTENTION DU GRADE DE DOCTEUR ÈS SCIENCES

PAR

**Jens DORFMUELLER**

acceptée sur proposition du jury:

Prof. N. Grandjean, président du jury

Prof. K. Kern, directeur de thèse

Dr A. Dmitriev, rapporteur

Prof. B. Hecht, rapporteur

Prof. O. Martin, rapporteur



ÉCOLE POLYTECHNIQUE  
FÉDÉRALE DE LAUSANNE

Suisse  
2010



## Abstract

In this thesis we study the properties of optical wire antennas. As experimental method for our investigations we use apertureless near-field optical microscopy. This technique achieves high spatial resolution well beyond the diffraction limit by utilizing the field enhancement at the apex of sharp tips. An interferometric measurement scheme allows us to detect both near-field intensity and optical phase. By using s-polarized light for illumination and detecting the p-polarized component of the backscattered light we are able to map the z-component of the electrical near-field. Optimizing polarizer and analyzer angles of our cross-polarization scheme ensures a background free plasmonic eigenmode mapping. By comparison with simulation data not including the tip we show that the measurement has little to no influence on the eigenmode.

The samples investigated in this thesis are arrays of gold nano-wires prepared by electron beam lithography. We observe plasmon resonances in our near-field images as patterns of lobes and explain them by regarding the wires as one dimensional Fabry-Pérot resonators. The number of nodes in between the lobes is the resonance order. From eigenmodes well beyond quadrupolar order we extract both, propagation constant and reflection phase of the guided surface plasmon polariton with superb accuracy. The combined symmetry breaking effects of oblique illumination and retardation allow the excitation of dipole forbidden even-order resonances. By systematically varying the azimuthal illumination angle we are able to map the directional receiving and emission patterns of the wire antennas.

In order to understand these patterns we develop an analytical model. In contrast to radio frequency (RF) antenna theories we not only assume surface currents but also take volume currents into account. The model also allows us to spotlight the differences between plasmonic and RF antennas. The equations we derive describe both, the property of the wires as resonators as well as the antenna emission / reception patterns. With just four — physically motivated — parameters we are able to fit measured as well as simulated data astonishingly well. With this model

predicting the relative intensity and phase of the light absorbed and scattered by nano-wire antennas it has great potential for future research.

**Keywords** apertureless scanning near-field microscopy; optical antennas; near-field optics; plasmonics; scanning probe microscopy; radiation patterns; Fabry-Pérot resonators; interferometric detection; theoretical model;

## **Zusammenfassung**

Diese Arbeit beschäftigt sich mit den Eigenschaften linearer optischer Antennen. Wir untersuchen sie dazu mit aperturloser, nahfeldoptischer Mikroskopie, einer Technik, die durch Ausnutzung des Feldverstärkungseffekts am Apex einer scharfen Spitze eine sehr hohe laterale Auflösung weit jenseits des optischen Beugungslimits erreicht. Ein interferometrisches Messverfahren ermöglicht sowohl die Nahfeldintensität als auch die optische Phase zu messen. Durch Beleuchtung mit s-polarisiertem Licht und Detektion der p-polarisierten Komponente des zurückgestreuten Lichtes können wir die senkrechte Feldkomponente des elektrischen Nahfeldes abbilden. Durch Optimierung der Polarisator und Analysator Stellung in unserer Kreuzpolarisationstechnik eliminieren wir störende Hintergrundsignale aus unseren Eigenmodenabbildungen. Durch Vergleiche mit Simulationen, die die Messspitze außer Acht lassen, zeigen wir, dass unsere Messmethode kaum Einfluss auf die Eigenmoden hat.

Bei den untersuchten Proben handelt es sich um Goldnanodraht-Arrays die durch Elektronenstrahllithographie hergestellt wurden. In unseren Nahfeldbildern können wir die Schwingungsbäuche der Plasmonresonanzen direkt beobachten. Die Resonanzen lassen sich verstehen indem man die Drähte als eindimensionale Fabry-Pérot Resonatoren beschreibt. Die Resonanzordnung ist gegeben durch die Anzahl der Knoten zwischen den Bäuchen. Aus Resonanzen weit jenseits der Quadrupol-Mode bestimmen wir sowohl die Propagationskonstante als auch die Reflektionsphase des geleiteten Oberflächenplasmons. Die Brechung der Beleuchtungssymmetrie durch einen streifenden Einfall des Lichtes und durch Retardationseffekte ermöglicht es auch Resonanzmoden anzuregen die eigentlich Dipol-verboten sind. Durch systematisches variieren des Beleuchtungswinkels gelingt es uns die Empfangs- und Sendecharakteristik der Drahtantennen zu bestimmen.

Um diese Charakteristiken besser zu verstehen entwickeln wir ein analytisches Modell. Während Radiofrequenz-Antennentheorien nur Oberflächenströme berücksichtigen, geht unsere Theorie von Volumenströmen aus. Die Gleichungen beschreiben sowohl die Resonatoreigenschaften als auch die Antenneneigenschaften der Drähte korrekt. Mit nur vier, physikalisch motivierten, Parametern gelingt es uns sowohl gemessene als auch simulierte Daten zu fitten. Das Modell erlaubt uns auch die

Unterschiede zwischen Radiofrequenzantennen und plasmonischen Antennen klar abzugrenzen. Da die Theorie sowohl die relative Intensität als auch die Phase von an Nano-Drähten gestreutem Licht vorhersagen kann, hat sie viel Potential für die zukünftige Forschung.

**Schlagwörter** aperturlose, nahfeldoptische Mikroskopie; optische Antennen; Nahfeldoptik; Plasmonik; Rastersondenmikroskopie; Richtcharakteristik; Fabry-Pérot Resonatoren; interferometrische Detektion; theoretisches Modell;

# Contents

<b>Abstract</b>	<b>iii</b>
<b>Zusammenfassung</b>	<b>v</b>
<b>1. Introduction</b>	<b>1</b>
1.1. Development of Antennas . . . . .	1
1.2. Potential of Optical Antennas . . . . .	2
1.3. Design of Optical Antennas . . . . .	4
1.4. Microscopy Methods . . . . .	5
<b>2. Cross-Polarized apertureless Scanning Near-Field Optical Microscopy</b>	<b>9</b>
2.1. Working Principle of apertureless SNOM . . . . .	9
2.1.1. Higher Harmonic Detection . . . . .	10
2.1.2. Interferometric Amplification . . . . .	11
2.1.3. Homodyne Amplification . . . . .	12
2.1.4. Confocal Microscope . . . . .	14
2.2. Cross-Polarization aSNOM . . . . .	15
2.2.1. Principle . . . . .	17
2.2.2. Michelson vs. Mach-Zehnder Interferometer . . . . .	17
2.2.3. Weak Tips . . . . .	18
2.3. Implementation . . . . .	19
2.4. Alignment . . . . .	21
2.4.1. Finding the Focus . . . . .	21
2.4.2. Polarization Scan . . . . .	22
2.4.3. Cross Polarized Focus Scan . . . . .	22
2.5. Eliminating the Residual Background Artefact in Cross-Polarized aSNOM . . . . .	25

2.5.1.	Description of the Artefact . . . . .	25
2.5.2.	Explanation of the Artefact . . . . .	26
2.5.3.	Correction of the Artefact . . . . .	28
<b>3.</b>	<b>Plasmonic Resonances of Gold Nano-Wires</b>	<b>31</b>
3.1.	Wire Array Sample . . . . .	32
3.2.	Simulations . . . . .	35
3.3.	Odd Order Resonances . . . . .	35
3.3.1.	Near-Field Images . . . . .	35
3.3.2.	Resonance-Length Dependence . . . . .	38
3.3.3.	Reflection Phase . . . . .	39
3.4.	Even Order Resonances . . . . .	40
3.4.1.	Breaking the Symmetry of the Illumination . . . . .	40
3.4.2.	The Second Order Mode . . . . .	42
<b>4.</b>	<b>Emission Patterns of Linear Plasmonic Antennas</b>	<b>45</b>
4.1.	Angle Dependent Measurements . . . . .	46
4.2.	Analytical Model to Describe the Wire Excitation . . . . .	49
4.2.1.	Illuminating Field . . . . .	51
4.2.2.	Field Generated by the Induced Current . . . . .	53
4.2.3.	Fields Inside of the Wire . . . . .	55
4.2.4.	Solving the Equations . . . . .	58
4.2.5.	Perpendicular Component of the E-Field . . . . .	60
4.3.	Applying the Model to Experimental Results . . . . .	60
4.3.1.	Near-Field Images . . . . .	61
4.3.2.	Geometric Resonances . . . . .	64
4.3.3.	Simulation Data . . . . .	67
4.3.4.	Experimental Data . . . . .	71
4.4.	Difference Between Normal and Plasmonic Antennas . . . . .	77
<b>5.</b>	<b>Summary and Outlook</b>	<b>87</b>
5.1.	Summary . . . . .	87
5.2.	Outlook . . . . .	88
5.2.1.	Antenna Arrays . . . . .	89
5.2.2.	Nonlinear Plasmonics . . . . .	90

5.2.3. Coupling Between Antennas . . . . .	91
<b>A. Consideration of the Experimental Situation</b>	<b>93</b>
A.1. Coordinate Transformation . . . . .	94
A.2. Projection of the Polarization Vector . . . . .	96
<b>B. Emission Pattern of an Infinite Thin Wire</b>	<b>99</b>
<b>Bibliography</b>	<b>105</b>
<b>Curriculum Vitae</b>	<b>119</b>
<b>Publications</b>	<b>121</b>



# Chapter 1.

## Introduction

### 1.1. Development of Antennas

At the end of the 19th century scientists started conducting first experiments with antennas [1]. It took several years until they learned how the design of an antenna influences characteristics such as the directivity of the antenna's emittance and reception. In the 1920s, by combining simple dipole antennas [2], with their relatively broad directivity and small bandwidth, Yagi and Uda developed the classic TV antenna with its narrow directivity [3]. For other purposes other antenna designs are advantageous, e. g. a bowtie antenna [4, 5] with a large emission angle and a large frequency bandwidth.

The detailed knowledge about antenna design and how it influences the bandwidth and emission pattern lead to tremendous technological advances. The wide distribution of radio transmitters and receivers in the 1930s and the success of television would not have been possible without antennas. Nowadays, antenna design is a standard discipline in electrical engineering and is indispensable in our lives. They

continue to be optimized for mobile phones or wireless computer networks and have become cornerstones of our modern information society.

The principle design parameter of an antenna is its size. To be in resonance with the electromagnetic waves it is supposed to receive or transmit it should be approximately of the size of the wavelength. The fact that the antenna in a mobile phone is much smaller than a rooftop television antenna stems from the usage of shorter wavelengths. The advantage of shorter wavelengths and corresponding higher carrier frequencies is the possibility to transmit more information per time.

The technical advancement of the last decades made it possible to manufacture smaller and smaller structures. With the development of nanotechnology various methods (i. e. the chemical growth [6,7], the focussed ion beam milling (FIB) [8,9] or the electron beam (e-beam) lithography [10]) made it possible to fabricate antennas small enough to shift their resonance wavelength into the part of the electromagnetic spectrum we usually refer to as light [11,12]. Today, these new antennas are often called “optical antennas” [13,14].

## **1.2. Potential of Optical Antennas**

Although these nanoscopic antennas have been under research for less than a decade and some of their properties are not yet fully understood, these nanoscopic antennas have the same potential to open the door to a complete new technology as their macroscopic counterparts 100 years ago. The capability of optical antennas to collect light and to concentrate it to certain regions [15,16] has fired the imagination of scientists.

The combination of antennas with atoms or molecules [17] might give rise to completely new (quantum-) sensing applications [18–22]. The proposed cheap, reusable,

molecule specific recognition schemes which are supposed to be able to detect even a few molecules would give rise to new technologies. For these applications the antennas need to be designed to have a low loss and their resonance tuned to the atoms / molecules of interest.

Already in clinical trials are nano-antennas as heat concentrating agents in cancer treatment [23]. Here, gold nano-shells are used as antennas and are brought into cancer cells. The absorption of near-infrared light by the shells leads to heating and finally to photothermally induced necrosis of the cancerous cell. The beauty of this technique is that the selective accumulation of nano shells in the cancer cell [24,25] in combination with focussed illumination leads to a very high specificity. The reason the nano shells have been chosen as antennas is their tunable, high absorption for an efficient heating.

The building blocks of meta-materials can also be regarded as nano-antennas. These two or three dimensional assemblies of metal nano structures can lead to new kinds of materials. While the electromagnetic properties of normal matter are dictated by the properties of the atoms and molecules they are made of, meta-materials allow an engineering of their building blocks. It has already been shown that it is possible to achieve negative refraction [26] and bending of light rays around obstacles [27]. Especially the last experiment got huge public attention and is often compared with Harry Potter's invisibility cloak [28, 29]. For meta-materials the design of the individual antenna is very important. It is dictated by the effective refractive index of the final meta-material.

### 1.3. Design of Optical Antennas

But what methods are there to design optical antennas? Can we apply the old antenna design rules from the radio frequency (RF) regime to the new, the optical regime? It turns out that it is actually not that simple. While RF antennas have their fundamental resonance when the antenna length is equal to half the wavelength, we will show in the following chapters that optical antennas are much shorter. This means that for optical antennas standard RF antenna theories can not be applied anymore. We need an improved model to describe them.

Why does the simple scaling down of antennas lead to new physics when the resonances lie in the optical regime? In the RF regime, metals can be regarded as perfect conductors with an infinitely large negative permittivity  $\epsilon$ . In the optical regime  $\epsilon$  is far from being infinite, instead it is a finite, complex valued number depending strongly on the exciting wavelength [30, 31]. This has a severe effect on the surface waves at the boundaries of the metal—dielectric interface. The dispersion relation of plasmons [32–34] tells us that the wavelengths of the excitation modes on the surfaces will be smaller than the free space wavelength. This has to be taken into account when we develop a new analytical description for optical antennas.

Today, the influence of the design of nano antennas on their optical properties is mainly studied by simulations. It has been very helpful that Maxwells equations are still valid at this length scale. Standard simulation methods, which have originally been designed for macroscopic antennas, can still be used in this new regime. For example, the finite-difference time-domain (FDTD) [35] method, invented in the 1970s, is still very helpful in understanding the properties of optical antennas [20, 36, 37].

Nevertheless, simulations are no substitute for an analytical model. Each simula-

tion can predict the behavior of a single sample. A systematic covering of large areas of the parameter space leads easily to very time consuming calculations and only gives the possibility to interpolate to the parameters in between the simulations. For a full physical understanding of optical antennas we desire simple formulas that can describe the excitability, the near-field patterns and the emission of radiation of optical antennas. On the one hand these equations can speed up the calculations on the other hand they allow extrapolation to new parameter sets [38]. In the end they will then help us to find the best optical antenna for each application. For the basic linear antenna we will do that in this thesis.

## 1.4. Microscopy Methods

While simulations are extremely helpful during the design process of an antenna, their prediction can only be as good as the experimentally determined parameters they rely on. The optical constants are usually obtained from experiments on bulk, crystalline metals. In contrast, the gold nano structures that are produced today are often polycrystalline or contaminated by other materials. Also, the small size of the particles results in a different proportion between volume and surface. It has, for example, been observed that the surface damping in small particles is much stronger and has to be accounted for in simulations [39–42]. This makes it necessary to validate the theoretical findings experimentally.

A common method to investigate the optical properties of small metal structures is to do spectroscopy on ensembles [43–45]. In these experiments the results are an average over a large amount of similar but not identical particles. Microscopy investigations of single particles have the advantage that spectroscopic features are not smeared out by small shape variations in the ensemble [7, 46].

By using nonlinear optical effects it is even possible to obtain some information about the strong near-fields around the antennas with conventional microscopes [12, 47]. The limitation of these confocal microscopy techniques is the Abbe diffraction limit on spatial resolution [48]. In order to distinguish two neighboring points in an optical far-field microscope, their distance has to be at least approximately half a wavelength. With the length of the first resonance of an optical dipole antenna being smaller than  $\lambda_{\text{vac}}/2$ , these techniques only allow an averaging over a single antenna.

To obtain higher resolution information on the optical properties of metal structures other methods are necessary. One possibility is to use electrons for detection. In electron energy loss spectroscopy (EELS) electrons passing the metal structures are losing some of their energy to surface plasmons [49, 50]. In imaging mode it is possible to map the plasmon excitability with the resolution of an electron microscope. It is not yet fully understood, though, what optical property the measured signal resembles. In some publications EELS is found to directly render the photonic local density of states (optical LDOS) [51, 52], while others do not find a direct link between EELS and LDOS maps [53].

Photoemission electron microscopy (PEEM) is an easier to understand technique. The local field enhancement of antenna structures leads to a higher photoelectron emission [54–56]. The local number of emitted electrons is depending on to the interference between the plasmon and the illumination field. The detection with electron optics allows a high resolution mapping of the near-field pattern around the antenna. The interpretation of the signal depends whether a single or two-photon process is used to overcome the work function of the metal [57].

All optical investigations have the advantage of being less stringent on the sample's

ambient conditions. No vacuum is necessary and most of the optics can be bought off-the-shelf. To achieve a high resolution, the illumination or the detection have to happen in the near-field region of the antennas. The origin of near-field microscopy goes back to an idea of Synge in the 1930s [58], but only in the 1980s it became possible to build such a scanning near-field optical microscopes (SNOM). A small aperture in an otherwise opaque metal film is used to confine the transmitted light [59–61].

The aperture SNOM was not Synge’s initial idea for a near-field microscope. At first, he wanted to use a small metal particle as local scatter to enhance the resolution [62, 63]. This idea is similar to what became the apertureless SNOM (aSNOM) [64–66]. Both methods, SNOM and apertureless SNOM, break the diffraction limit and can be used to map localized surface plasmons [67–73]. Both methods, though, suffer from the problem that the probing tip will influence the measurement process. The proximity of the tip to the investigated antenna will always modify the mapped eigenmode. For reliable experimental information it is necessary to minimize the influence of the probe.

In this thesis we will show how to use an aSNOM to map the local fields of optical antenna eigenmodes with minimal disturbance. In addition to the usual signal discrimination methods of tip–sample distance modulation and higher harmonic detection we use a cross-polarization scheme which allows us to obtain background free images of one of the E-field components. The comparison with simulation data (not including the tip) will show little to no deviation from our aSNOM experiment. This makes the cross-polarized aSNOM to a valuable tool for future research on plasmonics and near-field optics.

We investigate the basic structure of a wire antenna in great detail. Our investi-

gation of the length dependence of the resonance confirms theoretical models where the optical wire antenna is described by two parameters, a propagation constant and a reflection phase at the wire end. With these conclusions in mind, we continue to study the emission patterns of the wire antennas. In order to understand our findings we come up with a new theoretical model describing the resonances and the emission of plasmonic antennas. Compared to simulations and experimental data obtained until today, our analytical model gives us a broad understanding of linear antennas. The differences we find compared to normal antennas can now be explained by the material properties of metals in the optical regime.

## **Chapter 2.**

# **Cross-Polarized apertureless Scanning Near-Field Optical Microscopy**

We start this chapter with a review of the working principle of aSNOM. After this short review we concentrate on an improvement extending this well established technique to surface plasmon eigenmodes.

### **2.1. Working Principle of apertureless SNOM**

In order to achieve a resolution better than the diffraction limit, near-field techniques rely on a local field confinement. While SNOM uses apertures with diameters on the order of a tenth of the wavelength to block all light except for a small region, apertureless SNOM uses sharp tips as antennas to confine light to possibly even smaller volumes. This light confinement can be observed in simulations of elongated

tips illuminated with light [74, 75]. Experimentally, the field enhancement has been verified with the help of photosensitive polymer films [76, 77]. The lateral dimension of the field enhancement region at the tip apex is on the order of magnitude of the radius of curvature of the tip apex [78]. Typical tips used in experiments have apex radii of 5-10 nm and can thus be seen as nanoscopic light sources [64, 79, 80]. When the tip is raster scanned over a sample a change of index of refraction at the surface leads to a change in the scattering efficiency of the near-field light [81]. In conventional aSNOM this is used as contrast mechanism. Collecting the light backscattered from a light source focussed onto the sharp tip allows conclusions about the permittivity in the local region below the tip.

### **2.1.1. Higher Harmonic Detection**

The challenge of aSNOM lies in the fact that the light scattered from the small near-field region is overlaid by an often much larger portion of light scattered by the tip or by sample volumes in the farther neighborhood of the tip apex. The low intensity near-field component has to be filtered out. This is usually done by a modulation—demodulation scheme. The modulation is achieved by using an atomic force microscope (AFM) in non-contact mode and the demodulation can be done by a lock-in amplifier. The intensity of the near-field part of the scattered light has a non-linear, nearly exponential, tip-sample-distance dependence. A sinusoidal modulation of the vertical tip position will give rise to components at higher harmonics of the mechanical modulation frequency  $\omega$  [82–84].

For the light scattered solely at the tip, the situation is different. When the modulation is kept small compared to the focus size, the tip is moving in a field with a low gradient. The scattering intensity is nearly constant with a small harmonic

component and hardly any signal at higher harmonic frequencies. With our tip modulation amplitudes of  $\approx 20$  nm, filtering with a lock-in amplifier (Stanford Research, SR844) at the second or third harmonic is sufficient to filter out the far-field component and only detect a near-field signal.

### 2.1.2. Interferometric Amplification

Another difficulty is the low intensity of the near-field light. The intensity of the illumination beam is limited in intensity by the damage threshold of the tip to roughly  $0.5 \text{ MW/cm}^2$ . This limits the intensity of the light backscattered from the near-field region to intensities in the order of the noise-equivalent-power (NEP) of typical detectors. A standard way to overcome this fundamental problem is an optical amplification scheme [85]. The weak signal carrying beam  $I^{(\text{sig})}$  is interferometrically mixed in a beamsplitter (Thorlabs, BSW11) with a stronger reference beam  $I^{(\text{ref})}$ . The detected light has the intensity:

$$I = |\mathbf{E}|^2 = \mathbf{E}^{(\text{sig})} \overline{\mathbf{E}^{(\text{sig})}} + \mathbf{E}^{(\text{ref})} \overline{\mathbf{E}^{(\text{ref})}} + 2\text{Re}(\mathbf{E}^{(\text{sig})} \overline{\mathbf{E}^{(\text{ref})}}) \quad (2.1)$$

$$= I^{(\text{sig})} + I^{(\text{ref})} + 2\sqrt{I^{(\text{sig})}}\sqrt{I^{(\text{ref})}}\cos\Delta\varphi \quad (2.2)$$

where  $\Delta\varphi$  is the phase difference between the two beams. The first term,  $I^{(\text{sig})}$ , in this sum is much weaker than the others and can be neglected.  $I^{(\text{ref})}$  does not contain any modulation and will be discarded by the lock-in at the latest. The remaining cross term shows how the reference beam interferometrically amplifies the weak signal.

While equation 2.2 illustrates the effect very nicely, it ignores the effect of noise brought into the system by  $I^{(\text{ref})}$ . The region where this process can lead to a

significant improvement of the signal-to-noise ratio (SNR) is determined by the shot noise caused by the intensity of the reference beam. The SNR is given by the ratio between the average number of photons  $\langle n \rangle$  divided by the standard deviation  $\sigma$  [86]. For coherent light  $\sigma$  is given by [87]:

$$\sigma = \sqrt{\langle n \rangle} \propto \sqrt{I} \quad (2.3)$$

In the case of interferometric amplification, the complete light falling into the detector gives rise to the noise while only the interferometric part is responsible for the signal. Therefore, for an ideal detector the maximal reachable SNR would be independent of  $I^{(\text{ref})}$ :

$$\text{SNR} \propto \frac{2\sqrt{I^{(\text{sig})}}\sqrt{I^{(\text{ref})}}}{\sqrt{I}} \quad I^{(\text{sig})} \ll I^{(\text{ref})} \quad \frac{2\sqrt{I^{(\text{sig})}}\sqrt{I^{(\text{ref})}}}{\sqrt{I^{(\text{ref})}}} = 2\sqrt{I^{(\text{sig})}} \quad (2.4)$$

This leads to the conclusion that once the signal is amplified well above the NEP of the detector, no further improvement of the SNR is possible.

Both calculations assume a linear response of the detector to intensity. But once the reference beam is driving the detector into its non-linear regime, the SNR will decrease again.  $I^{(\text{ref})}$  should be chosen to amplify the signal above the NEP of the detector but to keep the detector in the linear regime.

### 2.1.3. Homodyne Amplification

Equation 2.2 shows that the intensity measured by the lock-in amplifier depends on  $\Delta\varphi$ . The phase difference between signal and reference determines whether the two beams interfere constructive or destructively. This can be used to measure both, the amplitude and the relative phase of the signal beam. Over the years several schemes

have been employed in aSNOM:

**homodyne** reference and signal have the same wavelength and amplitude and phase are obtained by measuring twice with two different phase differences  $\Delta\varphi = \psi$  and  $\Delta\varphi = \psi + 90^\circ$  [82]

**phase-shifting** similar to the homodyne scheme but uses more than two steps for the phase difference  $\Delta\varphi$  [88]

**heterodyne** one of the beams is frequency shifted with respect to the other and thus  $\Delta\varphi$  is constantly swept through [81]

**pseudo-heterodyne** a sinusoidal modulation of the optical path length of the reference generates sidebands that can be analyzed [89]

In our measurements we use a homodyne scheme. The phase difference  $\Delta\varphi$  is controlled by a self-built piezo (PI Ceramic, P-887.50) driven mirror assembly. From the two lock-in measurements  $S_1$  and  $S_2$ , the total amplitude  $S$  and the optical phase  $\psi$  can now be calculated by:

$$S = \sqrt{S_1^2 + S_2^2} \quad (2.5)$$

$$\tan \psi = \frac{S_2}{S_1} \quad (2.6)$$

The full determination of  $\psi$  from equation 2.6 is only possible by looking at the signs of  $S_1$  and  $S_2$ .

At this point, the reader is reminded that the cross term in equation 2.2 does have a sign and can become negative. Depending on the sign of  $\cos \Delta\varphi$ ,  $2\sqrt{I^{(\text{sig})}I^{(\text{ref})}}$  is added or subtracted from the offset produced mainly by  $I^{(\text{ref})}$ . Figure 2.1 shows the time evolution of the modulated signal. For a positive  $\cos \Delta\varphi$  the measured intensity

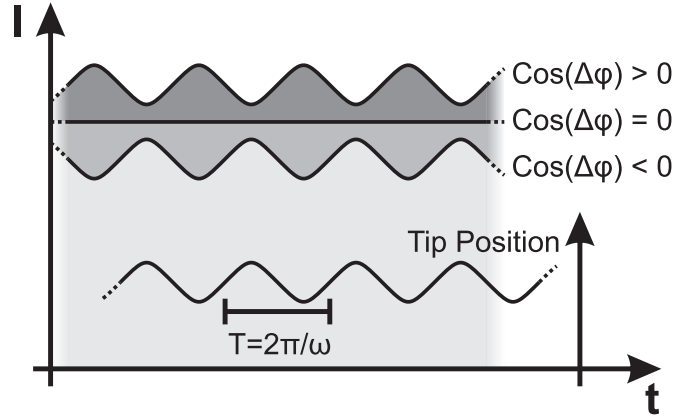


Figure 2.1.: Time-evolution of the modulated interferometric signal. For  $\cos \Delta\varphi = 0$  the measured intensity consists mainly of the constant reference beam  $I^{(\text{ref})}$ . Otherwise, depending on the sign of the cosine term, the signal is modulated in phase or  $180^\circ$  out of phase with the vertical tip position.

is  $180^\circ$  out of phase compared to the vertical tip position, for a negative  $\cos \Delta\varphi$  it is in phase. While the output of a single phase lock-in amplifier is signed, we use the phase display of our dual phase lock-in to determine a sign of the voltage. With the signed measurement values  $S_1$  and  $S_2$  we obtain access to the full  $360^\circ$  range of the optical phase.

#### 2.1.4. Confocal Microscope

In order to reduce the non-near-field light in our setup we use a spatial filtering technique. Figure 2.2 shows how a small aperture can be used to filter out light scattered by only the tip or only the sample. Together with the single mode fiber (Thorlabs 780HP) we use to deliver the light to our setup we turn the optical part of the setup into a confocal microscope.

In our case, as shown in figure 2.2, the light backscattered from the tip is first collimated into a 6 mm wide beam before it is focussed by an aspheric lens (Thorlabs,

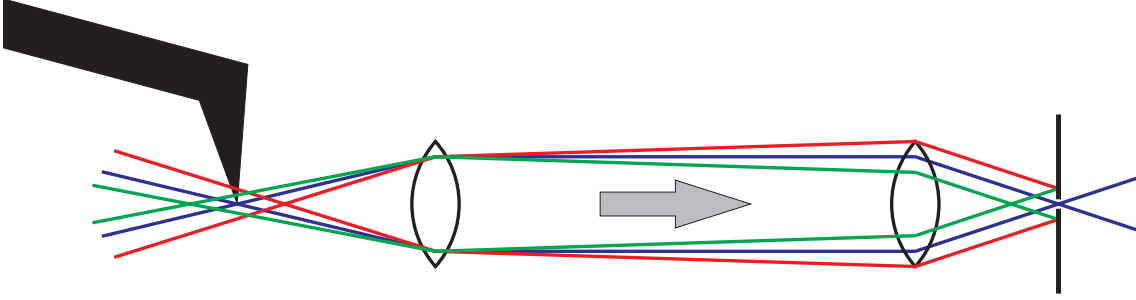


Figure 2.2.: Using a spatial filter in the detection path reduces the light scattered by the tip and the sample.

C280TME-B) on a fiber launch system (Thorlabs MBT613/M) into a single mode fiber. The reference beam is aligned mainly by minimizing its power loss through the fiber. The spatial filtering of the fiber ensures a very good phase front matching of the two beams and maximizes the interferometric amplification efficiency. This has been recognized as being advantageous for polarization sensitive measurements [90–92]. The reference and the signal beam are then delivered together to a avalanche photo (Hamamatsu, C5331-02) or a PIN diode (FEMTO, HCA-S).

## 2.2. Cross-Polarization aSNOM

Since a few years, aSNOM is not only used for index-of-refraction mapping but also for the mapping of plasmons. In an early paper, the resonances of gold discs have been imaged using an oblique illumination with p-polarized light. The dipole character of the resonance is observed as one bright and one dark lobe [70]. Only recently it has been shown that the pattern observed in this image is a result of a strong coupling between the tip and the sample [93]. This makes it complicated to interpret the obtained measurement data. Therefore we will explain here in detail a new method that allows the direct imaging of plasmonic eigenmodes by aSNOM.

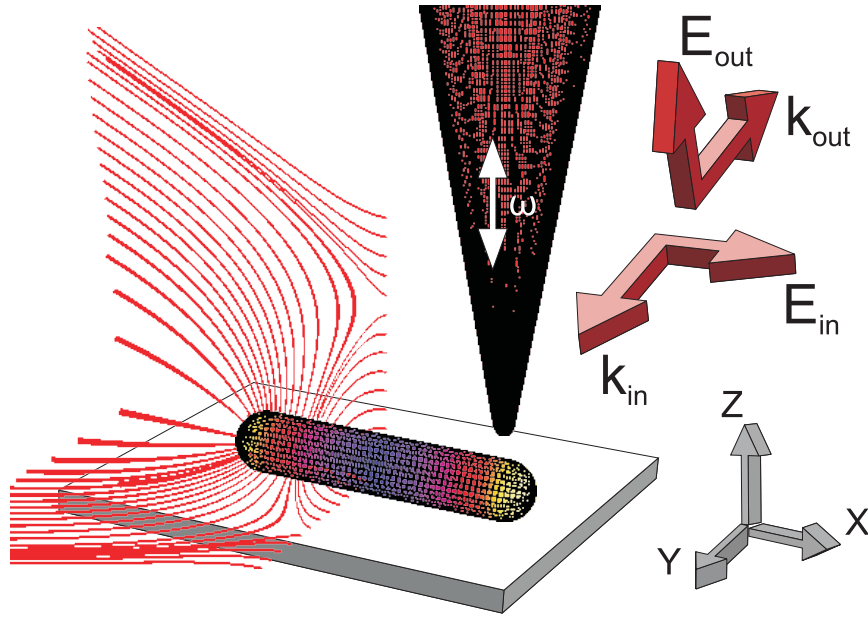


Figure 2.3.: Scheme of the setup. Weakly focused s-polarized radiation excites nano-wires largely unperturbed by the probing tip. A typical response field is indicated by the electric field strength distribution on the wire surface and a snapshot of selected field lines. Backscattered light is modulated by the tip vibration (frequency  $\omega$ ) and polarization-analyzed along the tip-axis.

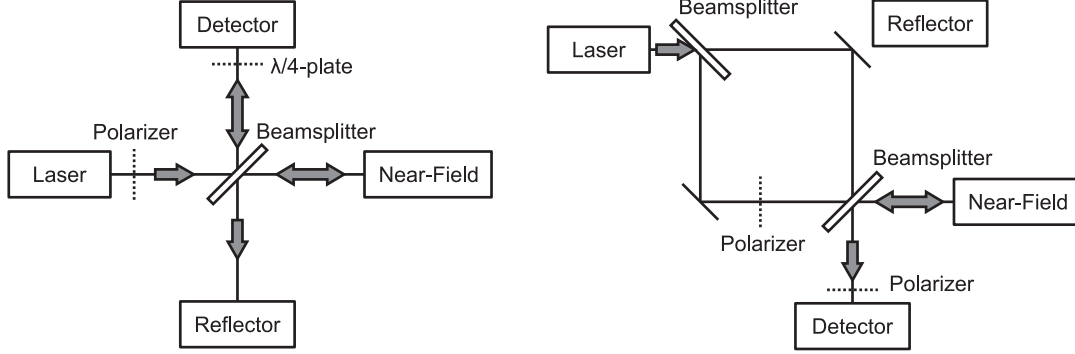


Figure 2.4.: Comparison between (a) Michelson and (b) Mach-Zehnder type interferometer in cross-polarized aSNOMs.

### 2.2.1. Principle

To suppress perturbation of the near-field at the nano-structures by the tip to the largest possible extent, we rely on a cross-polarization scheme (Fig. 2.3) where the illuminating and the scattered field components are orthogonally polarized [71, 94, 95]. For the excitation of the sample we use s-polarized light. This polarization hardly excites the tip at all [74]. In contrast, the structures on the sample may respond with strong plasmonic resonances. The tip efficiently picks up the vertical field components of these resonances and scatters them back into the far-field as mainly p-polarized light.

### 2.2.2. Michelson vs. Mach-Zehnder Interferometer

The method of controlling the two polarizations depends on the type of interferometer used for optical amplification. Many aSNOMs use a Michelson type of interferometer and the light is polarized to ensure s-polarization in the illumination path (figure 2.4(a)). By including a  $\lambda/4$ -plate into the reference beam the polarization is turned by  $90^\circ$  and only the p-polarized component of the scattered light is

amplified [96].

We use a different approach and gain much more control over the two polarizations. A Mach-Zehnder type of interferometer allows us to control the polarization of both paths independently (figure 2.4(b)). This would not be necessary if the tip would be a perfect round cone aligned perpendicular to the illumination polarization. All asymmetries of the tip break the perfect cross polarization and make a readjustment of both, the polarizer and the analyzer, necessary.

The light delivered to the aSNOM is neither polarized in the pure s- nor in the p-state. After splitting off the reference path, a Glan-Taylor prism polarizes the illumination to the s-state. After the scattered light is mixed with the reference beam in a second beam splitter, a second polarizer selects the p-component of both beams. By motorizing the rotation stages of the two Glan-Taylor prisms with stepper motors (Controller: Physik Instrumente, PI 511) we can scan the polarizations systematically to find an optimal configuration.

### **2.2.3. Weak Tips**

It is well known that the close proximity of two or more plasmon resonators leads to strong coupling between them [97]. The coupling has a strong influence on the eigenresonances and can drive them in and out of resonance. A metallic tip is such a resonator. With our cross-polarization approach we are weakening this effect by driving only one resonator and exciting the tip only indirectly. Nevertheless, also this indirect excitation can couple back to the investigated structure and can even suppress its excitation [21,98]. This effect is currently used to produce metamaterial analogues of electromagnetically induced transparency [99,100].

To achieve true eigenmode imaging of plasmonic resonances we have to avoid using

a second resonator as probe. It is thus preferable not to use metallic or metallized tips. We use non-contact AFM tips (Nanosensors, AdvancedTEC NC) made from silicon instead [101]. Another variant of tips used in the context of surface plasmon imaging are carbon nano-tube AFM tips [70].

When imaging dipole resonant objects with this cross-polarization technique it is possible to directly record the dipolar character exhibiting two lobes with a phase difference of  $180^\circ$  between them. By comparing the near-field images with simulation data we have also found that the recorded images represent maps of the normal component of the undisturbed eigenmode near-fields [71]. In the next chapter we will discuss measurements on nano-wires. The excellent resemblance between our measured signal and simulations conducted without including a tip will support this view.

## 2.3. Implementation

Our aSNOM implementation has been described in detail earlier [80, 102] and we constrain ourselves here to a brief description of the main components. We use a commercial AFM (Park Scientific, M5) for the non-contact mode distance control of the tip. The vibration amplitude of the cantilever kept at about 20 nm. Underneath the AFM head we mounted a low coefficient of thermal expansion INVAR-plate (material-number 1.3912) to mount the optical components on. The layout of the optical setup is shown in figure 2.5.

From a tunable continuous wave light source (Ti:Sa, Coherent 899) we deliver the light by a single mode fiber to our setup. The laser beam is kept on a height of 5 cm and is directed by protected silver mirrors (Thorlabs, PF05-03-P01 and PF10-03-P01) to ensure a large operation wavelength range. In front of the AFM head we

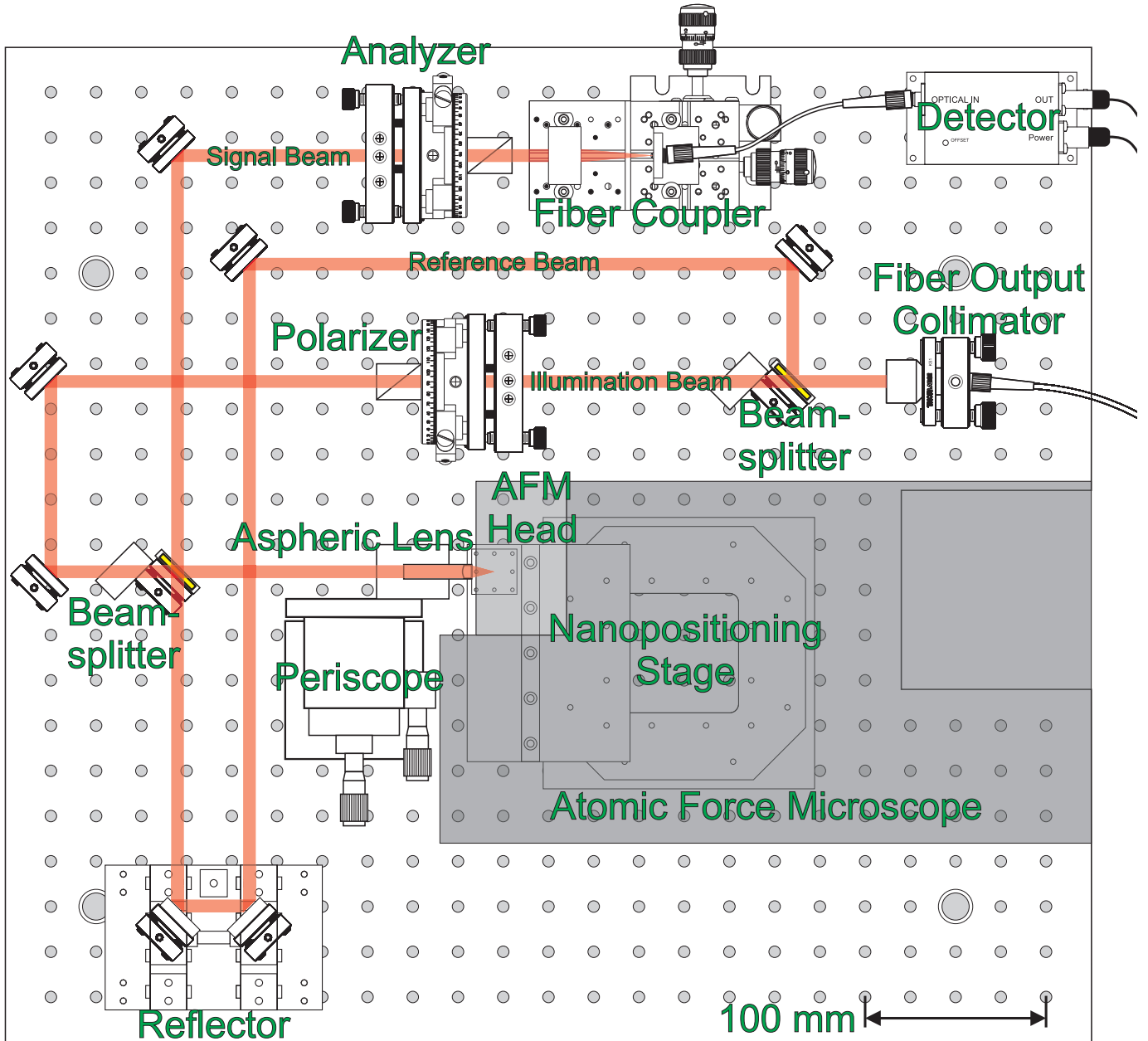


Figure 2.5.: Top view of the experimental setup. The light delivered by a single mode fiber is split into an illumination and a reference beam. A Glan-Taylor prism polarizes the illumination beam horizontally. An aspheric lens focusses the light onto the tip of an commercial AFM. The backscattered signal beam is mixed with the reference beam in a second beamsplitter. An analyzer selects the vertical polarizer component. Coupling back into a single mode fiber before detection ensures a confocal imaging of the tip apex.

mounted a periscope to direct the beam first upward and then onto the sample under an angle of about  $71^\circ$  relative to the surface normal. To focus the light onto the tip we use an aspheric lens (Geltech, NA 0.25) mounted on the periscope. It produces a focus size of about  $2\text{ }\mu\text{m}$  in the red to near-infrared wavelength range. Once we aligned the tip to be in the focus we use a 3-axis piezo stage (Physik Instrumente P-517.3CD scanner, E-710.3CD controller) to raster scan the sample underneath the tip. The components not discussed in this section are mentioned in the previous sections.

## 2.4. Alignment

In the last sections we described the principle idea behind the cross-polarization scheme and the components needed for the setup. Now we will describe in detail how to align the components and how to ensure a good configuration of the polarizers.

### 2.4.1. Finding the Focus

We start our alignment procedure by setting the output polarization at the fiber output coupler to roughly  $45^\circ$  with respect to the surface normal of the optical table. The polarizer is then polarizing the illumination beam horizontally ( $90^\circ$  with respect to the normal). In this first step we do not set the analyzer to be cross-polarized with the polarizer. It is set to an angle of about  $20^\circ$  and makes sure that both polarizations can pass through. We block the reference beam and make sure that the sample underneath the AFM head is still far away from the tip.

To find the center of the illumination focus we use the piezo of the AFM head to scan the tip through the illumination focus. The image we obtain is shown in

figure 2.6(a). It can be easily understood by seeing the optical setup as a confocal microscope in which the sample is scanned instead of the focus. Here, the AFM tip is the sample and its sharp tip apex can be regarded as a perfect point scatterer. With the scattering region of the tip being much smaller than the lateral dimension of the focus, we image the focus shape instead of a sample [75]. From this image we conclude that our focus has a lateral dimension of about  $2.5\text{ }\mu\text{m}$ . We attribute the small modulation in the intensity to interference with light reflected in the setup. For the next step we position the tip in the focus slightly in front of the position of maximal backscattering intensity (blue cross).

### **2.4.2. Polarization Scan**

To gain phase sensitivity we now mix in the reference beam. We now systematically search for a good cross-polarization by raster-scanning the two polarizers. A typical data set we obtain for the two dimensional polarization plane in second harmonic mode is shown in figure 2.7. The position  $0^\circ / 90^\circ$  (analyzer / polarizer) marks the position of nominal cross polarization (marked by a cross). The minimum we find in the amplitude scan 2.7(a) is at the position  $3.5^\circ / 93^\circ$  though. The optical phase 2.7(b) we record simultaneously shows a phase singularity at this position. This minimum is our preferred polarization state because it ensures that the obtained signal in aSNOM imaging comes mainly from polarization rotating features of the sample.

### **2.4.3. Cross Polarized Focus Scan**

After finding the ideal polarization we double check by scanning the focus again. This time we image the focus with interferometric amplification. Fig. 2.6(b) shows a

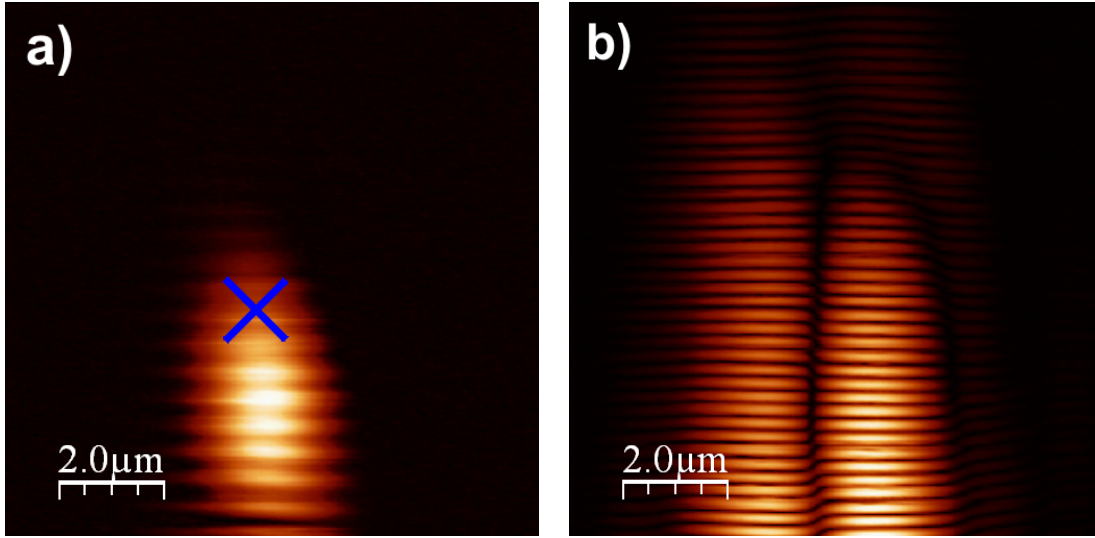


Figure 2.6.: Imaging the focus with the tip: (a) in the parallel-polarization mode a strong backscattering indicates the center of the focus. The blue cross marks the spot where we position the tip for imaging. (b) in cross-polarization mode the black line indicates that the backscattered signal is blocked by the analyzer.

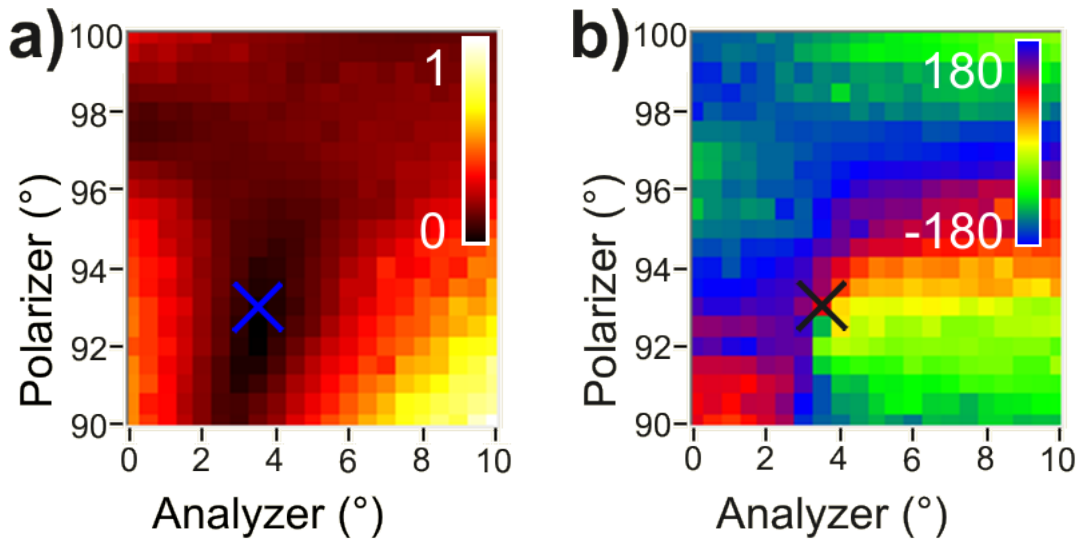


Figure 2.7.: Systematic search for the ideal polarizer angles. (a) shows the optical amplitude measured in 2nd harmonic mode. (b) shows the optical phase. The crossed mark the position of nominal cross polarization.

typical image we obtain. The decomposition of the focus signal in many horizontal lines comes from the interference between signal and reference beam. Moving the tip forward and backward changes the optical path length of the signal beam and accordance with equation 2.2 we see constructive and destructive interference.

We also see a characteristic dark line running from top to bottom through the center of the focus. To our interpretation these positions have a very symmetric configuration:

- The illumination polarization is perpendicular to the tip shaft and does not excite any modes along the tip.
- The analyzer polarization is parallel to the tip shaft and blocks all light being reflected by transversal excitations of the tip.
- The tip shaft is in the center of the focus where the gaussian beam has only horizontal components.

Away from the center, a gaussian focus does not only have E-field components of the main-polarization but also components of the other polarizations [103]. Presumably these small E-field components polarized along the tip shaft are the reason for the signal we observe left and right from the dark line.

The optimal cross polarization configuration depends on the tip. For some tips the optimization procedure needs several iterations to find the correct polarization angles. Some tips are discarded by us because it seems to be impossible to find the right polarization angles for them. We ascribe this to an asymmetric shape of the tips.

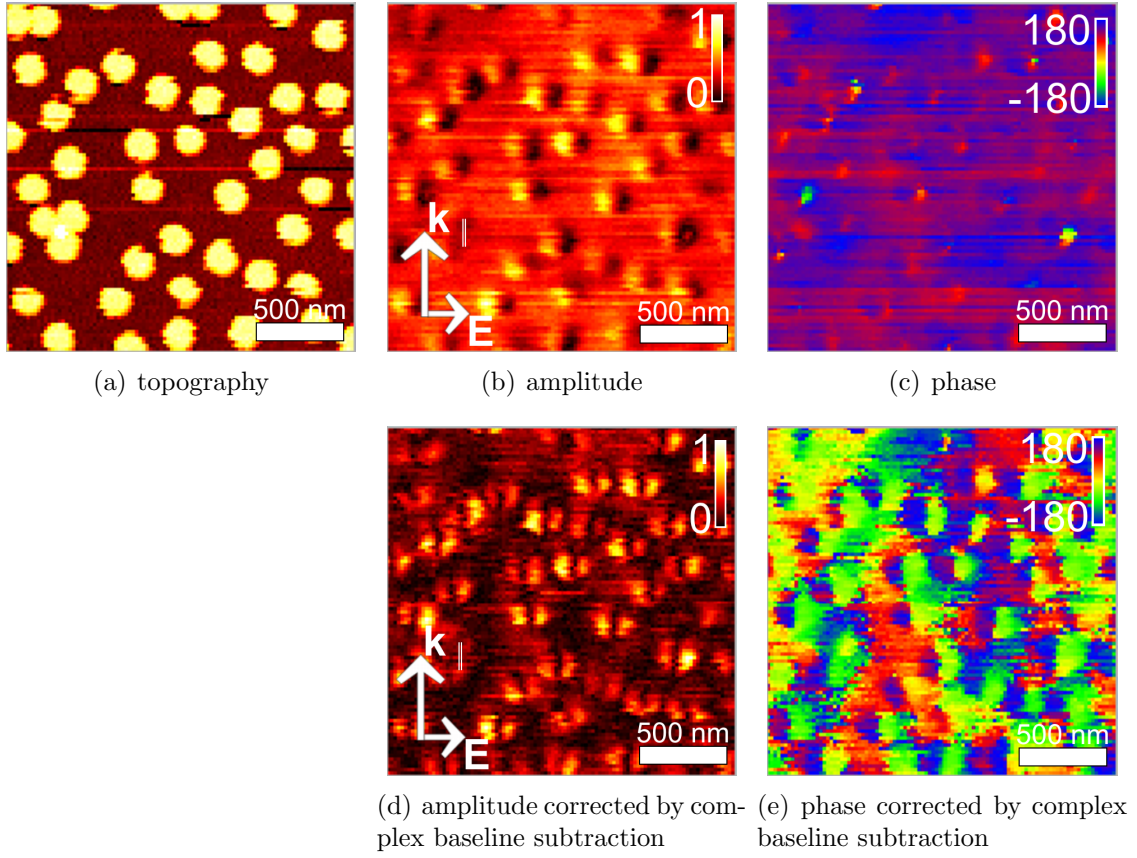


Figure 2.8.: Near-field image of Au discs on  $\text{SiO}_2$ . The optical images show the effect the background signal artefact.

## 2.5. Eliminating the Residual Background Artefact in Cross-Polarized aSNOM

After describing in detail how we align our aSNOM, we now discuss an artefact we observed, which is specific to the cross-polarized configuration.

### 2.5.1. Description of the Artefact

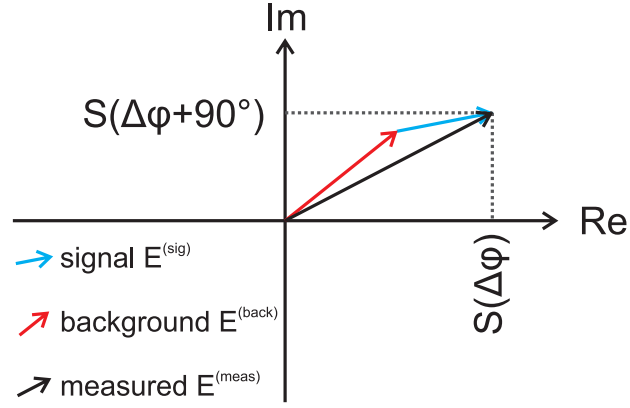
Figure 2.8 shows an image taken with an imperfect cross-polarization alignment. The topography image 2.8(a) shows gold discs on a  $\text{SiO}_2$  substrate. A detailed

study of these structures has been published earlier [71, 75]. The discs are excited by in-plane polarized illuminating light. In the optical image 2.8(b) the dipolar character is visible as one bright and one dark lobe. The dark lobes show regions with reduced optical amplitude, while the bright ones indicate added signal, relative to the regions in between the discs, showing a medium intensity. At the same time the phase image 2.8(c) shows contrast only in a few regions. The areas where the phase deviates from the otherwise uniform rest corresponds to the dark areas of the amplitude image.

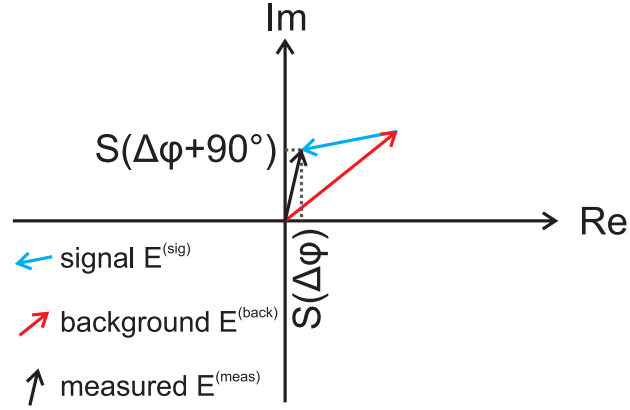
### 2.5.2. Explanation of the Artefact

We can explain these observations by assuming an additional background signal  $\mathbf{E}^{(\text{back})}$  overlaying our optical near-field signal  $\mathbf{E}^{(\text{sig})}$ . This can only happen under imperfect cross-polarization conditions where some of the light being backscattered by solely the tip or solely the sample is not filtered out and leads to a nonzero  $\mathbf{E}^{(\text{back})}$ . Figure 2.9 illustrates the measurement process on the bright and on the dark lobe seen on each disc in figure 2.8(b). The arrows illustrate the complex valued E-fields resulting in our interferometric measurement signal  $\mathbf{E}^{(\text{meas})} = \mathbf{E}^{(\text{sig})} + \mathbf{E}^{(\text{back})}$ . With the two measurements of the homodyne interferometric scheme we are able to determine both, the real and the imaginary part of  $\mathbf{E}^{(\text{meas})}$ .

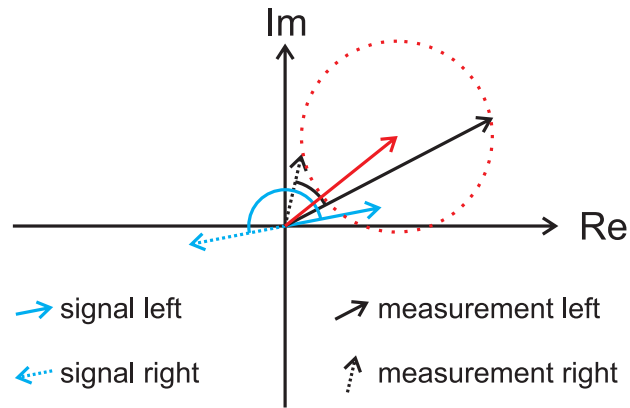
Figure 2.9(a) shows the measurement process on the bright lobe.  $\mathbf{E}^{(\text{back})}$  and  $\mathbf{E}^{(\text{sig})}$  point in nearly the same direction and result in an  $\mathbf{E}^{(\text{meas})}$  with a large amplitude and an optical phase close to the one of  $\mathbf{E}^{(\text{sig})}$ . On the dark lobe  $\mathbf{E}^{(\text{sig})}$  is flipped by  $180^\circ$  while the background stays constant. As depicted in figure 2.9(b), this results in a measured amplitude much smaller than the one of  $\mathbf{E}^{(\text{sig})}$  and the measured phase deviates strongly from the one of  $\mathbf{E}^{(\text{sig})}$ .



(a) measurement on the bright lobe



(b) measurement on the dark lobe



(c) comparison between background and no-background measurement

Figure 2.9.: Explanation of the effect of a background signal.

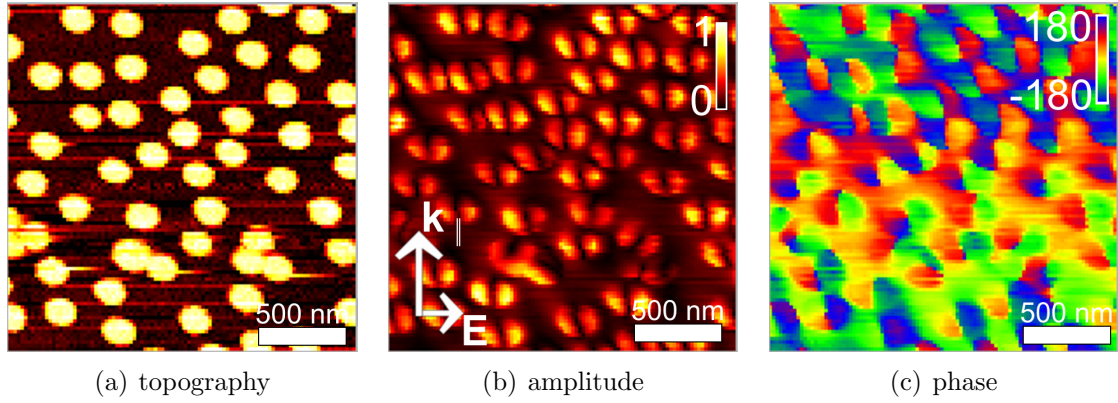


Figure 2.10.: Near-field image of Au discs on  $\text{SiO}_2$  without background. The optical images show the raw data without any correction.

Figure 2.9(c) summarizes these observations. While the optical signals  $\mathbf{E}^{(\text{sig})}$  we are interested in are equally strong and pointing into opposite directions in the complex plane, the measured signals  $\mathbf{E}^{(\text{meas})}$  are unequally strong and show a phase difference much smaller than  $180^\circ$ . Aside of the discs, instead of zero amplitude, we directly measure the background signal. In summary, all measurements of signals with the same amplitude should lie on a circle around the origin of the complex plane. Under imperfect cross-polarization conditions this circle is shifted by a background signal and leads to the disturbed images in figures 2.8(b) and (c).

### 2.5.3. Correction of the Artefact

On the substrate we are measuring only the background signal we depicted as red arrow. On top of the discs we measure the two lobes of the dipole resonance as one amplified, bright lobe and one reduced, dark lobe. This analysis also tells us how to reduce this artefact and to retrieve the original signal. The background signal can be found everywhere in the optical image while the real signal occupies only small areas. Also, for each lobe in the dipolar pattern we can find the counter lobe with

an opposite phase but about the same amplitude. The complex sum of two pixels from opposite lobes gives zero. Calculating the complex valued average of the whole image or one line will retrieve approximately the background signal. Subtracted it recovers the original optical signal. Figures 2.8(d) and (e) show the previous data set corrected by a complex baseline subtraction.

Better than reverting to a correction algorithm is to eliminate the background signal by a good cross-polarization. Figure 2.10 shows the raw data obtained from the same sample as before but with a better alignment. Here, the dipole resonance shows up as two bright lobes with a phase difference of  $180^\circ$ . Comparing figures 2.8(d) and 2.10(b) and 2.8(e) and 2.10(c) shows clearly that the method of ensuring a good cross-polarization leads to less background and should be preferred.

In the following chapters we are always optimizing the positions of both polarizers according the described scheme. The complex valued baseline correction we will be referring to is always just an additional procedure to improve our aSNOM images.



## Chapter 3.

# Plasmonic Resonances of Gold Nano-Wires

In this chapter we use our apertureless SNOM technique to measure the wavelength and reflection phase of plasmons in thin metal wires of finite length with sufficient accuracy to compare against theoretical models [104–107]. Such quasi-one-dimensional metallic structures are frequently also referred to as optical antennas in the literature [104–106]. In the following, to prevent confusion, we adopt the term “metal nano-wire” or short “wire”. This prototypical system can be described as Fabry-Pérot resonators for guided quasi one-dimensional plasmons. With our improved cross-polarization variant of aSNOM we obtain images of amplitude and phase of local electric field components.

The experimental situation has been described in detail in the last chapter. A short description can also be found in figure 3.1(a). For the experiments in this chapter we tuned our continuous wave laser source to a wavelength of 942 nm.

Compared to spectroscopy on particle arrays [43,44,108], our approach has the ad-

vantage that we can easily investigate individual wires. As in combinatorial material science [109], a limited number of images allow us to study a large number of isolated structures under virtually identical conditions, facilitating direct and quantitative analysis of the full system. From the lowest order resonances we obtain experimental values for the propagation *as well as* the reflection [104–107] of plasmons. We nicely confirm that the symmetry-forbidden even-order modes are accessible with off-axis excitation. Quantitatively, our results are in good agreement with simulations. However, we find small, systematic deviations attributed to device imperfections and/or overly idealized modeling, specifically concerning the intriguing behavior of the wire terminations.

### 3.1. Wire Array Sample

The gold nano-structures are prepared on heavily doped silicon wafers coated with a 100 nm silicon-oxide layer. Smooth, 25 nm high Au structures are prepared by standard electron beam lithography, thermal metal deposition and lift-off using a 0.3 – 0.5 nm Ti adhesive layer, whose influence on optical properties can be neglected. We investigate 40 nm wide wires with a length distribution from 40 nm to 1630 nm in steps of 10 nm. In one part of the study, wires are arranged in several interlaced columns as shown in Figure 3.1(c) with a surface-to-surface spacing of 260 nm. Scanning electron microscopic (SEM) analysis confirms that actual sample parameters agree with the nominal values to within the SEM resolution. To study excitation conditions for the lowest even order eigenmode in detail, we use an array of 40 nm wide wires that has been randomized both in length (280 nm, 300 nm, . . . , 360 nm) and azimuthal angle ( $-90^\circ$ ,  $-75^\circ$ , . . . ,  $90^\circ$ ) [see Figure 3.5(a)].

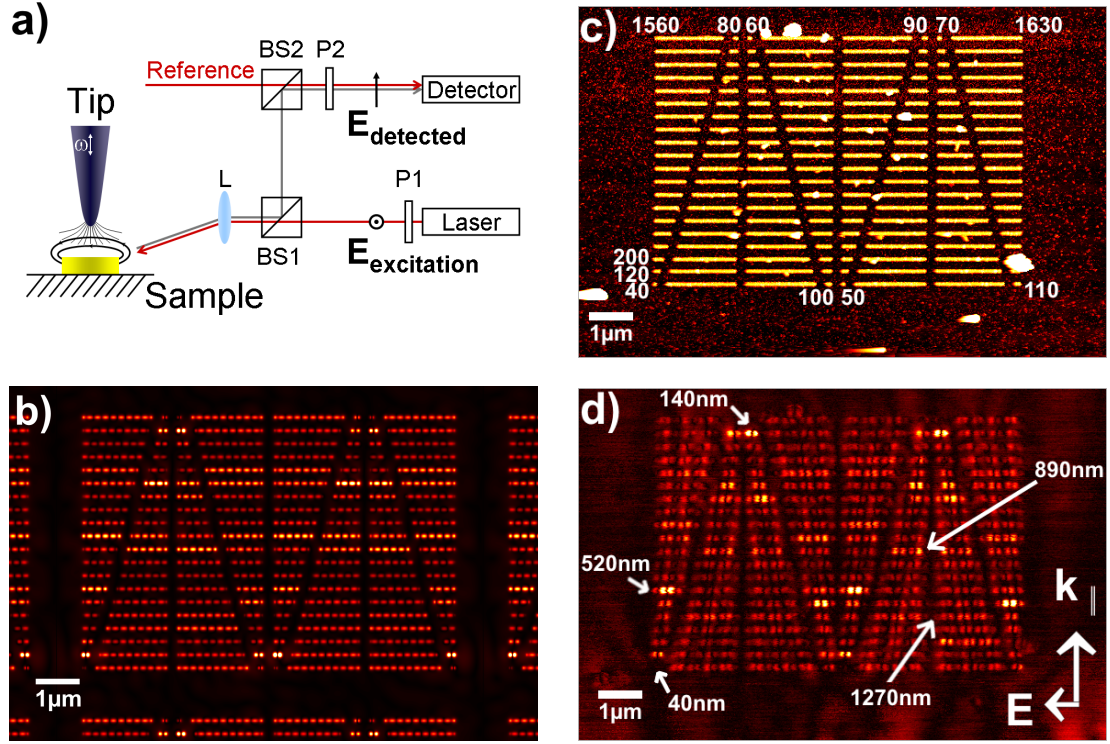


Figure 3.1.: (a) Scheme of the setup. Weakly focused s-polarized radiation excites nano-wires largely unperturbed by the probing tip. A typical response field is indicated by the electric field strength distribution on the wire surface and a snapshot of selected field lines. Backscattered light is modulated by the tip vibration (frequency  $\omega$ ) and polarization-analyzed along the tip-axis. (b) Simulated magnitude of the z-component of the electric field 24 nm above the structure shown in (c). (c) Topography of the metallic nano-wires. The wires of different length are arranged in a compact manner, though sufficiently separated to reasonably assume they are noninteracting. (d) Simultaneously obtained, baseline corrected near-field optical amplitude image for an excitation wavelength of  $\lambda = 942$  nm.

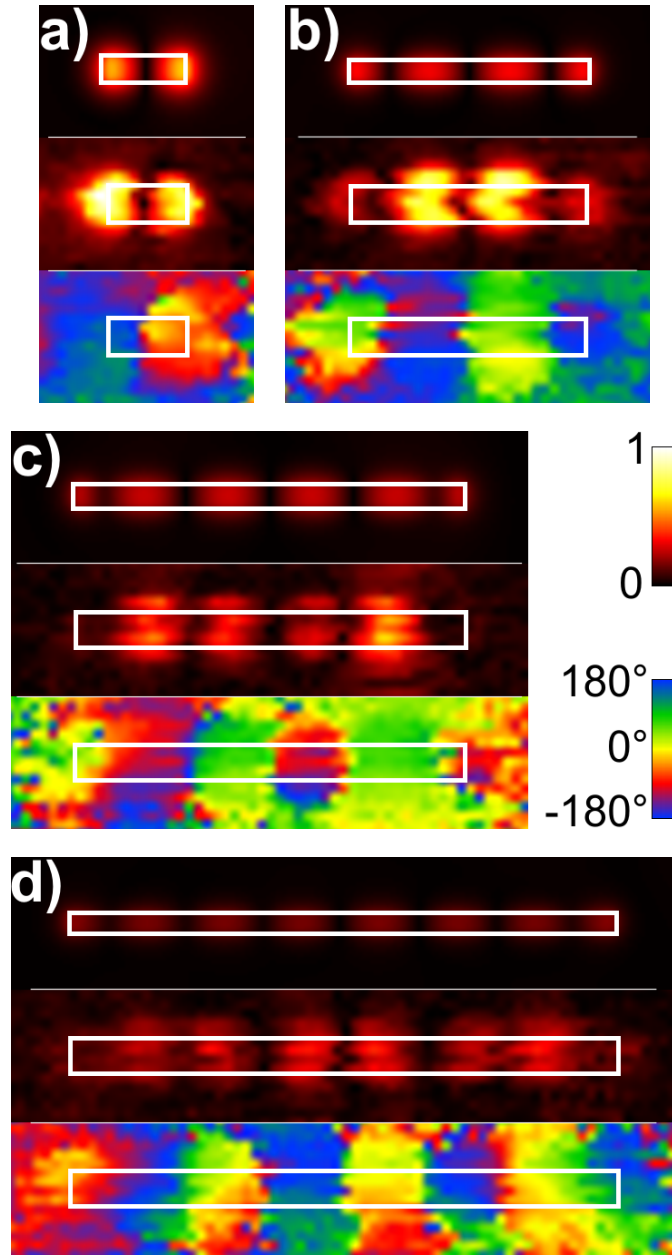


Figure 3.2.: (a)–(d) Compound images of simulated magnitude (top), measured magnitude (middle) and phase (bottom) for the 140 nm, 520 nm, 890 nm, and the 1270 nm long wires, respectively, which represent the odd order resonances. White rectangles indicate the contours of the wires as taken from the nominal and measured geometry.

## 3.2. Simulations

To compare with theoretical predictions, we perform extensive FDTD simulations [110]. The spatial domain is discretized with a resolution of 8 nm. For the refractive index we use values reported in literature [30]:  $n_{\text{Au}} = 0.198 + 6.046i$ ,  $n_{\text{SiO}_2} = 1.536$  and  $n_{\text{Si}} = 3.638$  at  $\lambda = 942$  nm. The semi-infinite half space above the substrate is assumed to be air. The sample shown in Figure 3.1(c) is entirely discretized as one supercell and arranged periodically in lateral directions to make use of periodic boundary conditions with periods of  $9.696 \mu\text{m}$  and  $6.896 \mu\text{m}$  – large enough to exclude interactions with neighboring supercells. The wires shown in Figure 3.5(a) are simulated individually with a square periodicity of  $1 \mu\text{m}$ . In the normal direction we assume perfectly matched layers. The structures are illuminated with s-polarized plane waves at an incidence angle of  $71^\circ$  with respect to the surface normal, reproducing exactly the experimental conditions.

The simulations do not include any probing tip. The measured signal is taken to be the normal component of the local electromagnetic field in a plane 24 nm above the structure. Based on our cross polarization scheme [71], this assumption is justified a posteriori by the excellent agreement between experimental and numerical data.

## 3.3. Odd Order Resonances

### 3.3.1. Near-Field Images

Figure 3.1(d) displays the near-field image of the sample shown in Figure 3.1(c) recorded with excitation polarization parallel to the wire axis. For presentation,

the image has been corrected with a line-by-line removal of a small complex-valued offset, attributed to remnants of parasitic background scattering. This does not affect the following analysis. Evidently, the signal strength varies strongly from wire to wire.

The shortest, 40 nm long wire exhibits a very weak signal while the 140 nm long wire gives the strongest signal. Its modal field distribution [see Figure 3.2(a)] is characterized by two amplitude lobes and a single nodal line in-between. This clear indication of a dipolar mode is also confirmed by the optical phase image which shows a difference in phase between the two lobes of about  $180^\circ$ . Longer wires show higher order resonances, enumerated by the number of node-lines crossed along the length of the wire. Thus, the third order resonance is observed for a wire length of  $\approx 520$  nm [Figure 3.2(b)] and the fifth for  $\approx 890$  nm [Figure 3.2(c)]. In Figure 3.1(b) we show the z-component of the  $\mathbf{E}$ -field 24 nm above the structure, as extracted from an FDTD simulation of the full structure. Comparing experiment and simulation shows a good agreement in the distribution of (near-) resonant wires as well as the modal structure of the individual wires.

The general interpretation of these observations are plasmonic standing waves patterns [111]. That is, inside the metal volume the charge density exhibits localized lobes of alternating sign along the wire length which oscillate in time. Associated electromagnetic fields are both effect and driving force of these fluctuations. As depicted in Figure 3.1(a) for the first order mode, outside the metal-dielectric interface the cross-polarized aSNOM probes the electric field component along the tip shaft. Only odd order modes are observed to show strong local fields in Figure 3.1(d). The even order modes, which are mirror symmetric about the y-z-plane, are fundamentally mismatched to the anti-symmetric excitation.

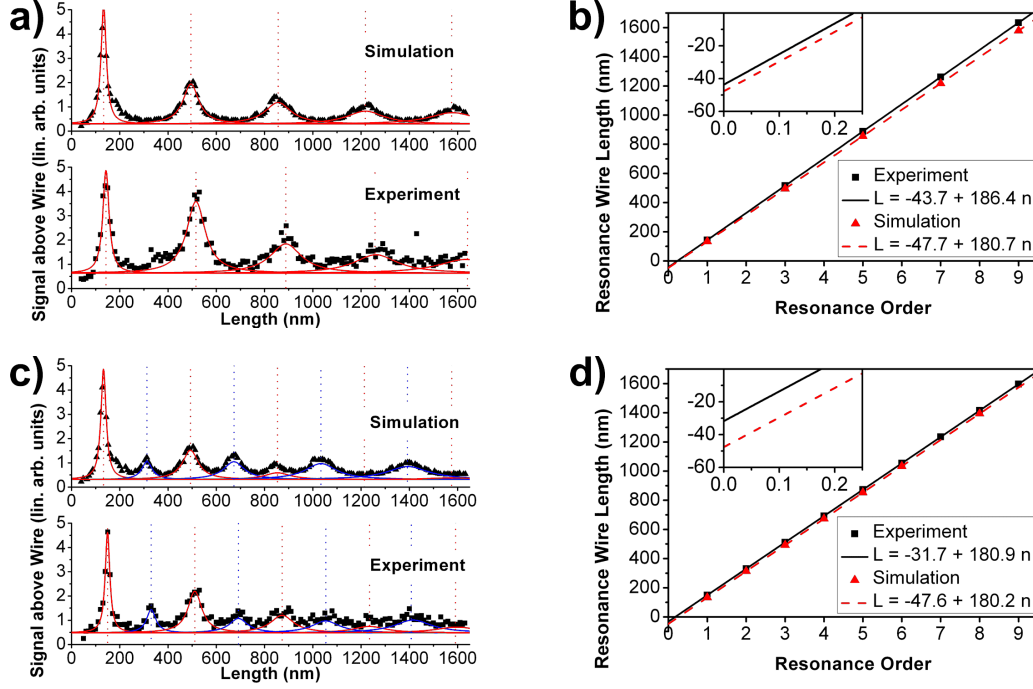


Figure 3.3.: (a) Resonance curves obtained by plotting the maximum signal per wire versus the wire length. The experimental and simulation data has been extracted from figure 3.1. The solid lines show Lorentzians fitted to the data. (b) Plot of the Lorentzians' peak positions versus the resonance order. The lines are a least square fit to the data. The inset is a zoom where the fitted straight lines cross the y-axis. (c) Resonance curves when the sample is rotated by  $\approx 20^\circ$ . (d) Resonance length versus resonance plot of the rotated sample.

For the symmetry-allowed odd modes, a more detailed comparison of the measured versus simulated signal reveals small differences for individual wires, particularly for higher order resonances [Figure 3.2(a)–(d)]. Generally, the measured local field strength at the ends is found to be considerably lower than at the central lobes and the inner lobes exhibit a tendency to pair up. At present, simulation does not lend a simple explanation, showing hardly any accents on different lobes of a given resonance.

### 3.3.2. Resonance-Length Dependence

Examining the system of wires as a whole, we identify the resonance lengths by extracting the maximum amplitude per wire. Figure 3.3(a) shows a plot of these maxima against wire length. Geometric resonances up to seventh order are clearly observed as peaks. With increasing resonance order, the peak amplitude drops and the width broadens. By fitting these peaks with Lorentzians, we obtain the resonant lengths for the different orders. The first order resonance can be observed at a wire length of 143 nm. From the simulation shown in Figure 3.1(b) we obtain an equivalent curve. As a first finding, the resonances appear slightly shifted towards smaller wire lengths compared to experiment. Figure 3.3(b) shows the resonance wire length as a function of resonance order, which is nicely approximated by a linear fit for both experimental and simulated data:

$$L_{\text{exp}}(n) = -(43.7 \pm 1.4) \text{ nm} + n \cdot (186.4 \pm 0.9) \text{ nm}, \quad (3.1)$$

$$L_{\text{sim}}(n) = -(47.7 \pm 0.8) \text{ nm} + n \cdot (180.7 \pm 0.6) \text{ nm}, \quad (3.2)$$

where  $n$  is the resonance order. In an intuitive and clear interpretation of these observations the nano-wires may be regarded as one-dimensional Fabry-Pérot resonators. Guided SPPs travel along the wire length  $L$  with a propagation constant  $\gamma$  and suffer a phase jump  $\delta\phi$  upon reflection at each end. For the  $n$ -th order resonant wire length the total round trip phase accumulation equals  $n$  times  $2\pi$ ,

$$2\gamma L(n) + 2\delta\phi = 2\pi \cdot n. \quad (3.3)$$

Our measured spacing between subsequent resonant, odd-order wire lengths thus provides an unambiguous unit of one plasmon wavelength,  $\lambda_p = 2\pi/\gamma = 372.8 \text{ nm}$ .

It compares very well to a finite element method mode solver-derived value of 371 nm for the wavelength of an infinite plasmonic waveguide of identical cross section.

### 3.3.3. Reflection Phase

The phase change  $\delta\phi = 42.2^\circ$  at the wire ends, though, is somewhat ambiguous. Viewing the nano-wires as optical nano-antennas [104] suggests an alternative way to interpret this quantity as an apparent length increase  $\delta L = \delta\phi/\gamma$ . Either description is independent of resonance order  $n$  and represents a reactance-related property specific to the wire terminating structure. However, differing conventions are possible of what constitutes “the” nano-wire length for rounded or tapered ends, etc., depending on whether the cap is counted as part of the wire or not. As we regard our cross-sectional end facets as nearly flat, we have a unique length definition for wire antennas. In this light, we judiciously note that the 40 nm width and 25 nm height of our rectangular, substrate-supported, flat-end wires compares well with the 43.7 nm diameter that would be derived following Ref. [104] from equation (3.1) for circular, in vacuo, hemispherically capped wires. The small systematic deviations of the simulated values (equation (3.2)) from our experimental data (equation (3.1)) may have several reasons, such as the imprecise knowledge of  $n_{\text{Au}}$  of thermally deposited gold or the idealized simulated wire geometry including abruptly sharp edges and corners.

The fact that the termination of nano wires have a strong influence on the plasmon resonances is also known from the literature [39]. Changing from a wire with a flat ending to one with rounded ends while keeping the total length constant makes the resonances shift to shorter wavelength in spectroscopy studies [112], they blue shift [45]. Being resonant at shorter wavelength means that the rounded wires have

to be longer to be resonant at the same wavelength as the wires with a flat ending. This is exactly the tendency we observe in figures 3.3(a) and 3.3(c).

The phase pickup at the wire end has recently been explained theoretically. By looking at a mode propagation along on a cylindrical nano wire together with its reflected counterpart and matching them at the boundary with a propagation free space mode it is possible to calculate an analytical expression for the reflection phase [112]. For a 40 nm diameter radius wire and an illumination wavelength  $\lambda = 633$  nm, this model predicts a reflection phase of about  $70^\circ$ .

## 3.4. Even Order Resonances

### 3.4.1. Breaking the Symmetry of the Illumination

Beyond characterizing plasmonic wires using the symmetry allowed odd order resonances our aSNOM approach also allows us to study the resonances with an even number of nodes. In our experiment, this symmetry constraint is easily lifted by changing the azimuthal angle of the sample relative to the excitation. Thanks to retardation, for skew incidence, the  $\mathbf{E}$ -field varies over the length of the wire and its projection onto the wire axis contains a mirror symmetric part, which thus enables the excitation of even modes. By analyzing an image recorded with the sample rotated by  $20^\circ$  (Figure 3.4), we obtain the resonance curve shown in Figure 3.3(c). Most prominently, besides the peaks previously observed (red lines), additional resonance peaks (blue lines) appear at the even order resonance lengths all with nearly the same amplitude. Apparently, the dipole coupling strength of odd order modes to the excitation rapidly diminishes for longer wires, whereas the retardation-enabled coupling of even modes remains equally strong.

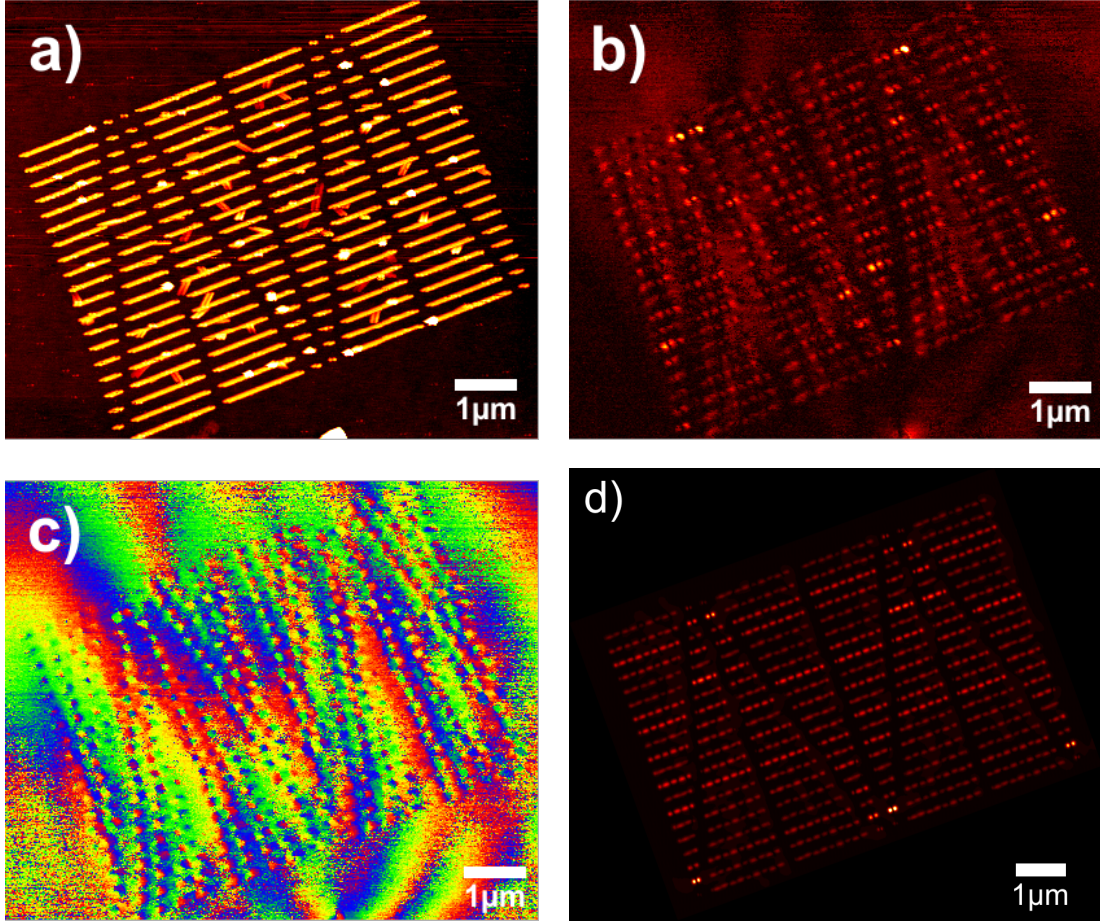


Figure 3.4.: Near-field investigation of the wire-antennas when the illumination is rotated by  $\approx 20^\circ$ : (a) AFM topography image of the rotated sample. (b) Optical amplitude recorded with a cross-polarized aSNOM at an illumination wavelength of  $\lambda = 942$  nm. (c) Optical phase retrieved by an interferometric detection scheme. (d) Simulated magnitude of the z-component of the electric field.

Fitting the peaks in the same manner as before leads to:

$$L_{\text{exp}}(n) = -(31.7 \pm 0.9) \text{ nm} + n \cdot (180.9 \pm 0.6) \text{ nm}, \quad (3.4)$$

$$L_{\text{sim}}(n) = -(47.6 \pm 0.8) \text{ nm} + n \cdot (180.2 \pm 0.6) \text{ nm}. \quad (3.5)$$

The fitting parameters derived from simulation hardly vary between equation (3.2) and (3.5), the corresponding experimental values change significantly from equation (3.1) to (3.4). We attribute the significant difference in the offset value between equations (4) and (5) to imperfect knowledge of the precise geometrical features of the fabricated wire ends, which are simulated as perfectly flat. While these findings will be subject of further, more detailed studies, in the next two paragraphs we concentrate on the angle and length dependence of the lowest even order resonance, which has received only little attention in the literature [55, 107].

### 3.4.2. The Second Order Mode

We analyze an array of wires with lengths distributed around the second order resonance and arranged with varying azimuthal orientations. Figure 3.5(b) shows this mode with three lobes and two nodes. We note that the “front” lobe (as seen from the incident radiation’s point of view) appears characteristically weaker than the middle and back lobe. Analyzing all wires in the same manner as before results in the 2-dimensional contour plot shown in Figure 3.5(c). From a set of individual simulations of each wire we extract the corresponding contour plot shown in Figure 3.5(d).

On the whole, both contour plots agree. The resonance wire lengths appear at  $\approx 330$  nm in experiment and  $\approx 310$  nm in simulation, consistent with equa-

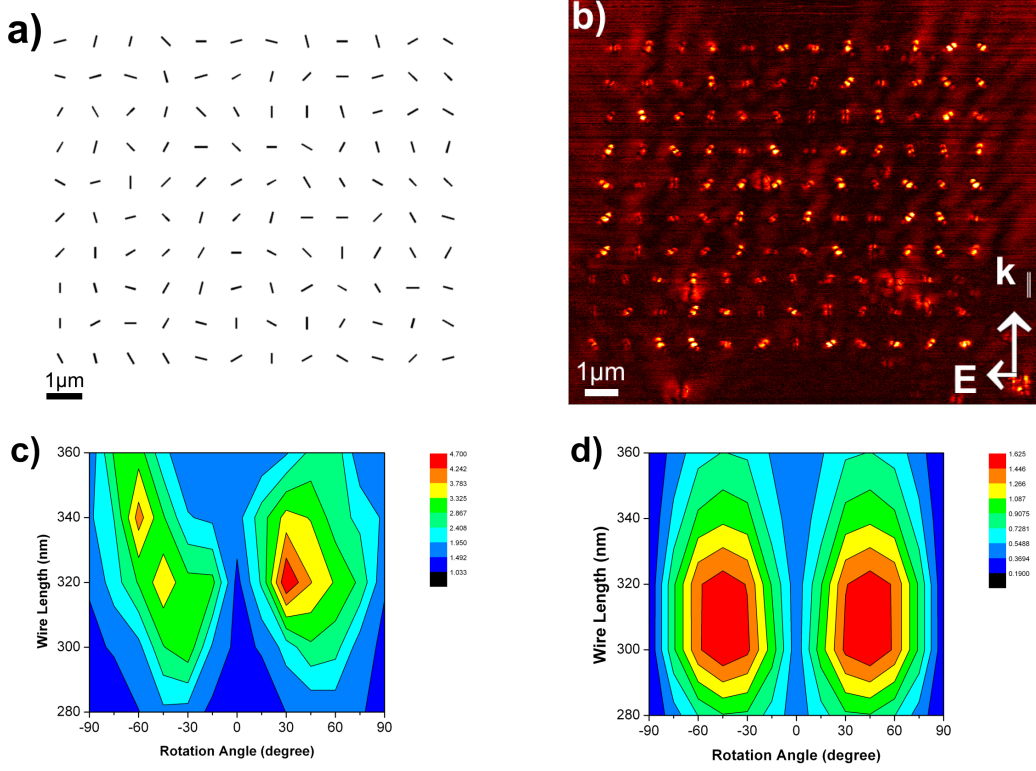


Figure 3.5.: (a) Design of the sample to study the second order resonance. The length and the rotation angle of the wires is varied from 280 to 360 nm and from  $-90$  to  $90^\circ$ . (b) Baseline corrected optical near-field amplitude of the respective sample at an illumination wavelength of  $\lambda = 942$  nm. (c) Detailed analysis of the second order resonance: The maximum signal obtained from each wire is plotted in a 2D angle – wire length – contour plot. The minimum between the two peaks shows that the second order resonance is symmetry forbidden at an angle of  $0^\circ$ . (d) Similar plot obtained from FDTD simulations. The wires of the sample have been simulated individually.

tions (3.1), (3.2), respectively. At the resonance wire length, both plots show maxima at about  $\pm 45^\circ$  as clear indication of an excitation of the even order plasmonic mode. Symmetry suppression explains the minima at  $0^\circ$  and at  $\pm 90^\circ$ .

The directional dependence of excitation – as studied here for the second order mode – could be of use in future applications, for example to tune the response of individual structures by the directionality of the external source or to allow efficient multi-wavelength optical excitation of nano-wires by multi-directional illumination.

A complete understanding of the contour plots is not straight forward. A full description of the wires has to explain two results simultaneously: its property as plasmon resonator with Fabry-Pérot modes and its directionality as receiving antenna. In the next chapter we will continue the discussion of the excitability of gold nano-wires and we will finally come up with an analytical model explaining our observations.

## Chapter 4.

# Emission Patterns of Linear Plasmonic Antennas

In the previous chapter we showed how near-field imaging with a cross-polarization aSNOM can be used to map the excitation of single plasmonic antennas. The amplitude of the near-field was a clear indication for how resonant the individual wires were. By rotating the sample slightly we already learned that the excitation of the modes depended on the illumination direction. For the second order mode, which was not excitable under perpendicular illumination, we even investigated the angle dependence in more detail. In the interpretation we restricted ourselves to qualitative arguments until now. We explained the features of the angle dependence by symmetry arguments. This can answer the fundamental question of how to access the even order modes but does not give any information about the strength of the individual modes. For example, a question that was unanswered until now was why the 7th order peak disappeared at the illumination angle of  $20^\circ$ ? This question can not be answered by symmetry arguments any more. It will need much more insight

to understand the complete physics behind the geometric resonance curves of the last chapter.

In this chapter we will present more data sets from measurements and simulations so that we are covering all angles. To understand the data we derive a new few-parameter model from physical arguments and compare them with each other. The excellent agreement of the model with simulations and experiments gives us confidence to draw far-reaching conclusion from this model at the end of this chapter. With the receiving properties of an antenna being the reciprocal phenomenon of an antennas emission pattern we can contrast the patterns we obtain to emission patterns of normal, radio-frequency (RF) antennas. The enormous qualitative differences we observe justifies the usage of the term “plasmonic antenna” to distinguish them from other antennas.

## **4.1. Angle Dependent Measurements**

To investigate the complete angle dependence of the excitability of the antennas we rotated our sample from an illumination direction perpendicular to the wire axis illumination ( $\phi = 0^\circ$ ) to an illumination direction parallel to the wire ( $\phi = 90^\circ$ ) in  $15^\circ$  steps. Due to symmetry this segment is enough to conclude for the full circle. In addition to the experiments we look at data from FDTD simulations with illumination from  $\phi = 0^\circ$  to  $90^\circ$  in  $5^\circ$  steps. As in chapter 3 the simulations take the experimental situation into account by including all wires and the substrate. Also the illumination is comparable in both cases. Both times the sample is illuminated under grazing incidence with the only difference that the simulation uses a plane wave while in the experiment the beam is focussed with a numerical aperture of 0.25 [102].

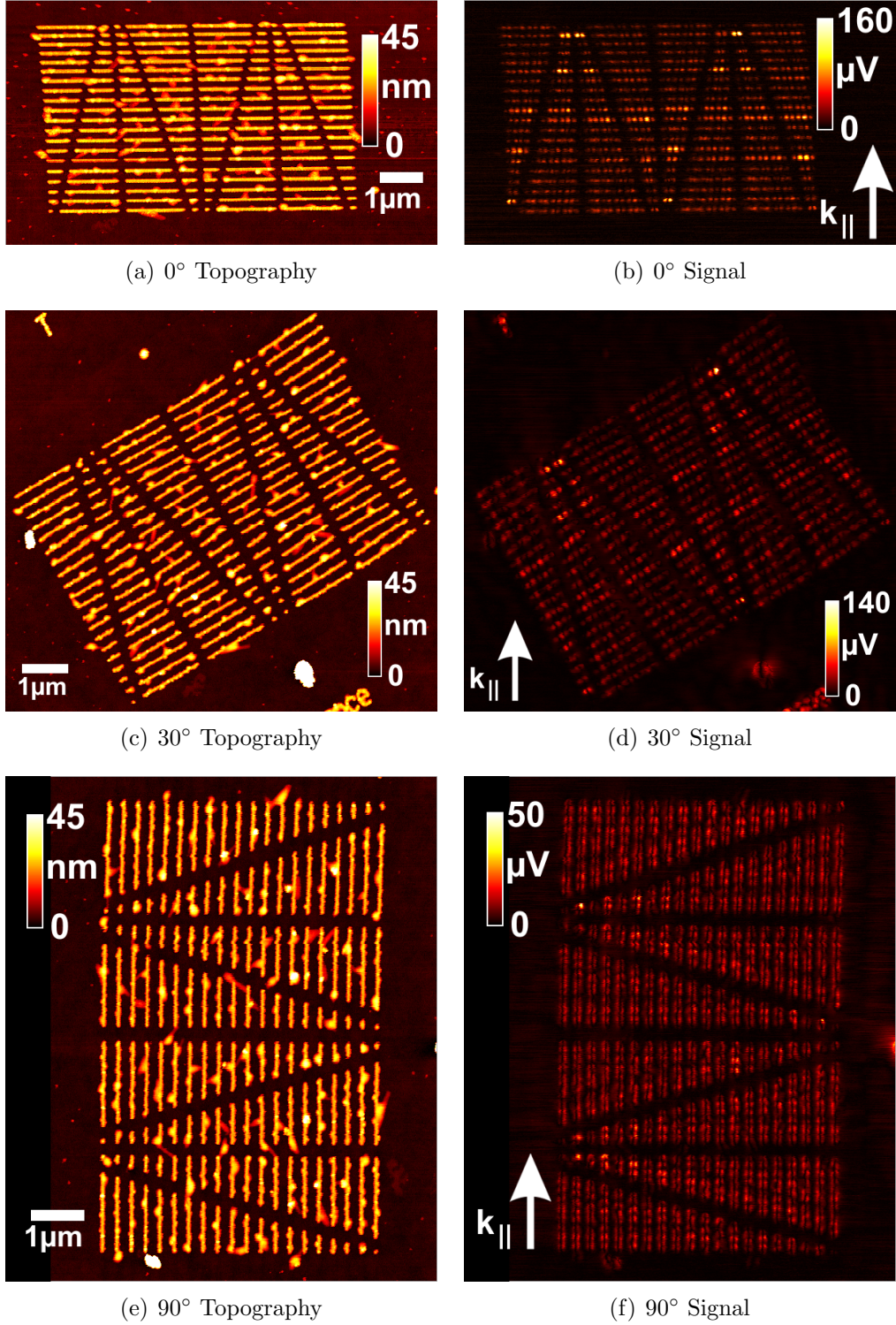


Figure 4.1.: AFM topography and measured aSNOM near-field signal: the topography images of the gold wires on the SiO<sub>2</sub> surface are recorded simultaneously with the near-field images. The direction of the 911 nm wavelength illumination laser beam is indicated by an arrow.

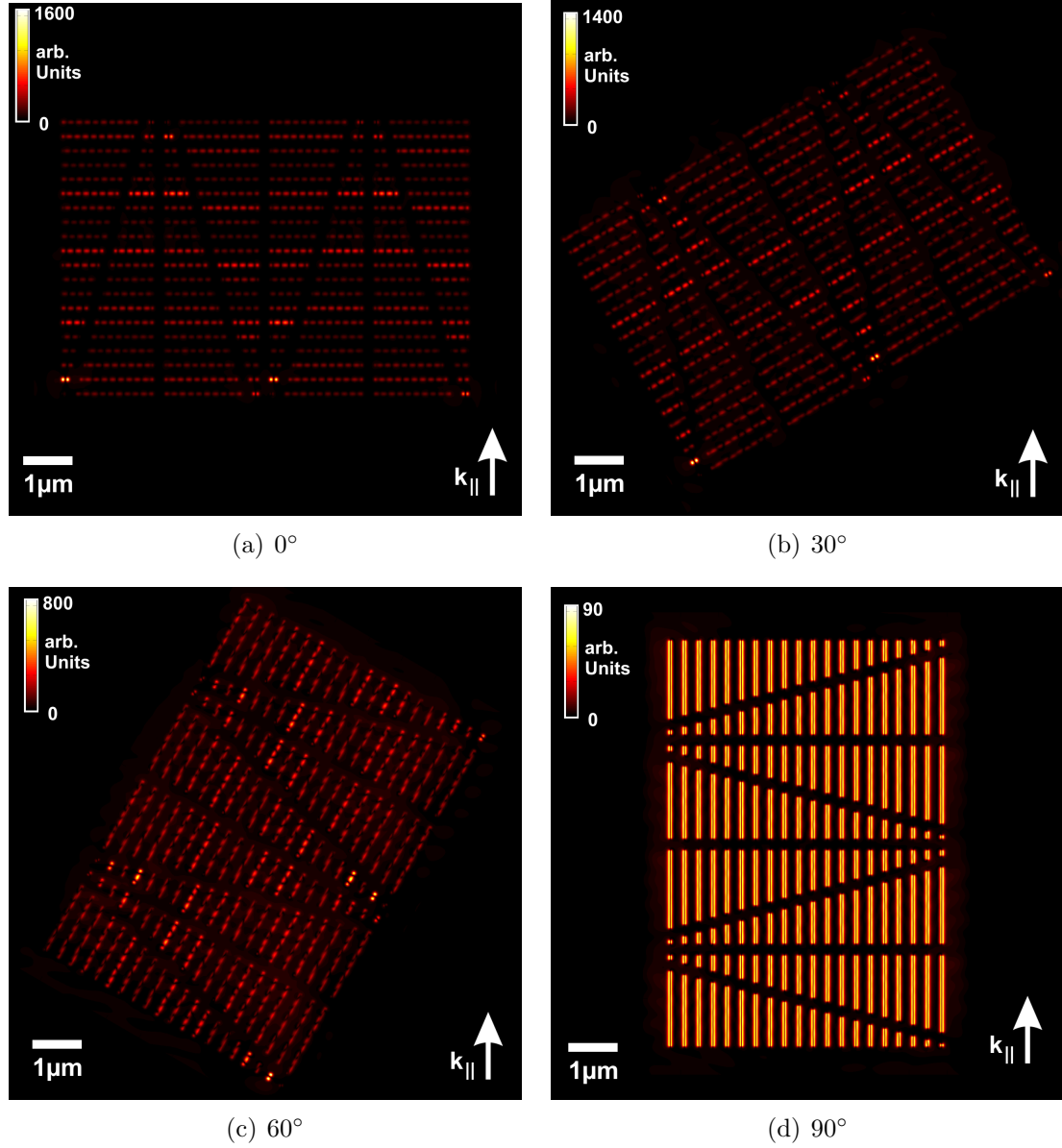


Figure 4.2.: FDTD simulations: magnitude of the radial component of the E-field 24 nm above the wires for different illumination angles. The parallel component of the oblique illumination's wavevector is indicated by an arrow. The wavelength of the plane wave is  $\lambda = 911$  nm.

The near-field images (figure 4.1) are similar to the ones in the previous chapter with the difference that we used 911 nm as illumination wavelength. They also show a good agreement with the radial-component of the E-field taken from the simulations (figure 4.2). In both cases we see nodes and lobes along the wires with different intensity depending on the length of the wire. A special case is the illumination at 90° angle (figures 4.1(f) and 4.2(d)) where the two images differ slightly. While the simulation shows exclusively a higher order transversal mode, the experiment also shows some intensity variation in the direction along the wire. This small difference might be an effect of the numerical aperture used in the experiment.

For a further, more detailed study we use the analysis procedure of extracting the maximum signal per wire described in the previous chapter. Some of the length-amplitude plots obtained from this method are shown in figures 4.9 and 4.12. These plots show the geometric resonances of the wires. By analyzing the peak heights in these plots we can draw conclusions about the dependence of the excitability of the wires on the illumination angle.

## 4.2. Analytical Model to Describe the Wire Excitation

To understand the angle dependence of the excitation better and to get an insight into the underlying physics we now derive a new model that will describe our observations. This theory will describe the longitudinal resonances of wire antennas. The contributions from transversal modes are not included into the equations itself but observed as a small signal offset when fitting our data. In deriving the model we let us guide by RF antenna theory as found in standard text books [113, 114]. In con-

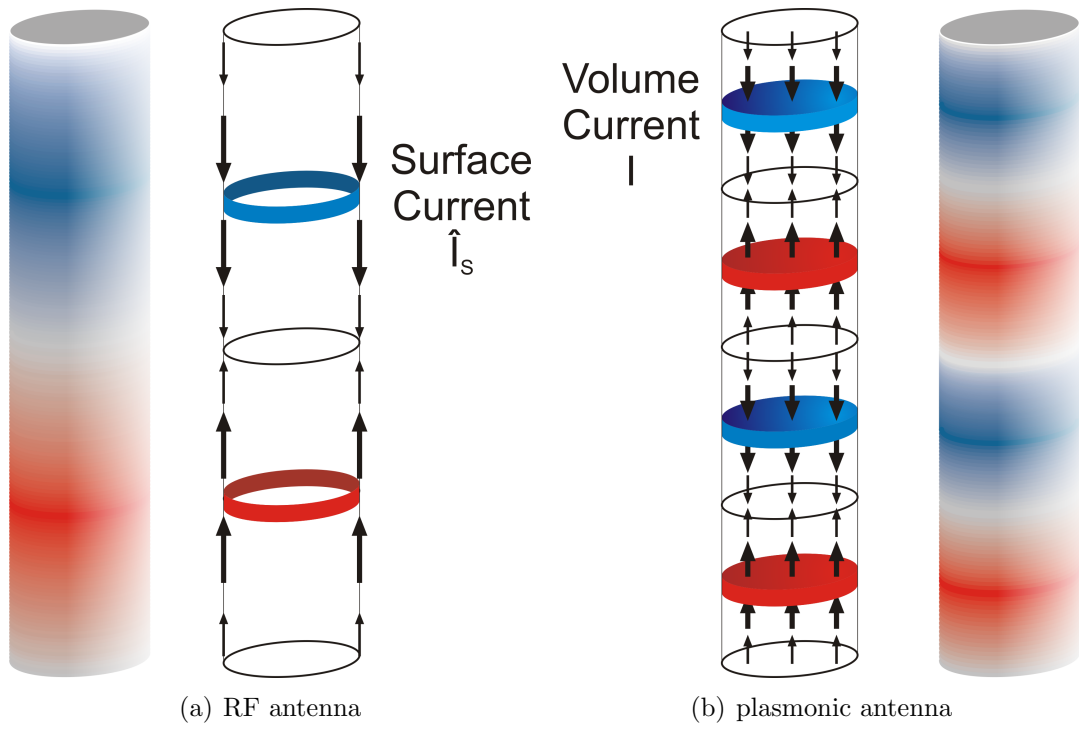


Figure 4.3.: Difference between RF antenna theory and the plasmonic antenna theory: (a) RF antenna with only a surface current; (b) plasmonic antenna with a volume current and a much shorter (plasmon) wavelength;

trast to standard antenna theory, we do not assume a perfect conductor as antenna material. In the optical regime the skin depth (the depth by what the amplitude of an electromagnetic wave has declined to  $1/e$  when penetrating into a metal) of real metals is in the same order of magnitude as the diameter of our wire [115]. Thus, unlike standard antenna theory, we will not restrict ourselves to surface currents but consider the possibility of volume currents (fig. 4.3).

In order to be able to obtain an analytical expression for our model we have to simplify the problem. Instead of wires with a rectangular cross-section, our model considers cylindrical wires with the same plasmon wavelength. The diameter of the wires is supposed to be much smaller than the wavelength. The exact diameter of the wires is not important, it enters the equations only through the plasmon wavelength.

In the experiment as well as in the simulations the wires are substrate supported. It is well known that a substrate, even when it is attached to the particle on only one side, shifts the resonance and can lead to additional damping [116]. In our theory, we include these effects into the complex valued plasmon wavelength. More precisely, we use the plasmon wavelength as a fitting parameter in our model. Concerning the far-field emission and reception properties of the antenna that we observe on the air-side of the wire, the substrate is hardly involved. Here, we treat the medium to be vacuum.

### 4.2.1. Illuminating Field

Figure 4.4(a) shows the geometric considerations on our illumination geometry. The cylindrical wire with permittivity  $\epsilon_m$  and length  $l$  is aligned parallel to the  $z$ -axis. As it is typical in antenna theory, the antenna is placed in the center of the coordinate

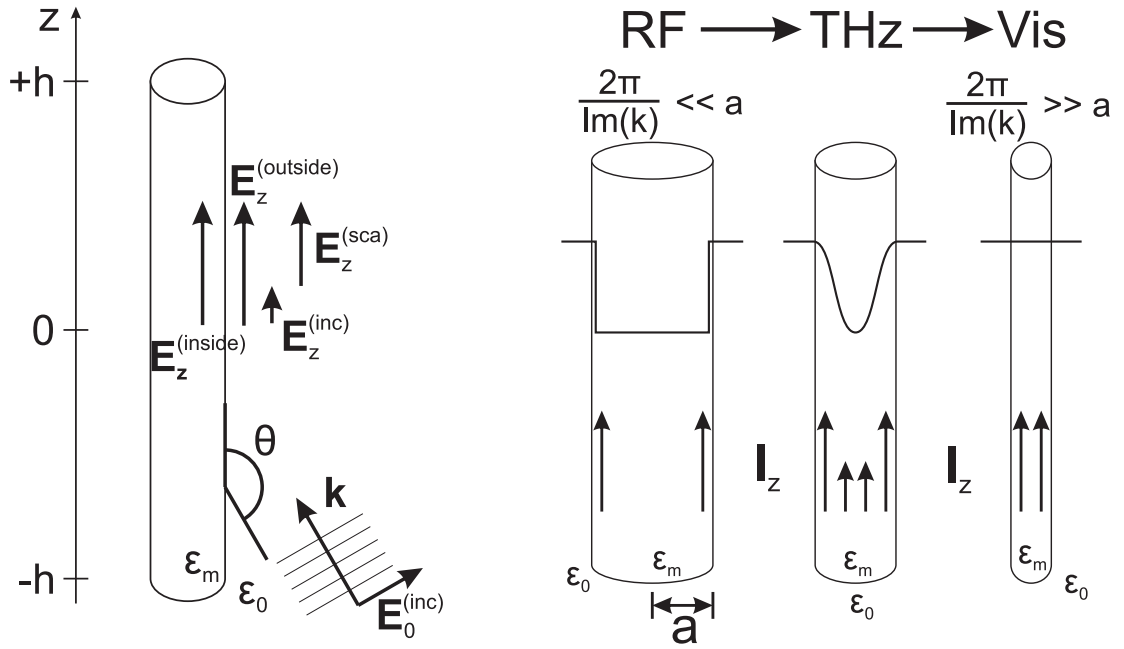


Figure 4.4.: (a) Geometry of the illuminating field: the component parallel to the wire of the incidence E-field  $E_z^{(inc)}$  is responsible for exciting the longitudinal resonances in the wire. (b) Currents inside of the wire: in the RF regime the incident electromagnetic field induces only a surface current; in the visible wavelength range the optical antenna radiuses become smaller than the skin depth and the incidence field induces a volume current.

system and extending from  $-h = -l/2$  to  $+h = +l/2$  where  $l$  is the length of the wire. It is illuminated by a plane wave with a field strength  $E^{(\text{inc})}$  and a wave vector  $\mathbf{k}$ . The angle of incidence relative to the wire's long axis is  $\theta$ . The polarization of the electromagnetic field is parallel to the plane spun by the wire and the wave vector. For the longitudinal plasmon mode only the E-field component parallel to the wire  $E_z^{(\text{inc})}$  is important:

$$E_z^{(\text{inc})}(z) = E_{0,z}^{(\text{inc})} e^{ik_{\parallel}z} = E_0^{(\text{inc})} \sin \theta e^{ik \cos \theta z} \quad (4.1)$$

The model assumes a wire much thinner than the illumination wavelength. On the length scale of the wire diameter the E-field can be assumed as being constant and we can use the above expression for the incident field for the whole cylindrical surface. Thus  $E_z^{(\text{inc})}(z)$  has only a z-coordinate dependence. Also, the E-fields at the wire caps will be small compared to those at the cylindrical surface and we neglect them here. We anticipate end effects that will not be explained by the model.

#### 4.2.2. Field Generated by the Induced Current

The incident field  $E^{(\text{inc})}$  will induce a current in the metal wire. For our thin wire we regard the current as longitudinal [117]. This approximation ignores any cross-sectional currents which are a part of transversal, higher order modes. When we see these modes in our near-field images (fig. 4.1(f) and 4.2(d)) we always see them with a much lower amplitude than the longitudinal modes. Later, when we explain our experimental findings with this theory, we will treat them as a small signal offset. Because the wires are smaller than the skin depth of the metal, the current in the wire can be approximated as homogeneous in the plane perpendicular to the wire:

$$\mathbf{I}(z, r) = I_z(z) \mathbf{e}_z.$$

Next, we can calculate the vector potential  $\mathbf{A}(\mathbf{x})$  of the induced current. For a current flow in the  $z$ -direction it has only a  $z$ -component ([114, eq. 14.4.3] and [113, eq. 9.3]). Together with harmonic time dependence  $e^{-i\omega t}$  (where  $\omega$  is the frequency), in cylindrical coordinates and in the Lorenz gauge,  $A_z(z, r, \phi)$  is:

$$A_z(z, r, \phi) = \frac{\mu_0}{4\pi} \int_{V'} I(z') \frac{e^{-ikR}}{R} d^3x \quad (4.2)$$

where  $R = \sqrt{(z - z')^2 + r^2 - 2rr' \cos(\phi - \phi') + r'^2}$  is the distance of the current to the observer and  $V'$  is the wire volume. Because the current has only a  $z$ -dependence, the integration over the  $r$  and  $\phi$  component can be performed:

$$A_z(z, r, \phi) = \frac{\mu}{4\pi} \int_{-h}^h I(z') \int_0^a \int_0^{2\pi} \frac{e^{-ikR}}{R} r' dr' d\phi' dz' \quad (4.3)$$

$$= \frac{\mu}{4\pi} \int_{-h}^h I(z') G(z - z', r) dz' \quad (4.4)$$

In the last step we introduced the thin wire kernel  $G(z - z', r)$  [114].

From this equation for the vector potential outside of the wire, we can calculate the outside E-field. As usual in electrodynamics [118], we want to match this outside field with an inside field that will be derived in the next section in order to fulfill the boundary conditions. For this we need the vector potential at  $r = a$ . Evaluating equation 4.4 at the wire surface has the inconvenience of a singularity at  $z = z'$ . Fortunately, the singularity exhibits logarithmic behavior and is thus integrative.

Instead of integrating the integral numerically (see discussion in [113, chapter 9.4]) we follow the approach of [114, chapter 21.4] to find an approximate solution. Because of the  $1/R$  dependence,  $G(z - z', a)$  gives the strongest contribution to the integral when  $R \approx 0$ , i.e.  $z' \approx z$ ,  $\rho' \approx \rho$  and  $\phi' \approx \phi$ . This approximation is also

known as ‘Pocklington’s Theory’ [119, p. 180]. This indicates that we can approximate  $G(z - z', a)$  with a delta-distribution:  $G(z - z', a) \approx \tilde{Z}\delta(z - z')$ . As we will see later, despite this crude approximation our model represents all of our observations very well while it permits us to obtain fully analytical expressions. Exact solutions of the integral (i. e. Hallén’s method of iteration [120]) are always numerical.

With the approximation we obtain the following expression for the vector potential on the surface:

$$A_z(z, a) = \frac{\mu}{4\pi} \tilde{Z}I(z) \quad (4.5)$$

The scattered E-field outside of the wire is given by ([113, eq. 9.58]):

$$E_z^{(\text{sca})}(\mathbf{x}) = E_z^{(\text{outside})} - E_z^{(\text{inc})} = \frac{ic^2}{\omega} \left( \frac{\partial^2}{\partial z^2} + k^2 \right) A_z(\mathbf{x}) \quad (4.6)$$

Which leads to the following expression for the field at the surface:

$$E_z^{(\text{outside})}(z, a) = E_z^{(\text{inc})}(z) + \frac{i}{4\pi\omega\epsilon_0} \left( \frac{\partial^2}{\partial z^2} + k^2 \right) \tilde{Z}I(z) \quad (4.7)$$

### 4.2.3. Fields Inside of the Wire

Now we calculate the field and the current inside of the wire antenna. This is where our theory deviates from the standard RF antenna theory. Engineering textbooks usually assume the antenna to be made of a perfect conductor ( $\epsilon_m = \infty$ ) and demand the fields inside of the metal to vanish. For an non-perfect conductor the inside field will not vanish and we will now derive an expression connecting the current  $I$  with the field  $E^{(\text{inside})}$ .

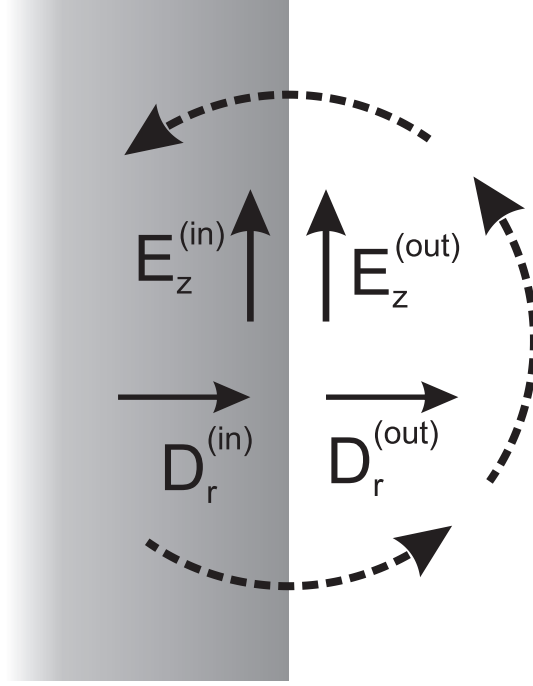


Figure 4.5.: Calculation of the radial component.

Gauss' law in its differential form gives us the divergence of the E-field:

$$\epsilon_m \nabla \cdot \mathbf{E} = \epsilon_m \left( \partial_z E_z + \frac{1}{r} \partial_r (r E_r) \right) = \epsilon_m \left( \partial_z E_z + \frac{1}{r} E_r + \partial_r E_r \right) = \rho \quad (4.8)$$

Due to symmetry, there is no  $E_\phi$  component in this equation. For small radiuses  $a$ , the summand  $\frac{1}{r} E_r$  will become large compared to  $\partial_r E_r$  which is small because  $E_r$  varies on the length scale of the plasmon wavelength.

Figure 4.5 shows how we calculate the radial component of the E-field at the surface, inside of the wire. We first use the boundary condition to express the inside field with the outside field:

$$E_r^{(\text{inside})}(a) = \frac{\epsilon_0}{\epsilon_m} E_r^{(\text{outside})}(a) \quad (4.9)$$

#### 4.2. Analytical Model to Describe the Wire Excitation

---

Next we use Coulomb's law and the small wire approximation for the outside field:

$$\nabla \cdot \mathbf{E}^{(\text{outside})}(a) = 0 \approx \partial_z E_z^{(\text{outside})}(a) + \frac{1}{r} E_r^{(\text{outside})}(a) = \partial_z E_z^{(\text{inside})}(a) + \frac{1}{r} E_r^{(\text{outside})}(a) \quad (4.10)$$

In the last step we used the boundary condition for the tangential component of the E-field.

Together we obtain the following approximation for the divergence of the inner field at the wire surface:

$$\epsilon_m \nabla \cdot \mathbf{E} \Big|_{r=a} \approx \epsilon_m \partial_z E_z^{(\text{inside})}(a) + \epsilon_m \frac{1}{a} E_r^{(\text{inside})}(a) \approx \epsilon_m \partial_z E_z^{(\text{inside})}(a) - \epsilon_0 \partial_z E_z^{(\text{inside})}(a) \quad (4.11)$$

We can also obtain an expression for the current from the equation of continuity ([113, eq. 6.3]):

$$\nabla \cdot \mathbf{I} = -\frac{\partial \rho}{\partial t} = i\omega \rho \quad (4.12)$$

In the last step we used time harmonicity of the charge distribution:  $\rho(\mathbf{x}, t) = \rho(\mathbf{x})e^{-i\omega t}$ .

Together with equation 4.8 we obtain:

$$\nabla \cdot \mathbf{I} = i\omega \epsilon_m \nabla \cdot \mathbf{E} \quad (4.13)$$

$$\partial_z I_z = i\omega (\epsilon_m - \epsilon_0) \partial_z E_z^{(\text{inside})} \quad (4.14)$$

We integrate this expression and obtain:

$$I_z(z) = i\omega \epsilon_m \left(1 - \frac{\epsilon_0}{\epsilon_m}\right) E_z^{(\text{inside})}(z) + I_{\text{const}} \quad (4.15)$$

where  $I_{\text{const}}$  is an integration constant.

#### 4.2.4. Solving the Equations

We now have two equations relating the z-component of the E-field to the wire current, one for the inside (eq. 4.15) and one for the outside (eq. 4.7). Together with the boundary condition for the tangential component of the field,  $E_z^{(\text{outside})} = E_z^{(\text{inside})}$ , we have a differential equation for  $I$ . To solve this equation we make the following ansatz:

$$I(z) = I_{\parallel} e^{ik_{\parallel} z} + I_{\pm} e^{\pm ikz} + I_{\pm p} e^{\pm ik_p z} \quad (4.16)$$

This ansatz for the current comes from assuming five different current waves traveling along the wire:

$I_{\parallel} e^{ik_{\parallel} z}$  a current induced by the illuminating field and having the same wave vector as the z-component of the incidence field ( $k_{\parallel} = k \cos \theta$ );

$I_{+} e^{+ikz}$  **and**  $I_{-} e^{-ikz}$  two currents traveling in both directions along the wire with the wave vector of free space; these terms are commonly used in antenna theory (i. g. [114, 121]);

$I_{+p} e^{+ik_p z}$  **and**  $I_{-p} e^{-ik_p z}$  two counter-propagating plasmonic currents; these currents are not included in RF antenna theory; we assume them to appear in the optical regime where we know that plasmons with a wavelength different from the vacuum wavelength appear on cylindrical wires [34, 122];

Inserting this ansatz into equations 4.7 and 4.15 and comparing the pre-factors

leads to the following results:

$$I_+ = I_- = 0 \quad (4.17)$$

$$\tilde{Z} = \frac{4\pi\epsilon_0}{(\epsilon_m - \epsilon_0)(k_p^2 - k^2)} \quad (4.18)$$

$$I_{\parallel} = \frac{i\epsilon_m\omega E_0^{(\text{inc})} \sin \theta}{1 - \frac{\epsilon_m - \epsilon_0}{4\pi\epsilon_0} \tilde{Z}(k_{\parallel}^2 - k^2)} = i\omega(\epsilon_m - \epsilon_0) E_0^{(\text{inc})} (k_p^2 - k^2) \frac{\sin \theta}{k_p^2 - k^2 \cos^2 \theta} \quad (4.19)$$

In contrast to RF antenna theory, where the E-field at the wire surface, given by  $E_z^{(\text{outside})}(z, a)$ , is set equal to zero, for our theory the vacuum wavelength current is zero. It is also surprising that we obtain an expression for  $\tilde{Z}$ . In antenna theory this value is associated with the impedance and has to be calculated separately. The two factors  $I_{\pm p}$  can not be determined directly from this ansatz. By imposing that the current has to disappear at both wire ends ( $I(\pm h) = 0$ ) we obtain the two necessary conditions. We obtain:

$$I_{+p} = -I_{\parallel} \frac{\sin((k_p + k_{\parallel})h)}{\sin(2k_p h)} = -I_{\parallel} \frac{\sin((k_p + k \cos \theta)h)}{\sin(2k_p h)} \quad (4.20)$$

$$I_{-p} = -I_{\parallel} \frac{\sin((k_p - k_{\parallel})h)}{\sin(2k_p h)} = -I_{\parallel} \frac{\sin((k_p - k \cos \theta)h)}{\sin(2k_p h)} \quad (4.21)$$

Equations 4.19, 4.20 and 4.21 together with the ansatz 4.16 give us the possibility to calculate the current along the wire depending on four parameters: the illumination field strength  $E_0^{(\text{inc})}$ , the illumination wavelength ( $\omega$  or  $k = \omega/c$ ), the plasmon k-vector ( $k_p$ ) and the incidence angle ( $\theta$ ). Generally  $k_p$  will be complex valued, i.e., it includes the damping constant of the plasmon.

### 4.2.5. Perpendicular Component of the E-Field

With today's technology it is impossible to directly measure the current in an optical antenna. But there are a few techniques to probe other measures of the excitation of an optical antenna, i.e. microbolometers [11] or two-photon-luminescence [12, 47]. As in the previous chapter, we use the method of near-field imaging with a cross-polarized apertureless SNOM to determine the excitation of the individual antennas. Compared to other techniques it has the advantage of imposing very little perturbation on plasmonic eigenmodes and providing direct intuition of the measured signal resembles. We showed already in the previous chapter that the amplitude resembles the radial component  $E_r$  of the near-field around the structures [71, 95]. This E-field component can be extracted from our model by using the vanishing divergence of the E-field outside of the wire:

$$\nabla \cdot \mathbf{E} = \frac{1}{r} \partial_r (r E_r) + \partial_z E_z = 0 \quad (4.22)$$

We can use the small wire approximation  $\nabla \cdot \mathbf{E} \approx \frac{1}{r} E_r + \partial_z E_z$  again and obtain:

$$E_r(a) = -a \partial_z E_z = -a \frac{1}{i\omega(\epsilon_m - \epsilon_0)} \partial_z I_z(z) = -a \frac{1}{i\omega(\epsilon_m - \epsilon_0)} \rho(z) \quad (4.23)$$

as expression for the radial component. This quantity will now be the one we compare to our measured and simulated data.

## 4.3. Applying the Model to Experimental Results

With the complete model at hand we can start explaining the different aspects of our measurements and simulations with the model. Before we come to the geometric

resonances we observed in the last chapter, we show how the  $E_z$ -component we calculated in the last section resembles the lobes we see in our near-field images.

### 4.3.1. Near-Field Images

In the previous chapter we showed that our near-field images are very well represented by the z-component of the E-field above the wires. If the model is adequate, equation 4.23 should explain the sequence of lobes and nodes we see along the wire. In figures 4.6(e) and 4.7(e) we show one-dimensional plots of the radial E-field component that we obtain from our model. As wire length we chose  $\lambda_p/2$  (first order resonance) and  $3\lambda_p/2$  (third order resonance) respectively. The first resonance shows two lobes while the third resonance shows four lobes. For both wires the field has a minimum at the center of the plot and the plots end abruptly in a maximum when the wire length has been reached.

This is the same behavior we saw in sections 3.3 and 4.1 in the near-field images and the FDTD-simulations. For comparison, figures 4.6(a) and 4.7(a) show a zoom into the first and the third order resonance of figure 4.2(a). A line cut through the center of the wire is shown in figures 4.6(c) and 4.7(c). The two black vertical lines mark the wire ends as obtained from the topography image. In the range directly above the wire the amplitude line cuts follow the prediction astonishingly well. This can be considered as a first success for our model.

Nevertheless, the simulation shows an  $E_z$ -field that extends over the physical ends of the wires. There are two reasons why the model is not capable of describing this phenomenon. On the one hand the model does not include a description of the wire's end caps which play an important role in this region. On the other hand we evaluate the radial electric field 24 nm above the simulated wire while the model

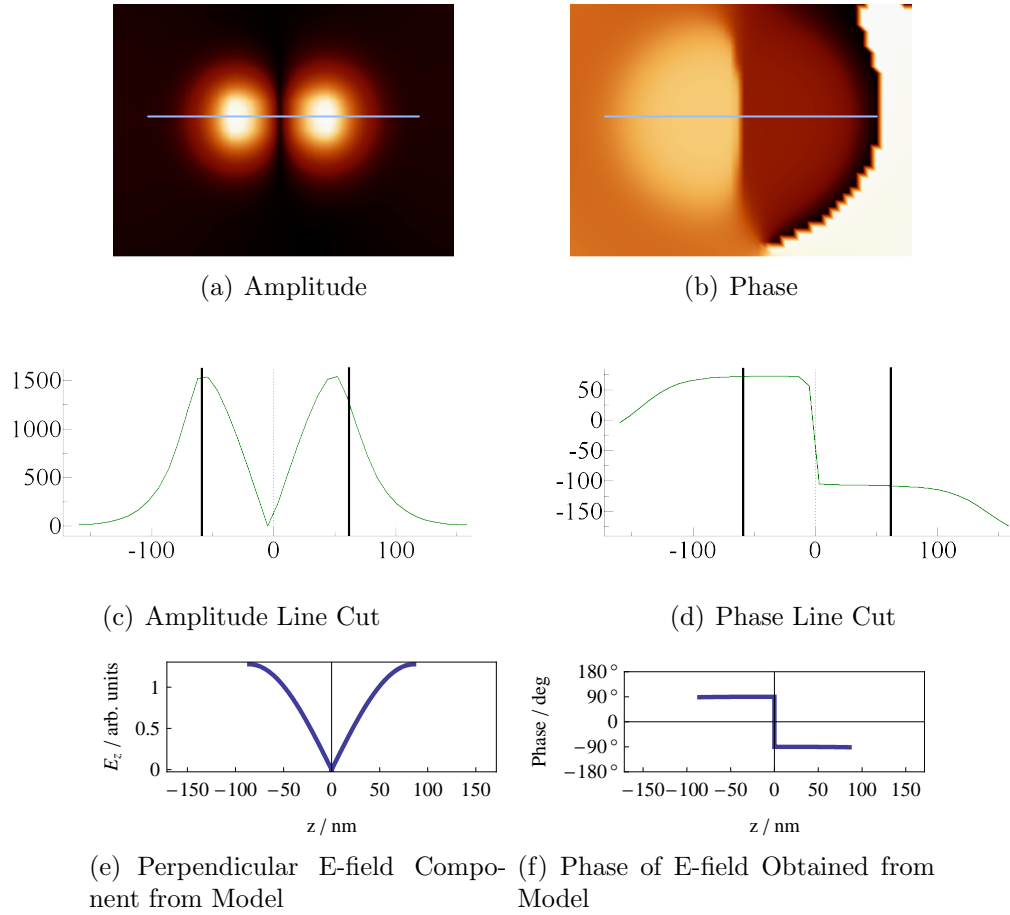


Figure 4.6.: Comparisons between the first order resonance in the simulation and the model: (a) and (b) show the amplitude and phase of the z-component of the E-field 24 nm above the sample; The blue lines indicate the position where the line cuts (c) and (d) through the fields of the first order resonance have been taken; (e) and (f) show the amplitude and phase of the radial component calculated by our model with equation 4.23.

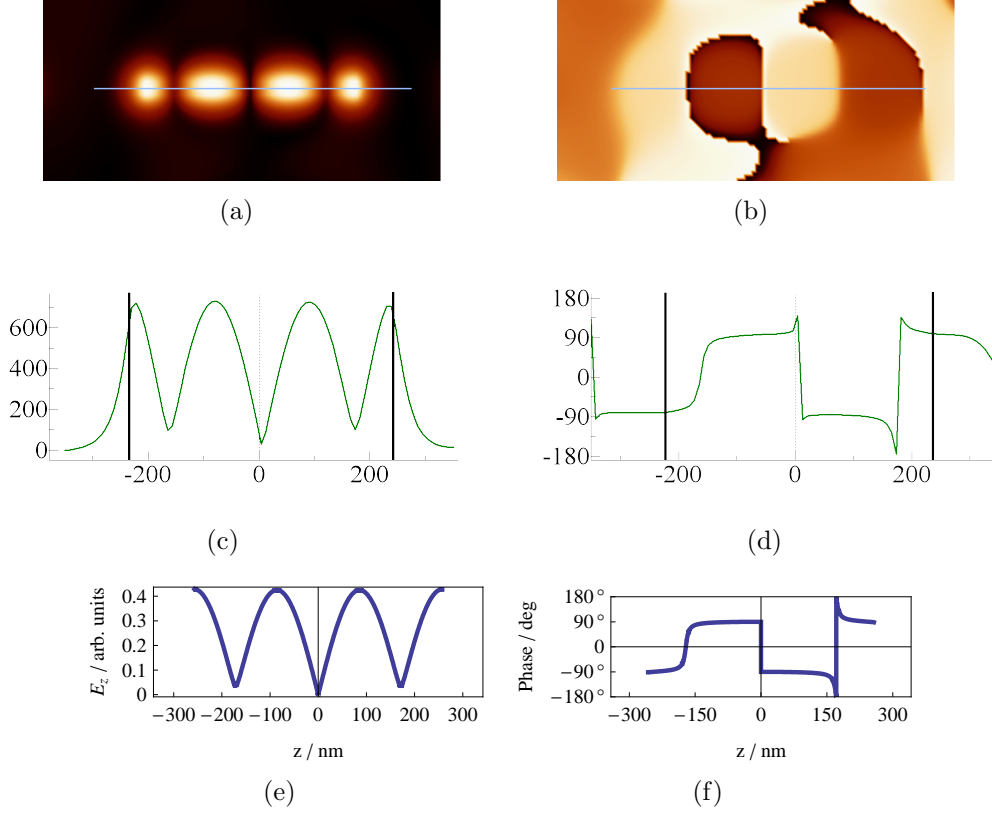


Figure 4.7.: Comparisons between the third order resonance in the simulation and the model: (a) and (b) show a zoom into the simulation of figure 4.2(a); The blue lines indicate the line cuts of (c) and (d); (e) and (f) show the amplitude and phase of the radial component calculated by equation 4.23.

describes the field directly at the surface. This difference gives the field some space to widen in the horizontal direction.

The right sides of figures 4.6 and 4.7 show the same comparison for the phase images. In the simulation as well as in the model two neighboring lobes show a phase difference of  $180^\circ$ . We conclude that the model can explain very accurately the radial, complex valued E-field around the metal nano-wires.

### 4.3.2. Geometric Resonances

The next challenge for the model is to explain the Fabry-Pérot resonances of the nano-wires. The length-amplitude plots we extract from the near-field images and the simulations contain only the maximum signal per wire. For the model we can do the same by numerically calculating the current  $I$  or the  $E_z$ -field-component for the complete wire and afterwards extracting the maximal signal. This is impractical for fitting the model to our data and thus we replace the proper signal function with a suitable proxy.

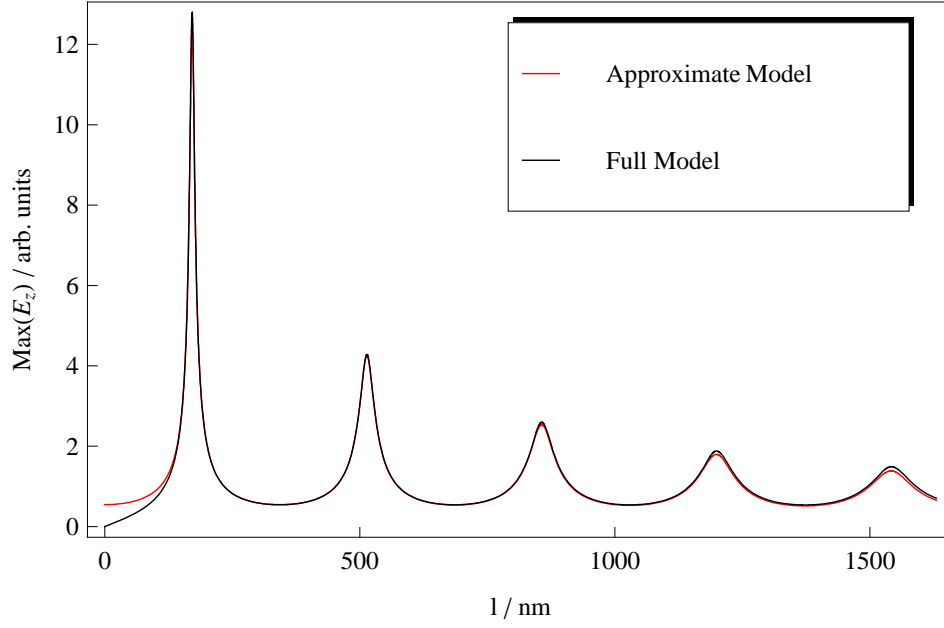
The current is an interferometric sum of three phasors ( $e^{\pm ik_p z}$ ,  $e^{ik_{\parallel} z}$ ) multiplied by respective amplitudes  $I_{\parallel}$ ,  $I_{+p}$  and  $I_{-p}$ . If on the scale of a wire length spatial oscillation is large ( $\text{Re}(k_p l) \geq 1$ ) but damping effects are small ( $\text{Im}(k_p l) \ll 1$ ), somewhere on the wire a maximum of the interferometric current sum will be attained which is well approximated by the sum of the absolute amplitudes: if the inverse of the imaginary part of  $k_p$  is large compared to the wire length,  $|e^{\pm ik_p z}|$  will be approximately 1. Thus we try to approximate the maximum current by the sum of the absolute valued of the three factors:

$$I_{\max} = |I_{\parallel}| + |I_{+p}| + |I_{-p}| \quad (4.24)$$

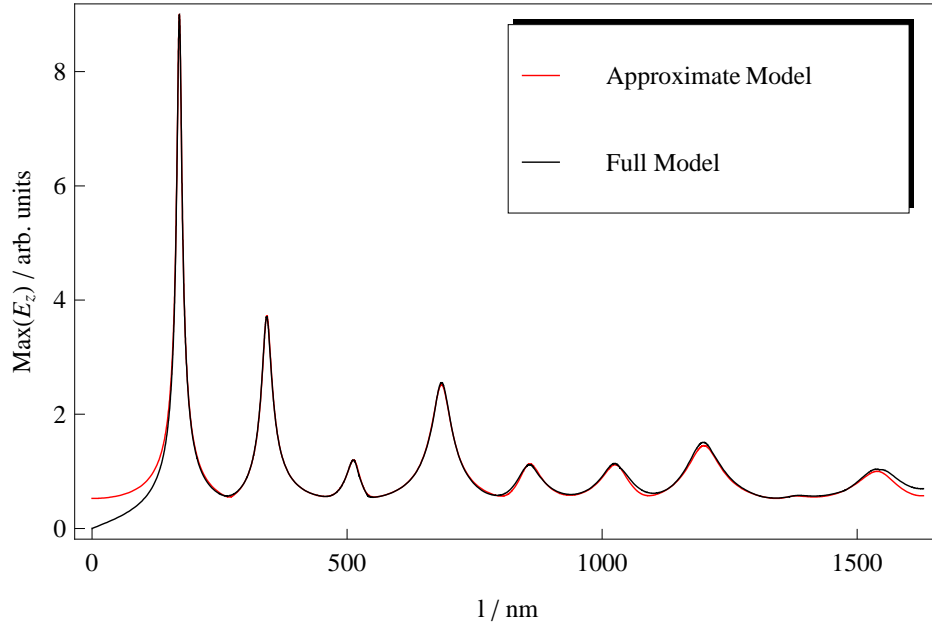
A similar approximation can be argued for the maximum of the field:

$$|E_r(a)|_{\max} \propto |k_{\parallel} I_{\parallel}| + |k_p I_{+p}| + |k_p I_{-p}| \quad (4.25)$$

Figure 4.8 shows a comparison between the maximal  $E_r$ -field extracted from the model and the analytical approximation of equation 4.25. Real and imaginary part of the k-vectors used for plotting are comparable to the values we observed in ex-



(a)  $\theta = 90^\circ$



(b)  $\theta = 45^\circ$

Figure 4.8.: Comparison between the complete model and the approximation from equation 4.25. The parameters used for producing these graphs are approximately the same we obtain from experiments and simulations:  $k_p = \frac{2\pi}{343} \text{ nm}^{-1} + i0.50 \mu\text{m}^{-1}$  and  $k = \frac{2\pi}{911} \text{ nm}^{-1}$ .

periments. The plots are typical examples for two illumination angles and show the good match between the approximate model and the full model. Only the region where the wires are shorter than the first resonance length (e.g.  $< 120$  nm) shows strong deviations, because on such short wires spatial oscillations are not fast enough to bring all partial currents “in-phase”.

When trying to fit the model to measured or simulated data another difficulty arises. The model proposed in this chapter does explicitly not include any effects of the wire ends. As we have seen in the last chapter, a phase pickup due to the end-caps’ reactance is not negligible. To include it into the model we follow ref. [104] and describe it as an apparent length increase:  $L_{\text{model}} = L_{\text{experiment}} + L_{\text{reactance}}$ . This introduces a necessary additional fitting parameter  $L_{\text{reactance}}$ .

One more fitting parameter turned out to be helpful to improve the fitting, an amplitude offset:  $E_{z,\text{offset}}$ . We first regard this parameter as purely empiric, later we will discuss the physical meaning of this parameter.

The simulations take the actual experimental illumination direction into account. The detailed description of the difference between the model and the experimental coordinate system is discussed in appendix A. In short, the substrate the wires are fabricated on forbids an illumination at exactly grazing incidence. We thus use an incidence illumination with a tilt angle of  $\alpha = 17^\circ$  off the substrate tangent. For an illumination direction perpendicular to the wire axis (rotation angle of the sample  $\psi = 0^\circ$ ) this is consistent with the geometry of the model at  $\theta = 90^\circ$ . But when rotating the sample the rotation angle of the sample  $\psi$  deviates slightly from  $\theta$ . The largest deviation occurs at a rotation angle of  $\psi = 90^\circ$  which matches with an angle  $\theta = \alpha$  of the model. To compensate for these coordinate system differences we use equations A.7 and A.10.

### 4.3.3. Simulation Data

The curves in figure 4.8 already look similar to the geometric resonance curves from chapter 3. Does the level of agreement allow to actually fit the model to the entire data set from all near-field images at once?

Some of these “length vs. maximum field” plots are shown in figure 4.9. The red curves show the fit of the simplified model to the data. The quality of the fits is remarkable. Only at lengths shorter than the dipole resonance the model deviates appreciably from the simulation data. As outlined in section 4.3.2, the failure in this regime is to be expected for the simplified model. The data for the rotation angle of  $\psi = 90^\circ$  show no significant peaks, the data points deviate little from the offset of about 80. This is consistent with the model which predicts no excitation of the longitudinal modes at this illumination direction.

To study the consistency of the model we first fitted the model to the resonance curves of each illumination angle individually. The five fitting parameters used in the model are all physically motivated and most of them can be obtained from or compared to other considerations:

- the real and imaginary part of plasmon k-vector:  $k_p = \frac{2\pi}{\lambda_p} + i\text{Im}(k_p)$ , where  $\lambda_p$  is the plasmon wavelength and  $\text{Im}(k_p)$  is the damping constant;
- amplitude  $A$  for the incident E-field;
- the apparent length increase  $L_{\text{reactance}}$ ;
- by adding a signal offset  $I_{\text{offset}}$  we improved the fitting; it will be connected to the excitation of higher order, transversal plasmonic modes;
- rotation angle  $\psi$ , which is a known parameter and only used as a consistency

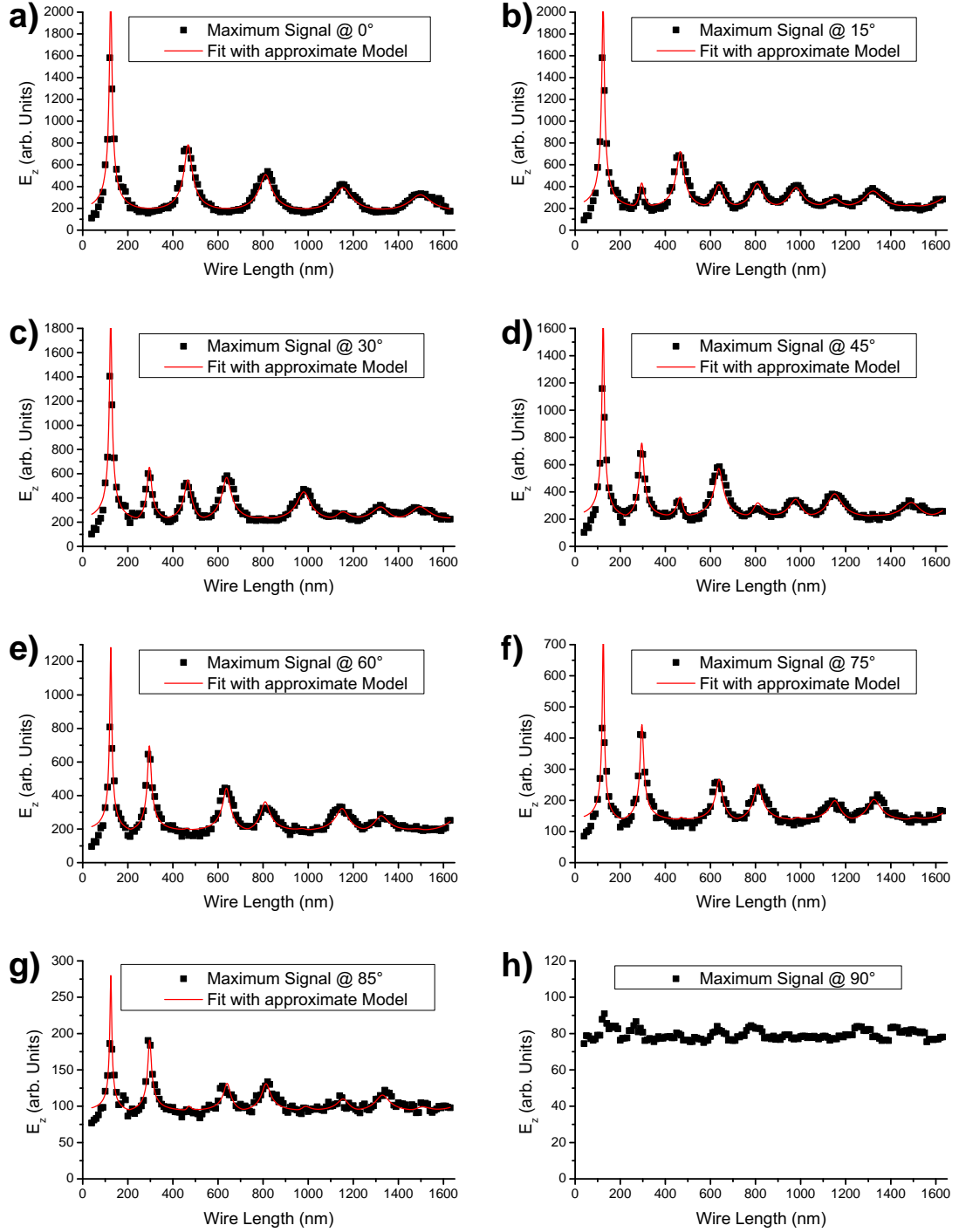


Figure 4.9.: The maximum of the z-component of the E-field 24 nm above the wire taken from FDTD simulations for different angles: (a)  $\psi = 0^\circ$ , (b)  $\psi = 15^\circ$ , (c)  $\psi = 30^\circ$ , (d)  $\psi = 45^\circ$ , (e)  $\psi = 60^\circ$ , (f)  $\psi = 75^\circ$ , (g)  $\psi = 85^\circ$ , (h)  $\psi = 90^\circ$ . The simplified model from equation 4.24 has been used to fit the data.

check;

For a systematic analysis, the angle dependence of the fitting parameters is plotted in figure 4.10. The plasmon wavelength 4.10(a) and apparent length increase 4.10(e) show no angle dependence. All measured values are distributed around 345 nm and 47 nm within their margin of error. The fitted amplitude 4.10(c) is also independent on illumination angle. This is very encouraging because it shows that all effects of the illumination angle on the amplitude are covered by the model. The rotation angle of the sample 4.10(d), which was included as a consistency check, is also retrieved by the fit algorithm within the fitting error. The damping constant 4.10(b) has a systematic dependence on the illumination angle. The fact that the damping constant  $\text{Im}(k_p)$  is decreasing with increasing rotation angle is astonishing and not yet understood.

The behavior of the signal offset 4.10(f) also leaves some open questions. Nevertheless, we can explain some trends we observe. At a rotation angle of  $90^\circ$  all wires give a similar strong signal. The fitting will assign most of the signal to the parameter offset. In the near-field images in figure 4.2(d) and 4.1(f) we can identify most of the signal as coming from the first transversal mode and not from any longitudinal mode. Going from higher illumination angles towards  $0^\circ$  the signal offset is decreasing. This makes sense in that the dipole moment of the first transversal mode is perpendicular to the excitation E-field. The fact that this mode is still excitable at a sample rotation angle of  $0^\circ$  may be surprising, but due to the symmetry breaking effect of the retarded grazing incidence illumination not impossible. In conclusion, we ascribe the signal offset parameter to the excitation of higher order transversal modes.

This shows that the model not only fits each data-set very well but also gives similar parameters for each illumination angle. This motivates us to attempt a

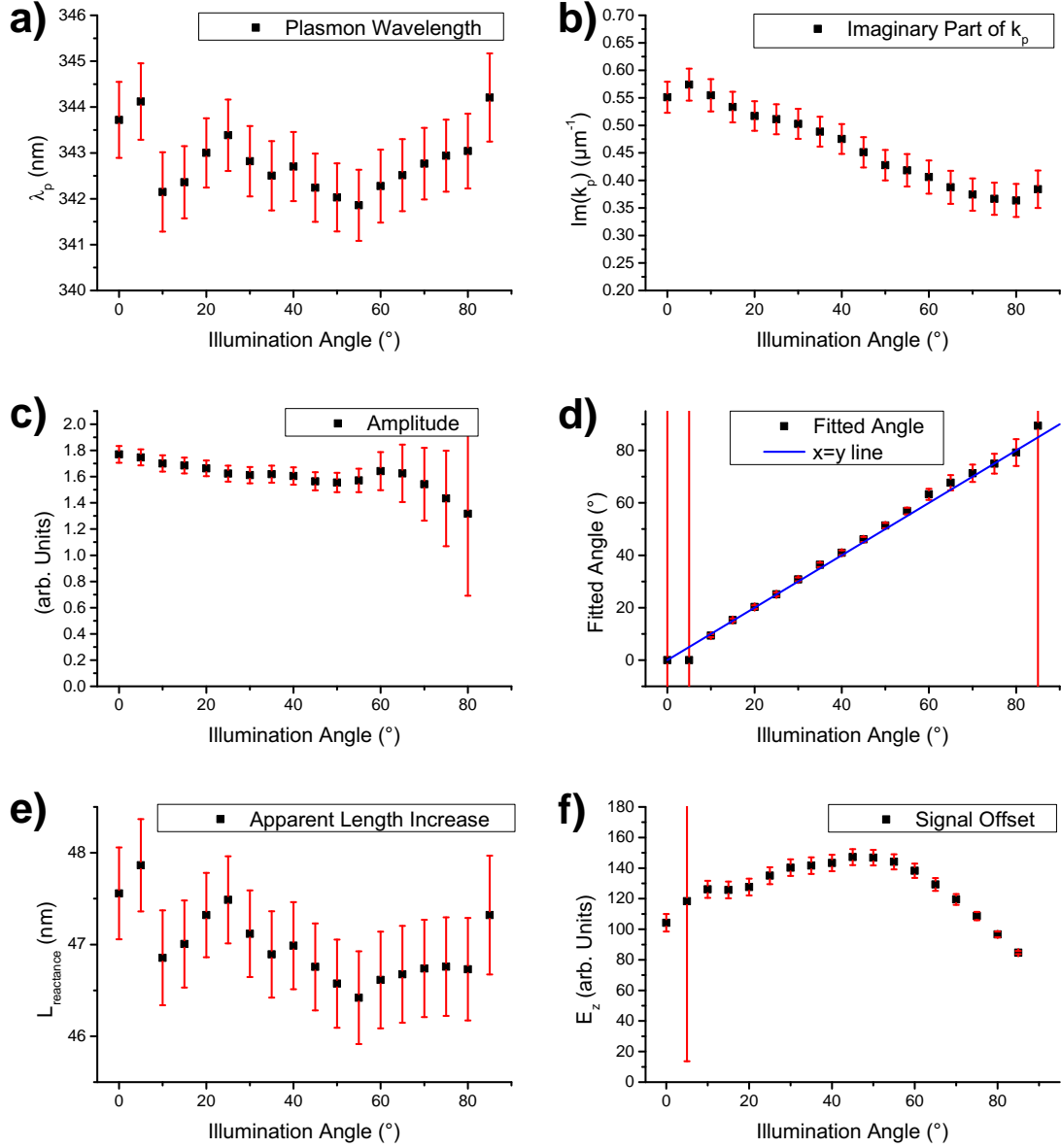


Figure 4.10.: Dependence of the fitting parameters on the illumination angles: (a) plasmon wavelength  $\lambda_p$ , (b) imaginary part of the plasmon wavevector  $\text{Im}(k_p)$ , (c) fitted amplitude, (d) fitted angle, (e) apparent length increase due to the reactance of the wire ends and (f) signal offset due to the excitation of the first transverse mode.

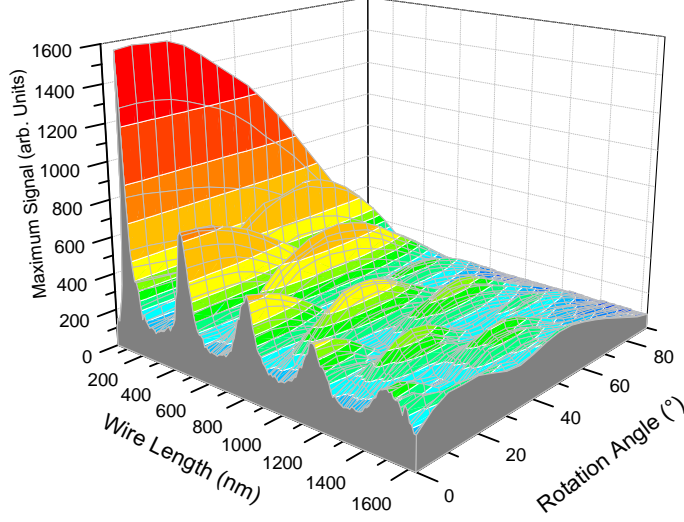


Figure 4.11.: Complete Data Set as 3D-Plot

global fit to the complete data set. This set is shown in figure 4.11 and comprises a total of 160 wires illuminated at 19 different angles. For the fit we use  $I_{\text{offset}}$  as a local parameter that will be fitted independently for each angle, use the nominal angle as illumination angle and use the other three parameters as global parameters. After the fit we can describe the whole data set of 3040 measurements by a global amplitude  $A$  and the following three parameters:  $\lambda_p = (342.86 \pm 0.18) \text{ nm}$ ,  $\text{Im}(k_p) = (0.4980 \pm 0.0066) \mu\text{m}^{-1}$  and  $L_{\text{reactance}} = (47.12 \pm 0.11) \text{ nm}$ .

#### 4.3.4. Experimental Data

After the simulations we here apply the model to our near-field experiments. Figure 4.12 shows the geometric resonance curves extracted from the near-field images. Compared to the numerically produced data, these curves contain somewhat more noise. Nevertheless, the resonances of the wires are clearly visible and our model

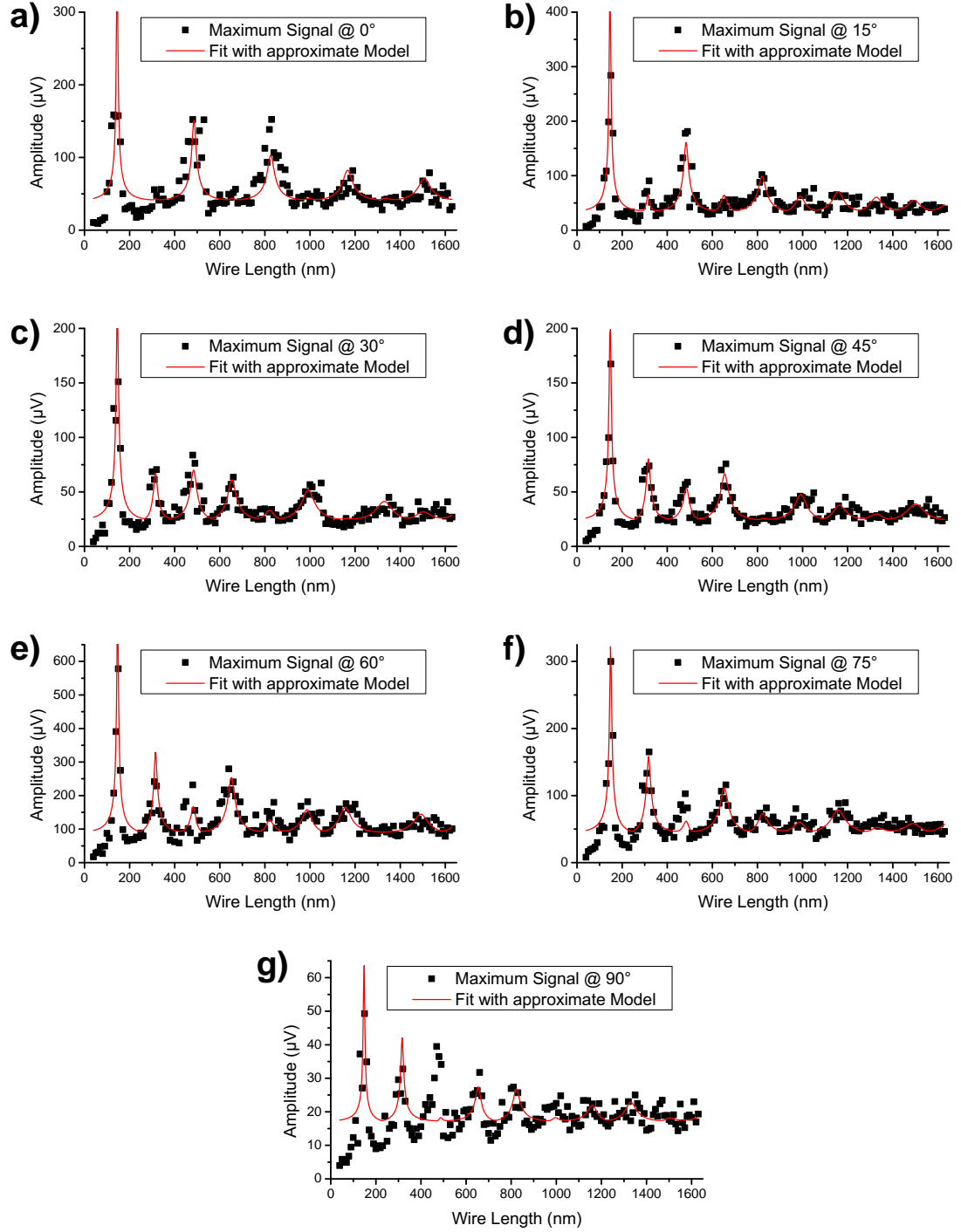


Figure 4.12.: The maximum of the measured near-field signal for different angles: (a)  $\psi = 0^\circ$ , (b)  $\psi = 15^\circ$ , (c)  $\psi = 30^\circ$ , (d)  $\psi = 45^\circ$ , (e)  $\psi = 60^\circ$ , (f)  $\psi = 75^\circ$ , (g)  $\psi = 90^\circ$ . The simplified model from equation 4.24 has been used to fit the data.

can easily fit the data very well.

As a first step we fit the individual measurements individually. The angle dependence of the five fitting parameters is shown in figure 4.13. The plasmon wavelength in 4.13(a) shows a much larger variation than the one we extracted from the simulation. The average values of  $\lambda_p$  of 338.6 nm matches the one in the simulations and differs only by 1.3%. The imaginary part of the plasmon's wavenumber in 4.13(b) shows the same strong variation as we observed in the simulation. Also the average value of  $\text{Im}(k_p)$  is comparable. Whereas before we saw a systematic dependence on the rotation angle, we can describe it here as noise.

The amplitude obtained from the fits cannot be interpreted physically. Each near-field image we obtain has to be regarded as separate experiment. In between two experiments usually the laser power varies and the tip has to be repositioned in the focus. Thus the illumination intensity and / or the backscattering efficiency changes from image to image. These effects result in a different amplitude for each near-field image and are observed in 4.13(c) as different fitted amplitude for each angle. Nevertheless, we can use the amplitude to normalize other fitted parameters, e.g. the signal offset.

While fitting the simulation data, the rotation angle was left as fitting parameter that showed the consistency of our model. Here the situation is more complicated. Figure 4.13(d) shows that the fitted angle deviates strongly from the condition Illumination Angle = Fitted Angle, indicated in blue. In the measurements at 45°, 60° and 75° the rotation angle obtained from the fitting algorithm is much smaller than the actual rotation angle. These systematic differences can be explained by the focussed rather than plane wave illumination that was used in our experimental setup.

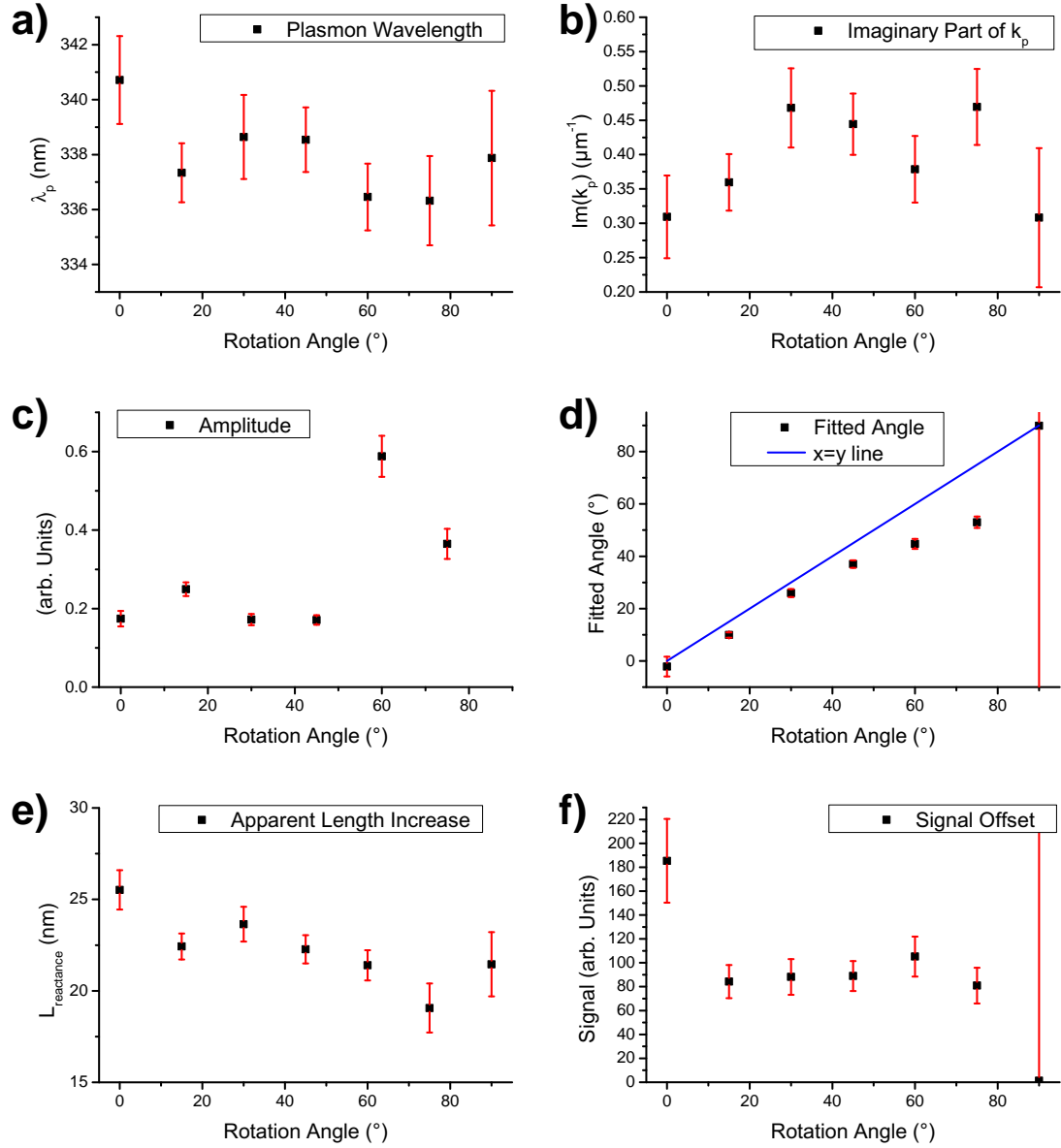


Figure 4.13.: Dependence of the fitting parameters on the illumination angles: (a) plasmon wavelength  $\lambda_p$ , (b) imaginary part of the plasmon wavevector  $\text{Im}(k_p)$ , (c) fitted amplitude, (d) fitted angle, (e) apparent length increase due to the reactance of the wire ends and (f) signal offset due to the excitation of the first transverse mode.

A Gaussian focus ( $\mathbf{E}(x, y, 0) = \mathbf{E}_0 e^{-(x^2+y^2)/w_0^2}$ ) can be presented in angular spectrum representation [103, eq. 3.9] as:

$$\hat{\mathbf{E}}(k_x, k_y; 0) = \frac{1}{4\pi^2} \iint_{-\infty}^{\infty} \mathbf{E}_0 e^{-\frac{x^2+y^2}{w_0^2}} e^{-i(k_x x + k_y y)} dx dy = \quad (4.26)$$

$$= \mathbf{E}_0 \frac{w_0^2}{4\pi} e^{-(k_x^2 + k_y^2) \frac{w_0^2}{4}} \quad (4.27)$$

By introducing an angle  $\Delta\alpha$  being the deviation from the main illumination direction and using the far-field equation  $k = \sqrt{k_x^2 + k_y^2 + k_z^2}$  we obtain:

$$\hat{\mathbf{E}}(\Delta\alpha; 0) = \mathbf{E}_0 \frac{w_0^2}{4\pi} e^{-k^2 \sin^2(\Delta\alpha) \frac{w_0^2}{4}} \quad (4.28)$$

Taking the inverse fourier transform brings us back to real space. Evaluating this expression at the center of the beam gives:

$$\mathbf{E}(x, y, 0) = \iint_{-\infty}^{\infty} \hat{\mathbf{E}}(\Delta\alpha; 0) e^{i(k_x x + k_y y)} dk_x dk_y \stackrel{x=y=0}{=} \int_0^{\frac{\pi}{2}} \hat{\mathbf{E}}(\Delta\alpha; 0) 2\pi k \cos \Delta\alpha d\Delta\alpha \quad (4.29)$$

This shows that illumination with a gaussian beam can be expressed as illumination by a sum of plane waves from multiple directions which are weighted by a (nearly) gaussian distribution around the main illumination direction  $\theta$ .

To study the different effects of this focussed illumination we numerically solved our model for a multidirectional illumination. We then used again our approximate model for the plane wave illumination to fit this artificial data. Depending on the direction from where the laser beam is focused onto the wires the rotation angle retrieved by fitting differs more or less from the main illumination direction. At perpendicular illumination,  $\theta = 90^\circ$ , the two angles are the same. Towards a rotation angle of  $\theta = 0^\circ$  the difference between the fitted and the real illumination direction

becomes larger. By those calculations we convinced ourselves that equation 4.28 explains the direction and the magnitude of the systematic deviations shown in figure 4.13(d).

The apparent length increase in 4.13(e) shows the same level of noise as the plasmon wavelength did. Otherwise we found no further systematic dependence on the rotation angle. The average value is lower than the one obtained in the simulations. This is not very surprising because in contrast to the simulations, where we modeled rectangular wires with flat end caps, in the experiment we have wires with end caps which are rounded by the production process. The signal offset in 4.13(f) has been normalized by the fitted amplitude.

As in the simulation, we can fit the complete data set globally. Due to the reasons mentioned earlier, however, we will not use the amplitude  $A$  as a global parameter. Because of the focussed illumination it is also not possible to set the rotation angle equal to the nominal angle. Instead we leave the rotation angle as a local fitting parameter. The values we obtain from the experiments are:  $\lambda_p = (337.52 \pm 0.51) \text{ nm}$ ,  $\text{Im}(k_p) = (0.387 \pm 0.020) \mu\text{m}^{-1}$  and  $L_{\text{reactance}} = (22.20 \pm 0.34) \text{ nm}$ . The fact that the apparent length increase in the experiment is smaller than in the simulation has been discussed earlier. The difference in the damping constant  $\text{Im}(k_p)$  however is surprising. The damping constant in the experiment is smaller than in the simulations. This means that in spite of the thermally evaporated gold used in the experiment the plasmon's propagation length is larger than the simulated one based on the permittivity of single crystalline gold [30]. Reasons for this unexpected deviation from the theory could lie in the fabrication process. For example, a slightly thicker wire in the experiment could lead to a higher quality factor of the resonator. One could also speculate that the shape of the wire termination could modify the

strength of the losses. This will be subject to further investigations.

## 4.4. Difference Between Normal and Plasmonic Antennas

In the last section we convinced ourselves that the model from section 4.2 describes our measurement results very well. In this section we now want to use the model and see what we can learn about the basic properties of nano-antennas from it.

The model addressed the question of the angle dependence of the excitability of a nano-antenna. According to the Rayleigh-Carson reciprocity theorem [123] the absorption spectrum of an antenna is equal to its emission pattern. This means, the absorption patterns obtained from our model are at the same time the emission patterns. This opens up a much larger scope than just interpreting our measurements. It can for example be used to calculate the emission pattern of a quantum dot [124] or a molecule coupled to nano-rod [17]. Especially when it comes to the directionality of the antennas, the model can help replace time consuming simulations through analytical expressions.

In figure 4.14 we use our model to plot the absorption / emission patterns of resonant plasmonic antennas. The antennas are oriented vertically in these plots. Unlike many antenna theory books we do plot the field strength  $E$  and not the intensity. The intensity can be obtained by simply squaring the plotted values. The plots show a somewhat idealized plasmonic antenna. In order to get a clearer image of the features we use a lower damping constant ( $\text{Im}(k_p) = 0.05 \mu\text{m}^{-1}$ ) than we obtained from our measurements. Nevertheless, the discussion of the main features holds true also for realistic antennas.

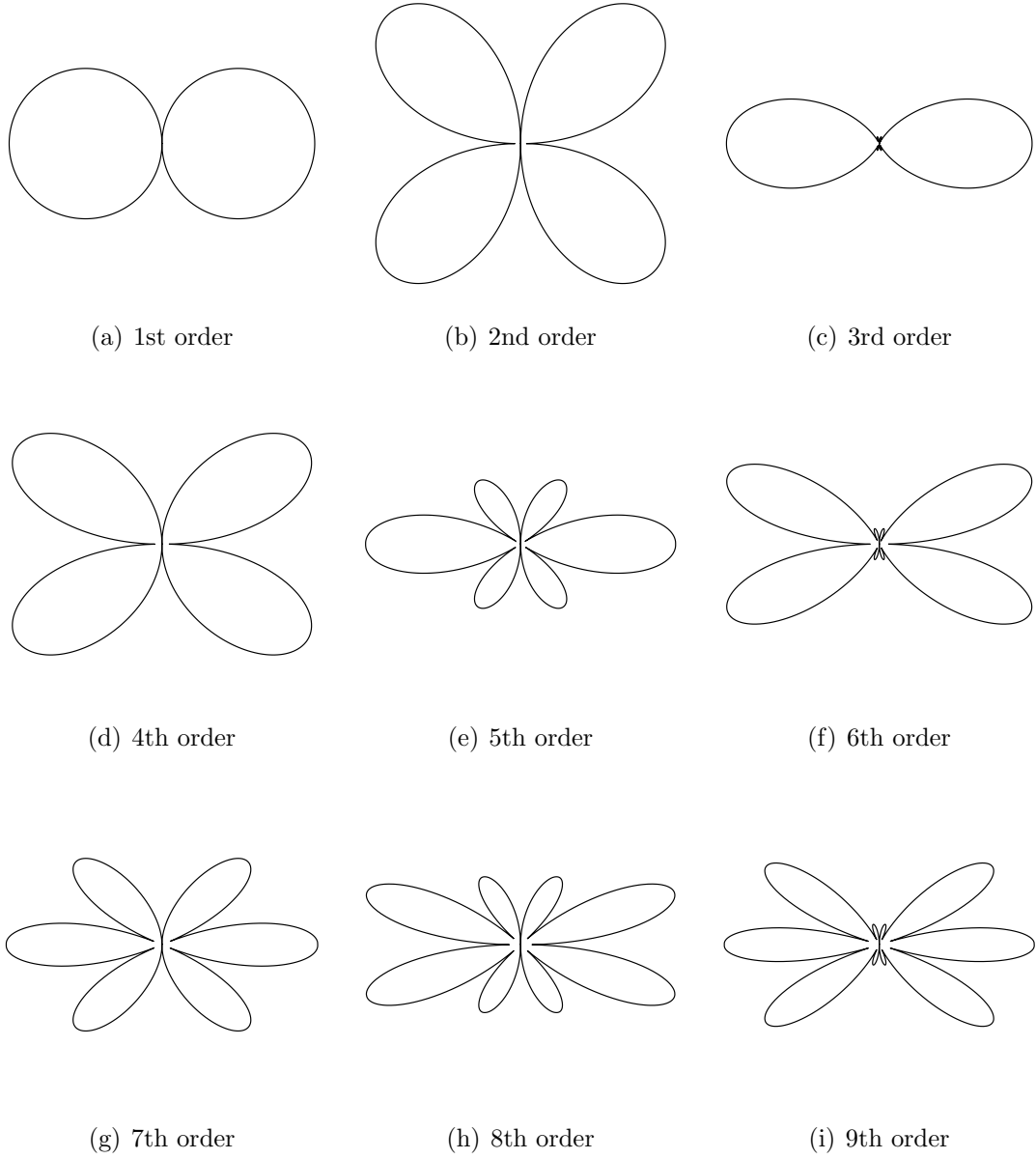


Figure 4.14.: Emission patterns of different order plasmonic antennas. The antennas are oriented vertically in these plots.

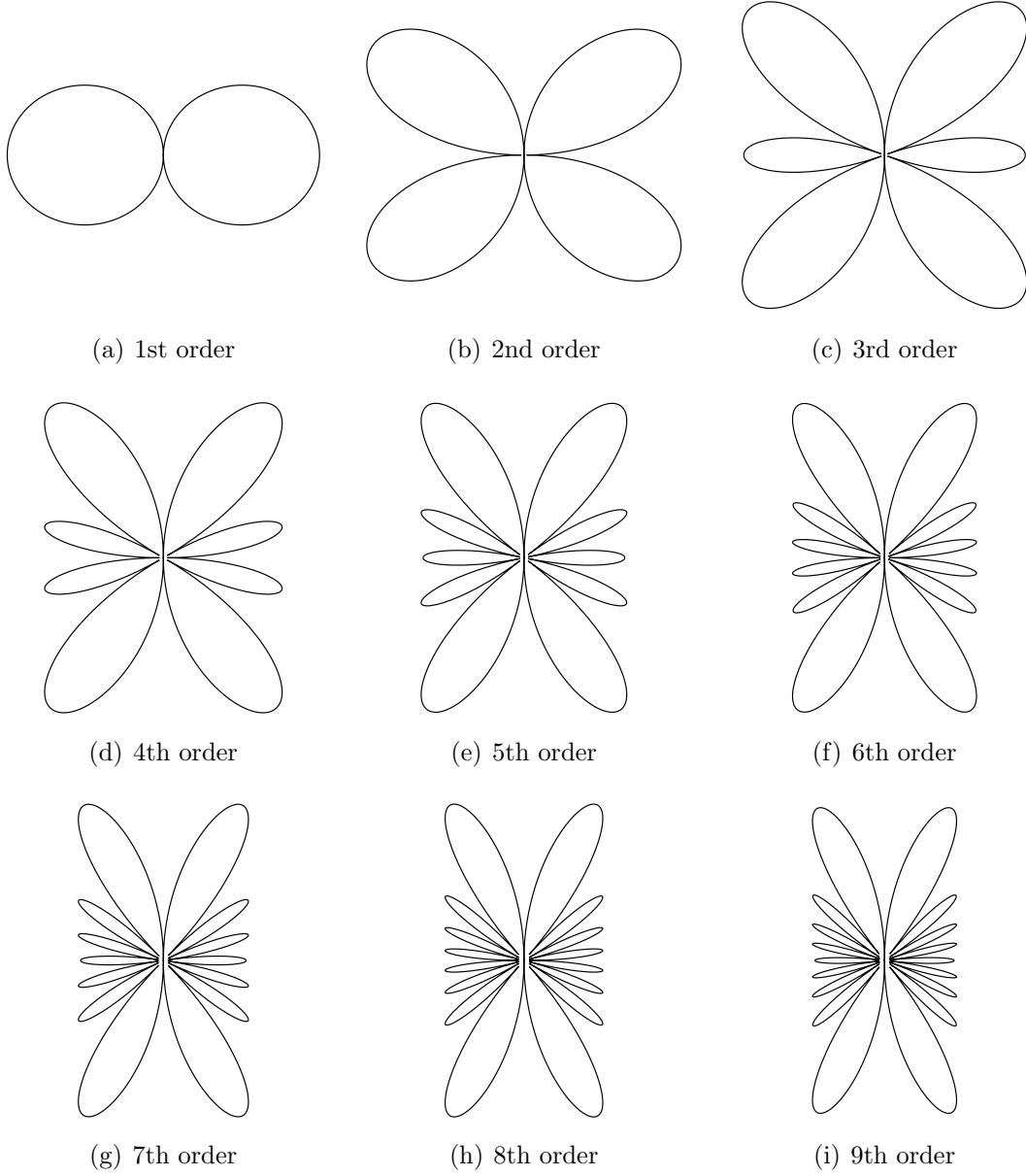


Figure 4.15.: Emission patterns of different order ordinary antennas. The antennas are oriented vertically in these plots.

The emission patterns of the first resonances look familiar. The first order mode shows the well known dipole pattern. The emission of the second order mode is a quadrupole. The third order mode has six lobes with four very weak lobes so that it does look more like a dipole. Interestingly, the next mode, the 4th order mode, resembles the second order mode. The 5th order mode differs from the 3rd order mode by stronger side lobes. Although some emission patterns of different resonance orders differ only slightly from each other, the trend to more lobes with higher order resonances is clearly visible. Nevertheless, the odd order modes always have their strongest emission into the direction perpendicular to the wire antenna. The even order modes in contrast have here always a minimum. This can of course be explained with the already familiar symmetry argument. The two lobes neighboring this minimum are always the strongest ones in the whole pattern.

By itself, these emission patterns look quite reasonable. But how do they differ from the ones of ordinary RF antennas? If our model is correct, it should be able to handle the limiting case of the plasmon approaching the vacuum wavelength. We try that by simply setting the parameter “plasmon wavelength” equal to the vacuum wavelength. Figure 4.15 shows the results of these plots. The mode pattern of the first order and the second order resonance are well known and shown in most textbooks. The hexapole and octapole patterns that we obtain for the third and fourth resonance can also be seen in some textbooks (i. e. [121, Fig. 1-12], [119, Fig. 3.8] and [125]). Up to here it seems that our model also gives the correct emission patterns for RF antennas. But the higher orders are shown only very rarely in books and we have no figures to compare. The only possibility to ensure the correctness of our higher order emission patterns is to compare them to a well established theory [114]. The perfect agreement between the two theories (not shown) lets us conclude

the plots presented in figure 4.15 are correct and our model is able to handle even the limiting case of the parameter  $\lambda_p$  approaching the vacuum wavelength.

The different order emission patterns of RF wire-antennas follow two basic rules. On the one hand the number of lobes increases by two from one resonance to the next, so that the  $n$ th order resonance has  $2n$  lobes. On the other hand, the lobes forming the smallest angle with the wire axis have the strongest emission. These two rules do not hold true for plasmonic antennas anymore. The plasmonic antennas we investigated, characterized by a plasmon wavenumber 2.65 times the vacuum wavenumber, follow the lobe number rule up to the 3rd order. The 4th, 5th and 6th order resonances have only  $2n - 4$  lobes, the 7th, 8th and 9th order resonance only  $2n - 8$  lobes. Finding a rule for the number of lobes of plasmonic antennas is difficult because the number of lobes for higher order resonances depends strongly on the ratio between the vacuum wavelength and the plasmon wavelength. But a trend that has been observed is that the deviation from the  $2n$ -lobes rule is stronger the larger the ratio  $\lambda/\lambda_p$ .

The plots show also that plasmonic antennas do not necessarily have their strongest emission into the lobes closest to the wire axis. In fact, for our antennas we observe the opposite. All the emission patterns of our wire antennas show the strongest emission into the lobes pointing closest to the direction perpendicular to the wire axis.

With the help of the model we can even investigate where these differences come from. Instead of just comparing the two we can also study how the transition from plasmonic to an RF antenna happens. The parameter determining how plasmonic an antenna is the proportion  $k_p/k$ . As an example, in figure 4.16 we look at the 7th order mode. From the original proportion  $k_p/k$  of 2.66 that characterized our wires

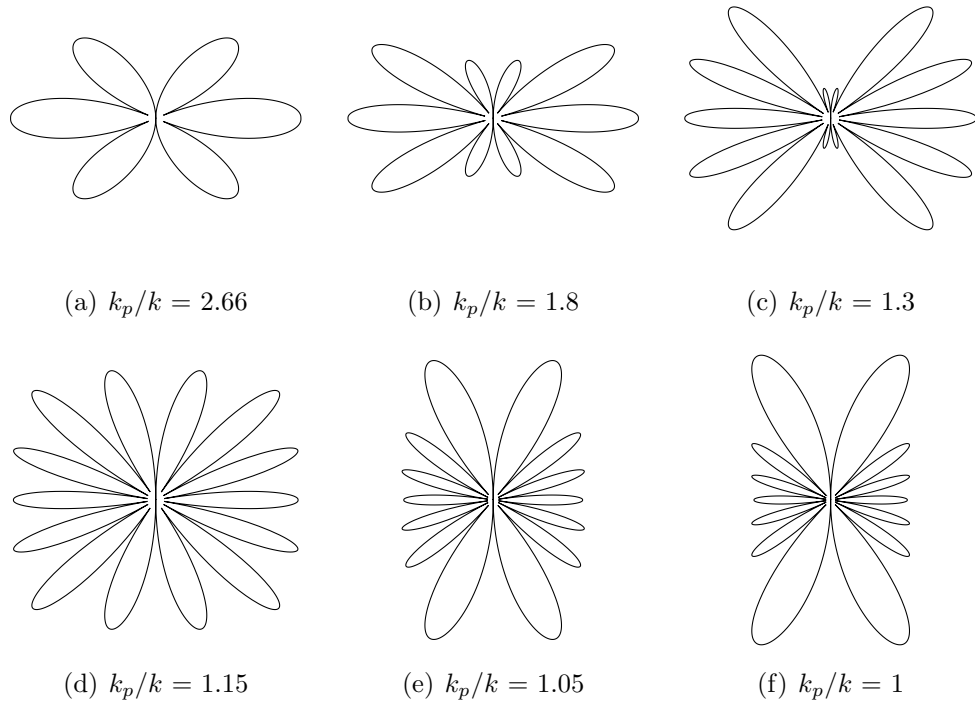


Figure 4.16.: Transition of a plasmonic into a RF antenna

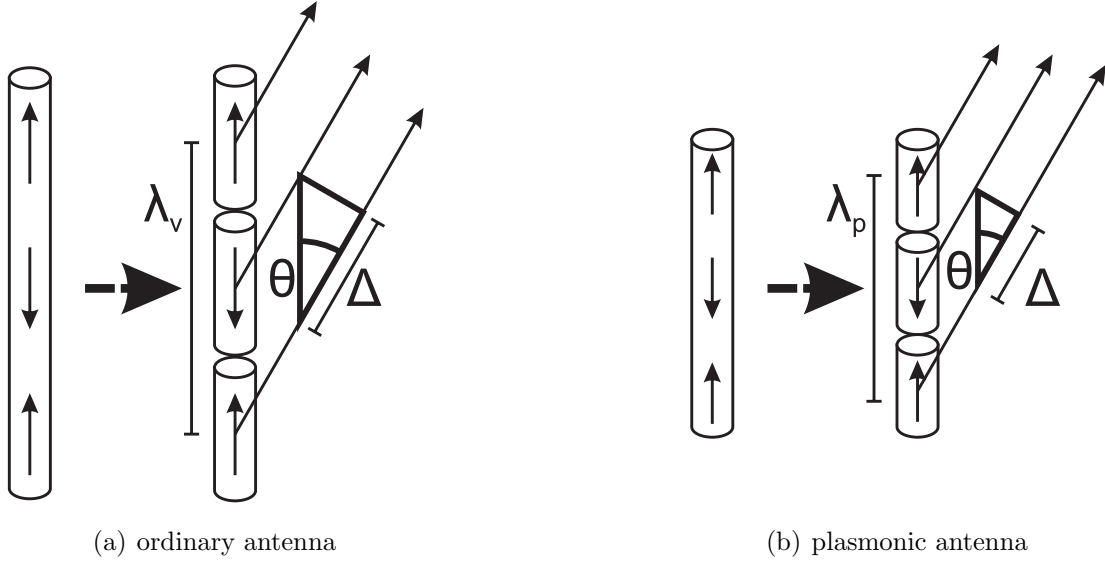


Figure 4.17.: The emission pattern of an antenna can be explained by interference of the different currents on the wire in the far field.

in the experiment and the simulation, we gradually change  $\lambda_p$  to  $\lambda$  while keeping the antenna length on resonance at  $3.5\lambda_p$ . From 4.16(a) to (b) the four side lobes crowd towards the center lobe and make space for four additional lobes. Figure 4.16(c) shows how these four new lobes grow stronger and also move towards the center. They make space for the last four lobes that are needed to fulfill the  $2n$ -lobes rule of RF antennas. In the figures 4.16(d) to (f) the outermost side lobes grow stronger and become the strongest lobes of the RF-antenna.

How can this dramatic effect on the emission patterns be understood, what is the physics behind it? Figure 4.17 shows the scheme of a third order resonance. We can think of the emission as a vector potential produced by currents on the linear antenna. In case of an ordinary, RF antenna (4.17(a)) two current lobes with the same directionality have a center-to-center distance of  $\lambda$ . The total E-field produced by these currents in the far-field will depend on the observation direction  $\theta$ . If we

forget for a moment that we have a continuous current distribution along the wire and think of three individual short currents it becomes clear that the resulting E-field is a result of the interference between these currents. It is obvious that the path length difference  $\Delta = \lambda \cos \theta$  is the parameter determining constructive or destructive interference. When we do the transition to plasmonic antennas while keeping the resonance order, we change the distance between two neighboring currents from  $\lambda/2$  to  $\lambda_p/2$  and thus  $\Delta$  becomes smaller. This is comparable to the behavior of the maxima in a multiple-slit pattern (see [126, ch. 10.2]). In the pattern of a  $N$  slit grating with a center-to-center slit separation  $a$  the angular position  $\theta_m$  of the  $m$ th principle maximum is given by:

$$\sin \theta_m = \frac{m\lambda}{a} \quad (4.30)$$

With the slit-to-slit distance becoming smaller the maxima move further apart from each other. The same happens to the lobes of our antennas, the lobes spread out further from each other and one lobe after another disappears.

While this analogy is very helpful to understand why plasmonic wire antennas have fewer lobes than their RF counterparts, in many other respects this analogy does not hold true. In contrast to the slits in Fraunhofer diffraction do our antenna pieces (indicated by arrows in figure 4.17) have an alternating direction. Thus, the antenna does not have principle maximum at  $\theta = 90^\circ$ , it has a subsidiary maximum or a minimum. In fact, the maxima observed as lobes of a linear wire antenna are always subsidiary maxima and never principal ones. Only RF antennas have the chance of fulfilling the interference condition for a principle maximum of  $\Delta = \lambda$ . Unfortunately this condition is only fulfilled for the angles  $\theta = 0^\circ$  and  $180^\circ$  and equation 4.1 tells us that there will no transversal E-field component for these two

angles. Thus there is no emission into these directions and what we see as the emission maxima of an RF antenna are only the next subsidiary maxima.



# Chapter 5.

## Summary and Outlook

### 5.1. Summary

This thesis discussed the properties of optical wire antennas. We use an apertureless SNOM to investigate such wires experimentally in the near-field regime. The cross-polarization configuration explained in chapter 2 turns out to be well suited for field mapping around the structures with only little disturbance of the eigenmodes. When the microscope is well aligned it is possible to obtain background free images in which the measured signal resembles the E-field component parallel to the probing tip. The good agreement between simulations of the structures without including the tip and our measurements lets us conclude that the influence of the tip on the antenna resonances we observe is small.

Although we are able to investigate a large range of different structures [101,127], we concentrate here on metal nano-wires. The plasmon excitation of the wire is essentially 1-dimensional and the resonances can be described in a Fabry-Pérot picture. We extract resonances by analyzing the near-field strength above the wires.

By varying the illumination direction we realized how non-symmetric illumination allows the excitation of otherwise symmetry forbidden modes. We took this discussion even further by measuring the angle dependent excitability of the 9 lowest order modes. The near-field imaging technique allows a simple interpretation of the data because the near-field amplitude is a direct measure of excitation strength. This is a big advantage over scattering experiments where excitation and emittance have both a directionality that has to be taken into account.

The results we obtained from simulation and experiment motivated us to search for an analytical description for the directionality of the excitability of plasmonic wire antennas. Inspired by RF antenna theory, we describe the excitation of the wires as a current distribution. While RF theories assume a perfect conductor and thus only expect surface currents, we include the possibility of volume currents. Our model uses four physically reasoned parameters to describe a wire antenna: the plasmon wavelength, the plasmon damping, the phase the plasmon suffers upon reflection and the length of the wire. With two more parameters (an amplitude offset due to the excitation of higher order modes and an overall amplitude) we are able to fit our complete data sets.

## **5.2. Outlook**

While our formulas allow only to calculate the current distribution on the wire upon illumination, the relevance is much larger. Due to reciprocity, the obtained directionality maps describe both, the excitation and the emission process. A combination of the two equations 4.16 and B.4 describes the complete scattering process and will advance the understanding of optical antennas significantly.

It allows to interpret scattering experiments on single wire antennas. As Mie

theory for metal spheres, this theory can predict the transmission, the extinction and the absorption of light by small wire antennas. This fact is already interesting for current state of the art research [128]. With scattering experiments often being much easier to carry out than near-field investigations, the well understood scattering properties can speed up research.

### 5.2.1. Antenna Arrays

A field of research where calculations of scattering by metal nano-wires can have an immediate effect is the investigation of antenna arrays. In designs where the antennas are far enough apart so that the coupling can be neglected the emission pattern of an array can be calculated by the interference of the individual antennas [114, 121, 129]. For an array of wires, the design parameter length can already have an interesting effect. For example, wires shorter than the dipole resonance are resonators in phase with the excitation field while a little longer wires are out of phase [130, 131]. With our method, which included the emission pattern of wire antennas as well as the resonator properties of the wire, analytical calculations can be used for optimizing these structures.

Flat antenna arrays can be produced very easily by standard lithography methods. They could, e.g., be useful for the enhancement of the (directed) outcoupling of radiation from light emitting diodes (LEDs) [132]. In a similar fashion, plasmonic structures are already used to enhance the efficiency of thin-film solar cells. Metal wire structures on the backside of the solar cell direct light into waveguide modes and increase the probability of photon absorption [133]. But also three dimensional structures are possible to fabricate today [26, 134]. This combination of antennas already lead to the development of metamaterials with extraordinary properties.

Especially in these structures it turns out that coupling between individual antennas cannot be ignored anymore [135] and has to be included into the theory.

### 5.2.2. Nonlinear Plasmonics

In the regime of nonlinear optical effects [136], there is still a lack of experimental data. Although models have been already proposed [137] only a few experiments on the single particle level have been carried out so far [138–140]. The enhancement of nonlinear effects is expected to scale with the enhancement factor of the structure for the involved wavelengths [141]. This would of course mean that the frequency conversion would be strongest if the resonator is resonant to all involved wavelengths [142]. This has not yet been observed in experiments. On the contrary, some experiments can not yet be fully explained by analytical models [143].

The easiest way to answer these question would be by far-field scattering experiments. Illuminating individual nano wires with a pulsed, focused laser beam and determining the higher harmonic scattering intensities and directional patterns would be one possibility. Illumination by two beams and detection of the sum- or difference-frequency signal in dependence of the illumination intensities would give an even better insight [144].

With the introduced model the linear parts, namely the excitation, absorption and emission, of the experiments on wire antennas can be explained for all wavelengths. This leaves only the nonlinear parameters as unknowns. For more complicated structures than wires, there are even predictions of enhancement effects due to magnetism [145].

### 5.2.3. Coupling Between Antennas

First investigations on more complex optical antennas have already been carried out by simulations [146]. Here, the difficulty arises that there is not yet a model fully describing the properties of the coupled antennas. But especially the interaction between several antennas gives rise to some interesting new effects. The coupling makes it necessary to find a concept similar to the impedance matching in the RF-regime [147].

The coupling is not only a challenge for theoretical predictions, it has a great potential for new applications. By controlling the coupling strength between resonators, it is possible to create peaks and dips in the resonance curve of the combined system which are much sharper than the original resonances [100]. With the plasmonic analogue to electromagnetic induced transparency (EIT) is possible to build ultra-sensitive bio detectors [99, 148] with a very small detection volume. Another way to achieve high quality factor structures is to utilize the magnetic field to store energy, e. g. in split ring resonators [149, 150]. Including this effect into the theoretical model could also be tried.

The theory we derived in this thesis is a first step towards a better understanding of plasmonic antennas. Including coupling effects as they are described today by simple hybridization models [97] will be a next step. With a full model at hand, the optimization of such sensor structures will change the empirical approach used today to systematic research.



## Appendix A.

# Consideration of the Experimental Situation

In section 4.2 we described a model that explains the absorption patterns of wire antennas, no matter whether they are plasmonic or RF antennas. For the mathematical description we used, as common in antenna theory, a spherical coordinate system with the wire centered in the symmetry axis (see figure A.1(a)). This is a different coordinate system than the one we used in the experiment (figure A.1(b)). Although not obvious at first sight, this change of coordinate system will have an effect on the coupling efficiency of the light to the wire. In this chapter we will derive the necessary coordinate transformation to correct for the errors that would otherwise appear for illumination angles  $\theta$  close to  $0^\circ$  or to  $180^\circ$ .

In contrast to the model, in the experiment the wire is placed on a substrate. In figure A.1(b) the substrate is filling out the Volume left of the  $x'-y'$ -plane. The substrate forces us to illuminate at a grazing incidence angle  $\alpha$ . Rotating the sample can be described as changing the rotation angle  $\psi$ . As indicated, the illumination

vector moves along a small circle of the sphere. In contrast to this, the illumination vector in the model moves along a great circle of the sphere when varying illumination angle  $\theta$ . For small angles  $\alpha$  the difference between two coordinate systems will become small and the experimental illumination angle  $\psi$  will nearly resemble the illumination angle of the model  $\theta$ .

There is a second, more severe effect that we have to consider. In the model we always presume illumination with an E-field amplitude  $E_0^{(\text{inc})}$  and a polarization parallel to the tangential vector  $\mathbf{e}_\theta$ . In the experiment the polarization will stay always parallel to the tangential vector  $\mathbf{e}_\psi$ . Again, for  $\alpha = 0^\circ$  model and experiment are equivalent from a physics point of view. The two angles do only have different names: the illumination angle  $\theta$  in the model and the rotation angle  $\psi = 90^\circ - \theta$  in the experiment. For  $\alpha \neq 0$ , i. g.  $\alpha = 17^\circ$  in our experiment, the two angles  $\theta$  and  $\psi$  differ when approaching  $\theta \approx 0^\circ$  or  $\psi \approx 90^\circ$ . The two polarization vectors,  $\mathbf{e}_\theta$  and  $\mathbf{e}_\psi$ , will even become perpendicular to each other when  $\psi = 90^\circ$ .

## A.1. Coordinate Transformation

To compare the model with the experiment, we transform the experimental coordinates into the model coordinate system. A vector  $\mathbf{r}$  can be described in the experiment's coordinate system as:

$$x' = r \sin(90^\circ - \alpha) \cos \psi \quad (\text{A.1})$$

$$y' = r \sin(90^\circ - \alpha) \sin \psi \quad (\text{A.2})$$

$$z' = r \cos(90^\circ - \alpha) \quad (\text{A.3})$$

In the model coordinate system we can describe the same vector by the following

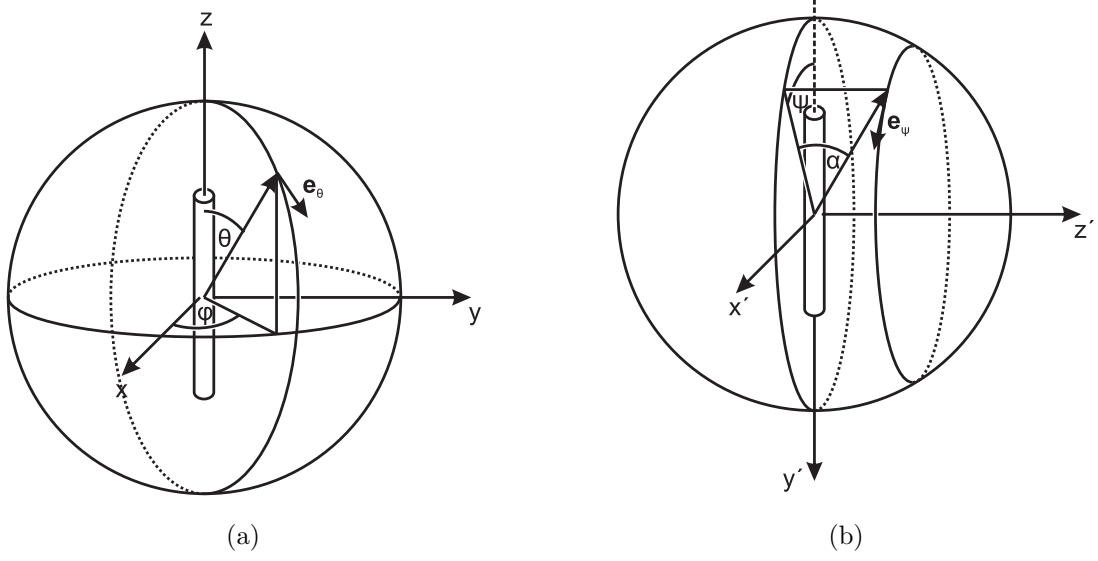


Figure A.1.: (a) the coordinate system used in the model; (b) the coordinate system used in the experiment; the angle used in the experimental and simulated data is  $\varphi$  while  $\alpha \approx 17^\circ$  is given by the periscope used in the experiment;

coordinates:

$$x = r \sin \theta \cos \varphi \hat{=} x' \quad (\text{A.4})$$

$$y = r \sin \theta \sin \varphi \hat{=} z' \quad (\text{A.5})$$

$$z = r \cos \theta \hat{=} -y' \quad (\text{A.6})$$

In these equations we also indicated how to connect these two coordinate systems.

From these relations it follows that:

$$\theta = \arccos(\sin(90^\circ - \alpha) \sin \psi) = \arccos(\cos \alpha \sin \psi) \quad (\text{A.7})$$

This equation allows us to calculate the illumination angle  $\theta$  for a given grazing incidence angle  $\alpha$  and a rotation angle  $\psi$ . It also shows that for the experimental

head-on-illumination,  $\psi = 90^\circ$ , the minimally reached  $\theta$  is equal to  $\alpha$ . This makes sense since in the real experiment, there will never be an illumination direction parallel to the wire axis.

## A.2. Projection of the Polarization Vector

The model supposes a polarization vector that is parallel to the plane spun by the angle axis and the illumination direction. As you can see in figure A.1(b), this does not hold true for the configuration of the experiment. In order to compensate this difference we will now calculate the projection of the experiments E-field vector, which is parallel to  $\mathbf{e}_\psi$ , onto the E-field vector of the model, which is parallel to  $\mathbf{e}_\theta$ . We start by describing the two unit vectors in their own coordinate systems  $x', y', z'$  and  $x, y, z$  respectively:

$$\mathbf{e}_\psi = \frac{\frac{\partial \mathbf{r}}{\partial \psi}}{\left| \frac{\partial \mathbf{r}}{\partial \psi} \right|} = \begin{pmatrix} -\sin \psi \\ \cos \psi \\ 0 \end{pmatrix} \quad (\text{A.8})$$

$$\mathbf{e}_\theta = \frac{\frac{\partial \mathbf{r}}{\partial \theta}}{\left| \frac{\partial \mathbf{r}}{\partial \theta} \right|} = \begin{pmatrix} \cos \theta \cos \varphi \\ \cos \theta \sin \varphi \\ -\sin \theta \end{pmatrix} \quad (\text{A.9})$$

The projection of the experimental E-field vector onto the one of the model can be described by the scalar product of the two unit vectors. Calculating the product

in the the coordinate system of the model leads to a factor:

$$f = \mathbf{e}_\psi \cdot \mathbf{e}_\theta = \begin{pmatrix} -\sin \psi \\ 0 \\ -\cos \psi \end{pmatrix} \cdot \begin{pmatrix} \cos \theta \cos \varphi \\ \cos \theta \sin \varphi \\ -\sin \theta \end{pmatrix} = \frac{\cos \psi}{\sqrt{1 - \cos^2 \alpha \sin^2 \psi}} \quad (\text{A.10})$$

By multiplying this factor  $f$  to the incident field, we can account for the different polarizations used in the experiment and in the model:

$$E_{0,\text{exp}}^{(\text{inc})}(\alpha, \psi) = f E_0^{(\text{inc})} \quad (\text{A.11})$$

When we now take everything together we can calculate the z-component of the illumination E-field:

$$E_{z,\text{exp}}^{(\text{inc})}(z, \alpha, \psi) = f E_0^{(\text{inc})} \sin \theta e^{ik \cos \theta} = \quad (\text{A.12})$$

$$= \frac{\cos \psi}{\sqrt{1 + \cos \alpha \sin \psi}} E_0^{(\text{inc})} e^{ik \cos \alpha \sin \psi} \quad (\text{A.13})$$

This is the expression we are using instead of equation 4.1 for the incident field when fitting the experimental or simulated data.



## Appendix B.

# Emission Pattern of an Infinite Thin Wire

In chapter 4 we derived the equations to describe the absorption of a linear plasmonic antenna. As we saw later, the model does not only describe the wires correctly on the resonance but was also able to describe the regions between the resonances. This property makes it quite complex and we had to obtain the maximum current on the wire numerically in order to obtain the absorption / emission patterns. If you are interested only in the emission pattern of resonant wires, you can use a simpler equation that we will derive in this appendix.

The derivation is inspired by chapter 9 of the book of J. D. Jackson [113]. It is much shorter and quite straight forward. Nevertheless, the equation we are about to derive still can explain all the observations about plasmonic emission patterns described in section 4.4. These two properties make it a good and rewarding exercise for students.

In section 4.2 we saw that the current on a wire antenna can be described by

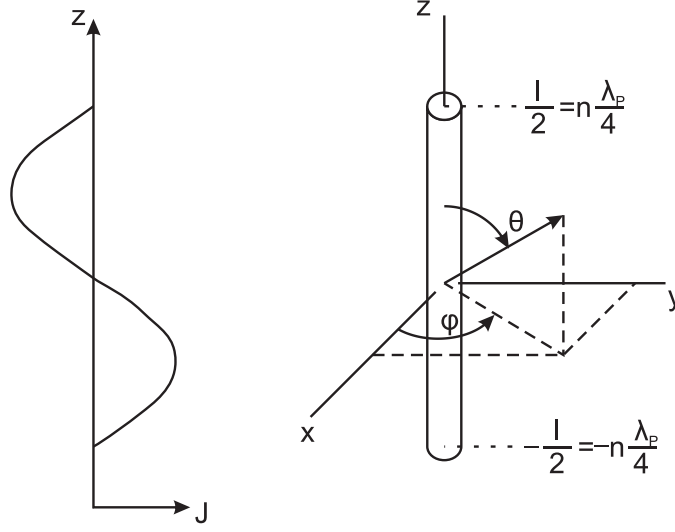


Figure B.1.: Scheme of the emission model

three components: a current induced by an excitation and two counter propagating plasmonic currents. At the  $n$ th order resonance, when the wire has a length  $d = n \frac{\lambda_p}{2} = \frac{n\pi}{k_p}$ , the induced current wave  $I_{\parallel} e^{ik_{\parallel}z}$  will be negligibly small compared too the two counter propagating plasmonic currents. Together with the condition of a vanishing current at the wire ends we obtain a nearly sinusoidal current distribution  $\mathbf{J}(\mathbf{x})$  (compare [113, eq. 9.53]):

$$\mathbf{J}(\mathbf{x}) = I_0 \sin\left(\frac{k_p d}{2} - k_p z\right) \delta(x) \delta(y) \mathbf{e}_z \quad (\text{B.1})$$

$$= I_0 \sin\left(\frac{n\pi}{2} - k_p z\right) \delta(x) \delta(y) \mathbf{e}_z \quad (\text{B.2})$$

where  $k_p$  is the plasmon wavelength. In this equation we also approximated our thin wires with an infinitely thin wire.

Now we can calculate the effect of this current distribution as a vector potential

---

$\mathbf{A}(\mathbf{x}, t)$  in Lorenz gauge and with sinusoidal time dependence [113, eq. 9.3]:

$$\mathbf{A}(\mathbf{x}) = \frac{\mu_0}{4\pi} \int \mathbf{J}(\mathbf{x}') \frac{e^{ik|\mathbf{x}-\mathbf{x}'|}}{|\mathbf{x}-\mathbf{x}'|} d^3x' \quad (\text{B.3})$$

where  $k$  is the vacuum wavelength and the integral runs over the volume of the wire.

Since we are only interested in the far-field emission patterns ( $|\mathbf{x}| \gg |\mathbf{x}'|$ ) we can approximate  $|\mathbf{x}-\mathbf{x}'| \approx r - \mathbf{n} \cdot \mathbf{x}'$ , with  $r = |\mathbf{x}|$  and  $\mathbf{n}$  is the unit vector in the direction  $\mathbf{x}$ . Equation B.3 now simplifies to:

$$\lim_{kr \rightarrow \infty} \mathbf{A}(\mathbf{x}) = \frac{\mu_0}{4\pi} \frac{e^{ikr}}{r} \int \mathbf{J}(\mathbf{x}') e^{-ik\mathbf{n} \cdot \mathbf{x}'} d^3x' \quad (\text{B.4})$$

Inserting  $\mathbf{J}(\mathbf{x})$  from equation B.2 leads to:

$$\lim_{kr \rightarrow \infty} \mathbf{A}(\mathbf{x}) = I_0 \mathbf{e}_z \frac{\mu_0}{4\pi} \frac{e^{ikr}}{r} \int_{-\frac{n\pi}{2k_P}}^{\frac{n\pi}{2k_P}} \sin\left(\frac{n\pi}{2} - k_P z'\right) e^{-ikz' \cos \theta} dz' \quad (\text{B.5})$$

The trigonometric equality  $\sin(\alpha \pm \beta) = \sin \alpha \cos \beta \pm \cos \alpha \sin \beta$  lets us separate the sum inside of the sine:

$$= I_0 \mathbf{e}_z \frac{\mu_0}{4\pi} \frac{e^{ikr}}{r} \int_{-\frac{n\pi}{2k_P}}^{\frac{n\pi}{2k_P}} \left( \sin\left(\frac{n\pi}{2}\right) \cos(k_P z') - \cos\left(\frac{n\pi}{2}\right) \sin(k_P z') \right) e^{-ikz' \cos \theta} dz' = \quad (\text{B.6})$$

$$= I_0 \mathbf{e}_z \frac{\mu_0}{4\pi} \frac{e^{ikr}}{r} \begin{cases} (-1)^{\frac{n-1}{2}} \int_{-\frac{n\pi}{2k_P}}^{\frac{n\pi}{2k_P}} \cos(k_P z') e^{-ikz' \cos \theta} dz' & \text{if } n \text{ odd} \\ (-1)^{\frac{n}{2}+1} \int_{-\frac{n\pi}{2k_P}}^{\frac{n\pi}{2k_P}} \sin(k_P z') e^{-ikz' \cos \theta} dz' & \text{if } n \text{ even} \end{cases} \quad (\text{B.7})$$

In the second line we used our knowledge that  $n$  is an integer value and separated the equation in one for even and one for odd  $n$ .

Now we can carry out the integration. The antiderivative can be found in the

standard literature (i.e. [151, p. 1082]):

$$\lim_{kr \rightarrow \infty} \mathbf{A}(\mathbf{x}) = I_0 \mathbf{e}_z \frac{\mu_0}{4\pi} \frac{e^{ikr}}{r} \begin{cases} \frac{2k_P \cos(\frac{k}{k_P} \frac{n\pi}{2} \cos \theta)}{k_P^2 - k^2 \cos^2 \theta} & \text{if } n \text{ odd} \\ -\frac{2ik_P \sin(\frac{k}{k_P} \frac{n\pi}{2} \cos \theta)}{k_P^2 - k^2 \cos^2 \theta} & \text{if } n \text{ even} \end{cases} \quad (\text{B.8})$$

The obtained vector potential is always parallel to the z-axis:  $\mathbf{A}(\mathbf{x}) = A(\mathbf{x})\mathbf{e}_z$ . The directionality of the far-field emission can be expressed easiest in spherical coordinates. We thus transfer  $\mathbf{e}_z$  from cartesian to spherical coordinates:  $\mathbf{e}_z = \cos \theta \mathbf{e}_r + \sin \theta \mathbf{e}_\theta$ .

Knowing the vector potential, it is easy to calculate the electrical and magnetic fields [113, eq. 9.4]:

$$\mathbf{H}(\mathbf{x}) = \frac{1}{\mu_0} \nabla \times \mathbf{A}(\mathbf{x}) = \quad (\text{B.9})$$

$$= \frac{\mathbf{e}_\phi}{\mu_0} \frac{1}{r} \left[ \frac{\partial}{\partial r} (A(\mathbf{x}) r \sin \theta) - \frac{\partial}{\partial \theta} (A(\mathbf{x}) \cos \theta) \right] \quad (\text{B.10})$$

The second summand,  $\frac{1}{r} \frac{\partial}{\partial \theta} (A(\mathbf{x}) \cos \theta)$ , is of the order  $r^{-2}$  and can neglected for  $r \rightarrow \infty$ . Carrying out the partial differentiation leads to:

$$\mathbf{H}(\mathbf{x}) \approx \frac{\mathbf{e}_\phi}{4\pi} I_0 k \frac{e^{ikr}}{r} \sin \theta \begin{cases} \frac{2ik_P \cos(\frac{k}{k_P} \frac{n\pi}{2} \cos \theta)}{k_P^2 - k^2 \cos^2 \theta} & \text{if } n \text{ odd} \\ \frac{2k_P \sin(\frac{k}{k_P} \frac{n\pi}{2} \cos \theta)}{k_P^2 - k^2 \cos^2 \theta} & \text{if } n \text{ even} \end{cases} \quad (\text{B.11})$$

The calculation of the electrical field is analogous [113, eq. 9.5]:

$$\mathbf{E}(\mathbf{x}) = \frac{i}{k} \sqrt{\frac{\mu_0}{\epsilon_0}} \nabla \times \mathbf{H}(\mathbf{x}) \quad (\text{B.12})$$

$$= \frac{i}{k} \sqrt{\frac{\mu_0}{\epsilon_0}} \left[ \mathbf{e}_r \frac{1}{r \sin \theta} \frac{\partial}{\partial \theta} (H(\mathbf{x}) \sin \theta) - \mathbf{e}_\theta \frac{1}{r} \frac{\partial}{\partial r} (H(\mathbf{x}) r) \right] \quad (\text{B.13})$$

---

As in the equation for the magnetic field, the first summand is of the order  $r^{-2}$  and can be neglected:

$$\mathbf{E}(\mathbf{x}) \approx \sqrt{\frac{\mu_0}{\epsilon_0}} \frac{\mathbf{e}_\theta}{4\pi} I_0 k \frac{e^{ikr}}{r} \sin \theta \begin{cases} \frac{2ik_P \cos(\frac{k}{k_P} \frac{n\pi}{2} \cos \theta)}{k_P^2 - k^2 \cos^2 \theta} & \text{if } n \text{ odd} \\ \frac{2k_P \sin(\frac{k}{k_P} \frac{n\pi}{2} \cos \theta)}{k_P^2 - k^2 \cos^2 \theta} & \text{if } n \text{ even} \end{cases} \quad (\text{B.14})$$

In antenna theory the emission patterns are often plotted as intensity plots. Therefore it is useful to calculate the time-averaged power radiated per unit solid angle [113, eq. 9.21]:

$$\frac{dP}{d\Omega} = \frac{1}{2} \text{Re} [r^2 \mathbf{n} \cdot \mathbf{E} \times \mathbf{H}^*] = \quad (\text{B.15})$$

$$= \frac{I_0^2}{8\pi^2} \sqrt{\frac{\mu_0}{\epsilon_0}} k^2 \sin^2 \theta \begin{cases} \left( \frac{k_P \cos(\frac{k}{k_P} \frac{n\pi}{2} \cos \theta)}{k_P^2 - k^2 \cos^2 \theta} \right)^2 & \text{if } n \text{ odd} \\ \left( \frac{k_P \sin(\frac{k}{k_P} \frac{n\pi}{2} \cos \theta)}{k_P^2 - k^2 \cos^2 \theta} \right)^2 & \text{if } n \text{ even} \end{cases} \quad (\text{B.16})$$

For the special case of a ordinary antenna ( $k_p = k$ ) the equation simplifies significantly and we obtain the formula of classical antenna theory [119, p. 160]:

$$\frac{dP}{d\Omega} = \frac{I_0^2}{8\pi^2} \sqrt{\frac{\mu_0}{\epsilon_0}} \begin{cases} \left( \frac{\cos(\frac{n\pi}{2} \cos \theta)}{\sin \theta} \right)^2 & \text{if } n \text{ odd} \\ \left( \frac{\sin(\frac{n\pi}{2} \cos \theta)}{\sin \theta} \right)^2 & \text{if } n \text{ even} \end{cases} \quad (\text{B.17})$$

Plotting the absolute value of the E-field (eq. B.14) to obtain the emission patterns is left to the interested reader. By changing the parameters it is possible to observed all the features described in section 4.4. As nice as this simplified model is, it is not able to explain is the off-resonance behavior of the wire antennas. For this, the effect of the wire as a Fabry-Pérot resonator is needed. This effect would have to be

artificially included into equation B.2 describing the current distribution. The model in chapter 4 does this automatically.

# Bibliography

- [1] F. GARDIOL, Y. FOURNIER: ‘Salvan: Cradle of wireless.’ *Microwave J.* **49** (2), pp. 124–136, 2006
- [2] H. HERTZ: ‘Ueber sehr schnelle electrische Schwingungen.’ *Ann. Phys.* **267** (7), pp. 421–448, 1887. doi:10.1002/andp.18872670707
- [3] H. YAGI: ‘Beam transmission of ultra short waves.’ *Proc. IRE* **16** (6), pp. 715–741, 1928
- [4] B. S. COLLINS: ‘VHF and UHF Antennas for Communications and Broadcasting.’ In: VOLAKIS [152]
- [5] C. A. BALANIS (editor): *Modern Antenna Handbook*. John Wiley & Sons, Inc., Hoboken, 2008
- [6] S. S. CHANG, C. SHIH, C. CHEN, W. LAI, C. R. C. WANG: ‘The shape transition of gold nanorods.’ *Langmuir* **15** (3), pp. 701–709, 1999. doi:10.1021/la980929l
- [7] O. SCHUBERT, J. BECKER, L. CARBONE, Y. KHALAVKA, T. PROVALSKA, I. ZINS, C. SÖNNICHSEN: ‘Mapping the polarization pattern of plasmon modes reveals nanoparticle symmetry.’ *Nano Lett.* **8** (8), pp. 2345–2350, 2008. doi:10.1021/nl801179a
- [8] D. FROMM, A. SUNDARAMURTHY, P. J. SCHUCK, G. KINO, W. MOERER: ‘Gap-dependent optical coupling of single ”Bowtie” nanoantennas resonant in the visible.’ *Nano Lett.* **4** (5), pp. 957–961, 2004. doi:10.1021/nl049951r
- [9] A. A. TSENG: ‘Recent developments in micromilling using focused ion beam technology.’ *J. Micromech. Microeng.* **14** (4), pp. R15–R34, 2004. doi:10.1088/0960-1317/14/4/R01
- [10] C. HAYNES, A. MCFARLAND, L. ZHAO, R. VAN DUYNE, G. C. SCHATZ, L. GUNNARSSON, J. PRIKULIS, B. KASEMO, M. KÄLL: ‘Nanoparticle optics: The importance of radiative dipole coupling in two-dimensional nanoparticle arrays.’ *J. Phys. Chem. B* **107** (30), pp. 7337–7342, 2003. doi:10.1021/jp034234r

- [11] C. FUMEAUX, M. GRITZ, I. CODREANU, W. SCHAICH, F. GONZALEZ, G. D. BOREMAN: ‘Measurement of the resonant lengths of infrared dipole antennas.’ *Infrared Phys. Techn.* **41** (5), pp. 271–281, 2000. doi:10.1016/S1350-4495(00)00047-5
- [12] P. MÜHLSCHLEGEL, H.-J. EISLER, O. J. F. MARTIN, B. HECHT, D. W. POHL: ‘Resonant optical antennas.’ *Science* **308** (5728), pp. 1607–1609, 2005. doi:10.1126/science.1111886
- [13] F. GONZALEZ, G. D. BOREMAN: ‘Comparison of dipole, bowtie, spiral and log-periodic IR antennas.’ *Infrared Phys. Techn.* **46** (5), pp. 418–428, 2005. doi:10.1016/j.infrared.2004.09.002
- [14] P. BHARADWAJ, B. DEUTSCH, L. NOVOTNY: ‘Optical Antennas.’ *Adv. Opt. Photon.* **1** (3), pp. 438–483, 2009. doi:10.1364/AOP.1.000438
- [15] M. I. STOCKMAN: ‘Nanofocusing of optical energy in tapered plasmonic waveguides.’ *Phys. Rev. Lett.* **93** (13), p. 137404, 2004. doi:10.1103/PhysRevLett.93.137404
- [16] C. ROPERS, C. C. NEACSU, T. ELSAESSER, M. ALBRECHT, M. B. RASCHKE, C. LIENAU: ‘Grating-coupling of surface plasmons onto metallic tips: A nanoconfined light source.’ *Nano Lett.* **7** (9), pp. 2784–2788, 2007. doi:10.1021/nl071340m
- [17] J.-J. GREFFET: ‘Nanoantennas for light emission.’ *Science* **308** (5728), pp. 1561–1563, 2005. doi:10.1126/science.1113355
- [18] T. A. KLAR: ‘Biosensing with plasmonic nanoparticles.’ In: V. M. SHALAEV, S. KAWATA (editors), ‘Nanophotonics with Surface Plasmons,’ *Advances in Nano-Optics and Nano-Photonics*, chap. 8, pp. 219–270. Elsevier, Amsterdam, 1st ed., 2007
- [19] J. AIZPURUA, G. W. BRYANT, L. RICHTER, F. J. GARCÍA DE ABAJO, B. KELLEY, T. MALLOUK: ‘Optical properties of coupled metallic nanorods for field-enhanced spectroscopy.’ *Phys. Rev. B* **71** (23), p. 235420, 2005. doi:10.1103/PhysRevB.71.235420
- [20] F. HAO, C. L. NEHL, J. H. HAFNER, P. NORDLANDER: ‘Plasmon resonances of a gold nanostar.’ *Nano Lett.* **7** (3), pp. 729–732, 2007. doi:10.1021/nl062969c
- [21] F. HAO, Y. SONNEFRAUD, P. VAN DORPE, S. A. MAIER, N. J. HALAS, P. NORDLANDER: ‘Symmetry Breaking in Plasmonic Nanocavities: Subradiant LSPR Sensing and a Tunable Fano Resonance.’ *Nano Lett.* **8** (11), pp. 3983–3988, 2008. doi:10.1021/nl802509r

- 
- [22] A. DMITRIEV, C. HAGGLUND, S. CHEN, H. FREDRIKSSON, T. PAKIZEH, M. KÄLL, D. S. SUTHERLAND: ‘Enhanced Nanoplasmonic Optical Sensors with Reduced Substrate Effect.’ *Nano Lett.* **8** (11), pp. 3893–3898, 2008. doi:10.1021/nl8023142
- [23] L. HIRSCH, R. STAFFORD, J. BANKSON, S. SERSHEN, B. RIVERA, R. PRICE, J. HAZLE, N. J. HALAS, J. L. WEST: ‘Nanoshell-mediated near-infrared thermal therapy of tumors under magnetic resonance guidance.’ *P. Natl. Acad. Sci. USA* **100** (23), pp. 13549–13554, 2003. doi:10.1073/pnas.2232479100
- [24] C. LOO, A. LOWERY, N. J. HALAS, J. L. WEST, R. A. DREZEK: ‘Immunotargeted nanoshells for integrated cancer imaging and therapy.’ *Nano Lett.* **5** (4), pp. 709–711, 2005. doi:10.1021/nl050127s
- [25] H. MAEDA, J. FANG, T. INUTSUKA, Y. KITAMOTO: ‘Vascular permeability enhancement in solid tumor: various factors, mechanisms involved and its implications.’ *Int. Immunopharmacol.* **3** (3), pp. 319–328, 2003. doi:10.1016/S1567-5769(02)00271-0
- [26] J. VALENTINE, S. ZHANG, T. ZENTGRAF, E. ULIN-AVILA, D. A. GENOV, G. BARTAL, X. ZHANG: ‘Three-dimensional optical metamaterial with a negative refractive index.’ *Nature* **455** (7211), pp. 376–U32, 2008. doi:10.1038/nature07247
- [27] D. SCHURIG, J. J. MOCK, B. J. JUSTICE, S. A. CUMMER, J. B. PENDRY, A. F. STARR, D. R. SMITH: ‘Metamaterial electromagnetic cloak at microwave frequencies.’ *Science* **314** (5801), pp. 977–980, 2006. doi:10.1126/science.1133628
- [28] A. CHO: ‘PHYSICS Invisibility Umbrella Would Let Future Harry Potters See the Light.’ *Science* **323** (5915), pp. 701–701, 2009. doi:10.1126/science.323.5915.701a
- [29] J. K. ROWLING: *Harry Potter and the Philosopher’s Stone*. Bloomsbury, London, 1997
- [30] P. B. JOHNSON, R. W. CHRISTY: ‘Optical-Constants of Noble-Metals.’ *Phys. Rev. B* **6** (12), pp. 4370–4379, 1972. doi:10.1103/PhysRevB.6.4370
- [31] E. D. PALIK (editor): *Handbook of Optical Constants of Solids*. Academic Press, Orlando, 1985
- [32] R. H. RITCHIE: ‘Plasma Losses by Fast Electrons in Thin Films.’ *Phys. Rev.* **106** (5), pp. 874–881, 1957. doi:10.1103/PhysRev.106.874

- [33] E. N. ECONOMOU: ‘Surface Plasmons in Thin Films.’ *Phys. Rev.* **182** (2), pp. 539–554, 1969. doi:10.1103/PhysRev.182.539
- [34] J. ASHLEY, L. EMERSON: ‘Dispersion relations for non-radiative surface plasmons on cylinders.’ *Surf. Sci.* **41** (2), pp. 615–618, 1974. doi:10.1016/0039-6028(74)90080-6
- [35] K. S. YEE: ‘Numerical solution of initial boundary value problems involving maxwell’s equations in isotropic media.’ *IEEE T. Antenn. Propag.* **AP14** (3), pp. 302–307, 1966. doi:10.1109/TAP.1966.1138693
- [36] T. H. TAMINIAU, F. D. STEFANI, F. B. SEGERINK, N. F. VAN HULST: ‘Optical antennas direct single-molecule emission.’ *Nat. Photonics* **2** (4), pp. 234–237, 2008. doi:10.1038/nphoton.2008.32
- [37] P. BIAGIONI, M. SAVOINI, J.-S. HUANG, L. DUÒ, M. FINAZZI, B. HECHT: ‘Near-field polarization shaping by a near-resonant plasmonic cross antenna.’ *Phys. Rev. B* **80** (15), p. 153409, 2009. doi:10.1103/PhysRevB.80.153409
- [38] T. J. DAVIS, K. C. VERNON, D. E. GÓMEZ: ‘Effect of retardation on localized surface plasmon resonances in a metallic nanorod.’ *Opt. Express* **17** (26), pp. 23655–23663, 2009. doi:10.1364/OE.17.023655
- [39] S. W. PRESCOTT, P. MULVANEY: ‘Gold nanorod extinction spectra.’ *J. Appl. Phys.* **99** (12), p. 123504, 2006. doi:10.1063/1.2203212
- [40] N. FÉLIDJ, J. AUBARD, G. LÉVI: ‘Discrete dipole approximation for ultraviolet-visible extinction spectra simulation of silver and gold colloids.’ *J. Chem. Phys.* **111** (3), pp. 1195–1208, 1999. doi:10.1063/1.479305
- [41] W. DOYLE, A. AGARWAL: ‘Optical Extinction of Metal Spheres.’ *J. Opt. Soc. Am.* **55** (3), pp. 305–308, 1965. doi:10.1364/JOSA.55.000305
- [42] F. J. GARCÍA DE ABAJO: ‘Nonlocal Effects in the Plasmons of Strongly Interacting Nanoparticles, Dimers, and Waveguides.’ *J. Phys. Chem. C* **112** (46), pp. 17983–17987, 2008. doi:10.1021/jp807345h
- [43] J. R. KRENN, G. SCHIDER, W. RECHBERGER, B. LAMPRECHT, A. LEITNER, F. R. AUSSNEG, J.-C. WEEBER: ‘Design of multipolar plasmon excitations in silver nanoparticles.’ *Appl. Phys. Lett.* **77** (21), pp. 3379–3381, 2000. doi:10.1063/1.1327615
- [44] L. ZHAO, K. KELLY, G. C. SCHATZ: ‘The extinction spectra of silver nanoparticle arrays: Influence of array structure on plasmon resonance wavelength and width.’ *J. Phys. Chem. B* **107** (30), pp. 7343–7350, 2003. doi:10.1021/jp034235j

- 
- [45] C. UNGUREANU, R. G. RAYAVARAPU, S. MANOHAR, T. G. VAN LEEUWEN: ‘Discrete dipole approximation simulations of gold nanorod optical properties: Choice of input parameters and comparison with experiment.’ *J. Appl. Phys.* **105** (10), p. 102032, 2009. doi:10.1063/1.3116139
- [46] H. DITLBACHER, A. HOHENAU, D. WAGNER, U. KREIBIG, M. ROGERS, F. HOFER, F. R. AUSSENEKG, J. R. KRENN: ‘Silver nanowires as surface plasmon resonators.’ *Phys. Rev. Lett.* **95** (25), p. 257403, 2005. doi:10.1103/PhysRevLett.95.257403
- [47] P. GHENUCHE, S. CHERUKULAPPURATH, T. H. TAMINIAU, N. F. VAN HULST, R. QUIDANT: ‘Spectroscopic mode mapping of resonant plasmon nanoantennas.’ *Phys. Rev. Lett.* **101** (11), p. 116805, 2008. doi:10.1103/PhysRevLett.101.116805
- [48] E. ABBE: ‘Beiträge zur Theorie des Mikroskops und der mikroskopischen Wahrnehmung.’ *Arch. Mikros. Anat.* **9** (1), pp. 413–468, 1873. doi:10.1007/BF02956173
- [49] J. NELAYAH, M. KOCIAK, O. STEPHAN, F. J. GARCÍA DE ABAJO, M. TENCE, L. HENRARD, D. TAVERNA, I. PASTORIZA-SANTOS, L. M. LIZ-MARZÁN, C. COLLIEX: ‘Mapping surface plasmons on a single metallic nanoparticle.’ *Nat. Phys.* **3** (5), pp. 348–353, 2007. doi:10.1038/nphys575
- [50] M. BOSMAN, V. J. KEAST, M. WATANABE, A. I. MAAROOF, M. B. CORTIE: ‘Mapping surface plasmons at the nanometre scale with an electron beam.’ *Nanotechnology* **18** (16), p. 165505, 2007. doi:10.1088/0957-4484/18/16/165505
- [51] F. J. GARCÍA DE ABAJO, M. KOCIAK: ‘Probing the photonic local density of states with electron energy loss spectroscopy.’ *Phys. Rev. Lett.* **100** (10), p. 106804, 2008. doi:10.1103/PhysRevLett.100.106804
- [52] G. COLAS DES FRANCS, C. GIRARD, J.-C. WEEBER, A. DEREUX: ‘Relationship between scanning near-field optical images and local density of photonic states.’ *Chem. Phys. Lett.* **345** (5-6), pp. 512–516, 2001. doi:10.1016/S0009-2614(01)00914-9
- [53] U. HOHENESTER, H. DITLBACHER, J. R. KRENN: ‘Electron-Energy-Loss Spectra of Plasmonic Nanoparticles.’ *Phys. Rev. Lett.* **103** (10), p. 106801, 2009. doi:10.1103/PhysRevLett.103.106801
- [54] M. AESCHLIMANN, M. BAUER, D. BAYER, T. BRIXNER, F. J. GARCÍA DE ABAJO, W. PFEIFFER, M. ROHMER, C. SPINDLER, F. STEEB: ‘Adaptive

- subwavelength control of nano-optical fields.’ *Nature* **446** (7133), pp. 301–304, 2007. doi:10.1038/nature05595
- [55] L. DOUILLARD, F. CHARRA, Z. KORCZAK, R. BACHELOT, S. KOSTCHEEV, G. LERONDEL, P.-M. ADAM, P. ROYER: ‘Short range plasmon resonators probed by photoemission electron microscopy.’ *Nano Lett.* **8** (3), pp. 935–940, 2008. doi:10.1021/nl080053v
- [56] A. KUBO, K. ONDA, H. PETEK, Z. SUN, Y. JUNG, H. K. KIM: ‘Femtosecond imaging of surface plasmon dynamics in a nanostructured silver film.’ *Nano Lett.* **5** (6), pp. 1123–1127, 2005. doi:10.1021/nl0506655
- [57] D. BAYER, C. WIEMANN, O. GAIER, M. BAUER, M. AESCHLIMANN: ‘Time-Resolved 2PPE and Time-Resolved PEEM as a Probe of LSP’s in Silver Nanoparticles.’ *J. Nanomater.* **2008** (249514), pp. 1–11, 2008. doi:10.1155/2008/249514
- [58] E. H. SYNGE: ‘A suggested method for extending microscopic resolution into the ultra-microscopic region.’ *Philos. Mag.* **6** (35), pp. 356–362, 1928
- [59] D. W. POHL, W. DENK, M. LANZ: ‘Optical stethoscopy: Image recording with resolution  $\lambda/20$ .’ *Appl. Phys. Lett.* **44** (7), pp. 651–653, 1984. doi:10.1063/1.94865
- [60] E. BETZIG, J. K. TRAUTMAN: ‘Near-Field Optics: Microscopy, Spectroscopy, and Surface Modification Beyond the Diffraction Limit.’ *Science* **257** (5067), pp. 189–195, 1992. doi:10.1126/science.257.5067.189
- [61] B. HECHT, B. SICK, U. P. WILD, V. DECKERT, R. ZENOBI, O. J. F. MARTIN, D. W. POHL: ‘Scanning near-field optical microscopy with aperture probes: Fundamentals and applications.’ *J. Chem. Phys.* **112** (18), pp. 7761–7774, 2000. doi:10.1063/1.481382
- [62] D. MCMULLAN: ‘The prehistory of scanned image microscopy. Part I: Scanned optical microscopes.’ *Proceedings of the Royal Microscopical Society* **25** (2), pp. 127–131, 1990
- [63] L. NOVOTNY: ‘Chapter 5 The history of near-field optics.’ In: E. WOLF (editor), ‘Progress in Optics,’ vol. 50 of *Progress in Optics*, pp. 137–184. Elsevier, Amsterdam, 2007. doi:10.1016/S0079-6638(07)50005-3
- [64] F. ZENHAUSERN, M. P. O’BOYLE, H. K. WICKRAMASINGHE: ‘Apertureless Near-Field Optical Microscope.’ *Appl. Phys. Lett.* **65** (13), pp. 1623–1625, 1994. doi:10.1063/1.112931

- 
- [65] B. KNOLL: *Abtastende Nahfeldmikroskopie mit Infrarot- und Mikrowellen*. Ph.D. thesis, Technische Universität München, 1999
- [66] M. BREHM, H. G. FREY, R. GUCKENBERGER, R. HILLENBRAND, D. KAZANTSEV, F. KEILMANN, N. OCELIC, T. TAUBNER: ‘Consolidating apertureless SNOM.’ *J. Korean Phys. Soc.* **47**, pp. S80–S85, 2005
- [67] T. KLAR, M. PERNER, S. GROSSE, G. VON PLESSEN, W. SPIRKL, J. FELDMANN: ‘Surface-plasmon resonances in single metallic nanoparticles.’ *Phys. Rev. Lett.* **80** (19), pp. 4249–4252, 1998. doi:10.1103/PhysRevLett.80.4249
- [68] K. IMURA, T. NAGAHARA, H. OKAMOTO: ‘Near-field optical imaging of plasmon modes in gold nanorods.’ *J. Chem. Phys.* **122** (15), p. 154701, 2005. doi:10.1063/1.1873692
- [69] H. OKAMOTO, K. IMURA: ‘Near-field optical imaging of nanoscale optical fields and plasmon waves.’ *Japanese Journal of Applied Physics* **47** (7), pp. 6055–6062, 2008. doi:10.1143/JJAP.47.6055
- [70] R. HILLENBRAND, F. KEILMANN, P. HANARP, D. S. SUTHERLAND, J. AIZPURUA: ‘Coherent imaging of nanoscale plasmon patterns with a carbon nanotube optical probe.’ *Appl. Phys. Lett.* **83** (2), pp. 368–370, 2003. doi:10.1063/1.1592629
- [71] R. ESTEBAN, R. VOGELGESANG, J. DORFMÜLLER, A. DMITRIEV, C. ROCKSTUHL, C. ETRICH, K. KERN: ‘Direct Near-Field Optical Imaging of Higher Order Plasmonic Resonances.’ *Nano Lett.* **8** (10), pp. 3155–3159, 2008. doi:10.1021/nl801396r
- [72] A. C. JONES, R. L. OLMON, S. E. SKRABALAK, B. J. WILEY, Y. N. XIA, M. B. RASCHKE: ‘Mid-IR Plasmonics: Near-Field Imaging of Coherent Plasmon Modes of Silver Nanowires.’ *Nano Lett.* **9** (7), pp. 2553–2558, 2009. doi:10.1021/nl900638p
- [73] D.-S. KIM, J. HEO, S.-H. AHN, S. W. HAN, W. S. YUN, Z. H. KIM: ‘Real-Space Mapping of the Strongly Coupled Plasmons of Nanoparticle Dimers.’ *Nano Lett.* **9** (10), pp. 3619–3625, 2009. doi:10.1021/nl901839f
- [74] L. NOVOTNY, R. BIAN, X. XIE: ‘Theory of nanometric optical tweezers.’ *Phys. Rev. Lett.* **79** (4), pp. 645–648, 1997. doi:10.1103/PhysRevLett.79.645
- [75] R. ESTEBAN LLORENTE: *Apertureless SNOM: Realistic Modeling of the Imaging Process and Measurements of Resonant Plasmonic Nanostructures*. Ph.D. thesis, École Polytechnique Fédérale de Lausanne, 2007

- [76] F. H'DHILI, R. BACHELOT, G. LERONDEL, D. BARCHIESI, P. ROYER: 'Near-field optics: Direct observation of the field enhancement below an apertureless probe using a photosensitive polymer.' *Appl. Phys. Lett.* **79** (24), pp. 4019–4021, 2001. doi:10.1063/1.1425083
- [77] R. BACHELOT, F. H'DHILI, D. BARCHIESI, G. LERONDEL, R. FIKRI, P. ROYER, N. LANDRAUD, J. PERETTI, F. CHAPUT, G. LARNPEL, J. BOILOT, K. LAHLIL: 'Apertureless near-field optical microscopy: A study of the local tip field enhancement using photosensitive azobenzene-containing films.' *J. Appl. Phys.* **94** (3), pp. 2060–2072, 2003. doi:10.1063/1.1585117
- [78] R. ESTEBAN, R. VOGELGESANG, K. KERN: 'Simulation of optical near and far fields of dielectric apertureless scanning probes.' *Nanotechnology* **17** (2), pp. 475–482, 2006. doi:10.1088/0957-4484/17/2/022
- [79] J. M. GERTON, L. WADE, G. LESSARD, Z. MA, S. QUAKE: 'Tip-enhanced fluorescence microscopy at 10 nanometer resolution.' *Phys. Rev. Lett.* **93** (18), p. 180801, 2004. doi:10.1103/PhysRevLett.93.180801
- [80] A. BEK, R. VOGELGESANG, K. KERN: 'Apertureless scanning near field optical microscope with sub-10 nm resolution.' *Rev. Sci. Instrum.* **77** (4), p. 043703, 2006. doi:10.1063/1.2190211
- [81] R. HILLENBRAND, F. KEILMANN: 'Complex optical constants on a subwavelength scale.' *Phys. Rev. Lett.* **85** (14), pp. 3029–3032, 2000. doi:10.1103/PhysRevLett.85.3029
- [82] B. KNOLL, F. KEILMANN: 'Enhanced dielectric contrast in scattering-type scanning near-field optical microscopy.' *Opt. Commun.* **182** (4-6), pp. 321–328, 2000. doi:10.1016/S0030-4018(00)00826-9
- [83] R. HILLENBRAND: *Nahfeldoptische Amplituden- und Phasenkontrast-mikroskopie zur nanoskopischen optischen Abbildung von Materialkontrast und optisch resonanten Partikeln*. Ph.D. thesis, Technische Universität München, 2001
- [84] J. DORFMÜLLER: *Implementation of an Apertureless Scanning Near-Field Optical Microscope for the Infrared Spectrum*. Diplomarbeit, University of Konstanz, Konstanz, Germany, 2006
- [85] T. TAUBNER, R. HILLENBRAND, F. KEILMANN: 'Performance of visible and mid-infrared scattering-type near-field optical microscopes.' *J. Microsc.-Oxf.* **210**, pp. 311–314, 2003. doi:10.1046/j.1365-2818.2003.01164.x

- 
- [86] D. J. SCHROEDER: *Astronomical Optics*. Academic Press, San Diego, 2nd ed., 2000
- [87] R. LOUDON: *The Quantum Theory of Light*. Oxford University Press, Oxford, New York, 3rd ed., 2000
- [88] B. DEUTSCH, R. HILLENBRAND, L. NOVOTNY: ‘Near-field amplitude and phase recovery using phase-shifting interferometry.’ *Opt. Express* **16** (2), pp. 494–501, 2008. doi:10.1364/OE.16.000494
- [89] N. OCELCIC, A. J. HUBER, R. HILLENBRAND: ‘Pseudoheterodyne detection for background-free near-field spectroscopy.’ *Appl. Phys. Lett.* **89** (10), p. 101124, 2006. doi:10.1063/1.2348781
- [90] E. POTMA, W. DE BOEIJ, D. WIERSMA: ‘Femtosecond dynamics of intracellular water probed with nonlinear optical Kerr effect microspectroscopy.’ *Biophys. J.* **80** (6), pp. 3019–3024, 2001
- [91] L. GOMEZ, R. BACHELOT, A. BOUHELIER, G. P. WIEDERRECHT, S.-H. CHANG, S. GRAY, F. HUA, S. JEON, J. ROGERS, M. CASTRO, S. BLAIZE, I. STEFANON, G. LERONDEL, P. ROYER: ‘Apertureless scanning near-field optical microscopy: a comparison between homodyne and heterodyne approaches.’ *J. Opt. Soc. Am. B* **23** (5), pp. 823–833, 2006. doi:10.1364/JOSAB.23.000823
- [92] Y. OSHIKANE, S. HARA, T. MATSUDA, H. INOUE, M. NAKANO, T. KATAOKA: ‘Observation of localized optical near-field generated by submicron two-hole structure for novel SNOM probe.’ *Surf. Interface Anal.* **40** (6-7), pp. 1054–1058, 2008. doi:10.1002/sia.2830
- [93] A. GARCÍA-ETXARRI, I. ROMERO, F. J. GARCÍA DE ABAJO, R. HILLENBRAND, J. AIZPURUA: ‘Influence of the tip in near-field imaging of nanoparticle plasmonic modes: Weak and strong coupling regimes.’ *Phys. Rev. B* **79** (12), p. 125439, 2009. doi:10.1103/PhysRevB.79.125439
- [94] T. ZENTGRAF, J. DORFMÜLLER, C. ROCKSTUHL, C. ETRICH, R. VOGELGESANG, K. KERN, T. PERTSCH, F. LEDERER, H. GIESSEN: ‘Amplitude-and phase-resolved optical near fields of split-ring-resonator-based metamaterials.’ *Opt. Lett.* **33** (8), pp. 848–850, 2008. doi:10.1364/OL.33.000848
- [95] J. DORFMÜLLER, R. VOGELGESANG, R. T. WEITZ, C. ROCKSTUHL, C. ETRICH, T. PERTSCH, F. LEDERER, K. KERN: ‘Fabry-Pérot Resonances in One-Dimensional Plasmonic Nanostructures.’ *Nano Lett.* **9** (6), pp. 2372–2377, 2009. doi:10.1021/nl900900r

- [96] M. RANG, A. C. JONES, F. ZHOU, Z.-Y. LI, B. J. WILEY, Y. N. XIA, M. B. RASCHKE: ‘Optical Near-Field Mapping of Plasmonic Nanoprisms.’ *Nano Lett.* **8** (10), pp. 3357–3363, 2008. doi:10.1021/nl801808b
- [97] E. PRODAN, C. RADLOFF, N. J. HALAS, P. NORDLANDER: ‘A hybridization model for the plasmon response of complex nanostructures.’ *Science* **302** (5644), pp. 419–422, 2003. doi:10.1126/science.1089171
- [98] N. VERELLEN, Y. SONNEFRAUD, H. SOBHANI, F. HAO, V. V. MOSHCHALOV, P. VAN DORPE, P. NORDLANDER, S. A. MAIER: ‘Fano Resonances in Individual Coherent Plasmonic Nanocavities.’ *Nano Lett.* **9** (4), pp. 1663–1667, 2009. doi:10.1021/nl9001876
- [99] N. LIU, T. WEISS, M. MESCH, L. LANGGUTH, U. EIGENTHALER, M. HIRSCHER, C. SOENNICHSEN, H. GIESSEN: ‘Planar Metamaterial Analogue of Electromagnetically Induced Transparency for Plasmonic Sensing.’ *Nano Lett.* **10** (4), pp. 1103–1107, 2010. doi:10.1021/nl902621d
- [100] C. ALZAR, M. MARTINEZ, P. NUSSENZVEIG: ‘Classical analog of electromagnetically induced transparency.’ *Am. J. Phys.* **70** (1), pp. 37–41, 2002. doi:10.1119/1.1412644
- [101] R. VOGELGESANG, J. DORFMÜLLER, R. ESTEBAN, R. T. WEITZ, A. DMITRIEV, K. KERN: ‘Plasmonic nanostructures in aperture-less scanning near-field optical microscopy (aSNOM).’ *Phys. Status Solidi B* **245** (10), pp. 2255–2260, 2008. doi:10.1002/pssb.200879617
- [102] A. BEK: *Apertureless SNOM: A New Tool for Nano-Optics*. Ph.D. thesis, École Polytechnique Fédérale de Lausanne, 2004
- [103] L. NOVOTNY, B. HECHT: *Principles of Nano-Optics*. Cambridge University Press, Cambridge, 2006
- [104] L. NOVOTNY: ‘Effective wavelength scaling for optical antennas.’ *Phys. Rev. Lett.* **98** (26), p. 266802, 2007. doi:10.1103/PhysRevLett.98.266802
- [105] E. S. BARNARD, J. S. WHITE, A. CHANDRAN, M. L. BRONGERSMA: ‘Spectral properties of plasmonic resonator antennas.’ *Opt. Express* **16** (21), pp. 16529–16537, 2008. doi:10.1364/OE.16.016529
- [106] G. W. BRYANT, F. J. GARCÍA DE ABAJO, J. AIZPURUA: ‘Mapping the plasmon resonances of metallic nanoantennas.’ *Nano Lett.* **8** (2), pp. 631–636, 2008. doi:10.1021/nl073042v

- 
- [107] E. R. ENCINA, E. A. CORONADO: ‘Plasmonic nanoantennas: Angular scattering properties of multipole resonances in noble metal nanorods.’ *J. Phys. Chem. C* **112** (26), pp. 9586–9594, 2008. doi:10.1021/jp7120142
- [108] G. SCHIDER, J. R. KRENN, A. HOHENAU, H. DITLBACHER, A. LEITNER, F. R. AUSSENEGG, W. SCHAICH, I. PUSCASU, B. MONACELLI, G. D. BOREMAN: ‘Plasmon dispersion relation of Au and Ag nanowires.’ *Phys. Rev. B* **68** (15), p. 155427, 2003. doi:10.1103/PhysRevB.68.155427
- [109] J. J. HANAK: ‘The “multiple-sample concept” in materials research: Synthesis, compositional analysis and testing of entire multicomponent systems.’ *J. Mater. Sci.* **5** (11), pp. 964–971, 1970. doi:10.1007/BF00558177
- [110] A. TAFLOVE, S. C. HAGNESS: *Computational Electrodynamics: The Finite-Difference Time-Domain Method*. Artech House, Boston, 3rd ed., 2005
- [111] T. SØNDERGAARD, J. BEERMANN, A. BOLTASSEVA, S. I. BOZHEVOLNYI: ‘Slow-plasmon resonant-nanostrip antennas: Analysis and demonstration.’ *Phys. Rev. B* **77** (11), p. 115420, 2008. doi:10.1103/PhysRevB.77.115420
- [112] R. GORDON: ‘Reflection of Cylindrical Surface Waves.’ *Opt. Express* **17** (21), pp. 18621–18629, 2009. doi:10.1364/OE.17.018621
- [113] J. D. JACKSON: *Classical Electrodynamics*. Wiley, New York, Weinheim, 3rd ed., 1999
- [114] S. J. ORFANIDIS: *Electromagnetic Waves and Antennas*. ECE Department, Rutgers University, Piscataway (NJ), 2008
- [115] R. QIANG, R. L. CHEN, J. CHEN: ‘Modeling electrical properties of gold films at infrared frequency using FDTD method.’ *Int. J. Infrared Milli.* **25** (8), pp. 1263–1270, 2004. doi:10.1023/B:IJIM.0000042759.67055.7a
- [116] C. F. BOHREN, D. R. HUFFMAN: *Absorption and Scattering of Light by Small Particles*. Wiley-VCH, Weinheim, 1998
- [117] H. POCKLINGTON: ‘Electrical oscillations in wires.’ *Proc. Camb. Phil. Soc.* **9**, pp. 461–461, 1897
- [118] G. MIE: ‘Beiträge zur Optik trüber Medien, speziell kolloidaler Metallösungen.’ *Ann. Phys.* **25** (3), pp. 377–445, 1908. doi:10.1002/andp.19083300302
- [119] D. S. JONES: *The Theory of Electromagnetism*, vol. 47 of *International Series of Monographs on Pure and Applied Mathematics*. Pergamon Press, Oxford, New York, 1964

- [120] E. HALLÉN: ‘Properties of a Long Antenna.’ *J. Appl. Phys.* **19** (12), pp. 1140–1147, 1948. doi:10.1063/1.1715034
- [121] T. F. EIBERT, J. L. VOLAKIS: ‘Fundamentals of Antennas, Arrays, and Mobile Communications.’ In: VOLAKIS [152], chap. 1
- [122] C. A. PFEIFFER, E. N. ECONOMOU, K. L. NGAI: ‘Surface polaritons in a circularly cylindrical interface: Surface plasmons.’ *Phys. Rev. B* **10** (8), pp. 3038–3051, 1974. doi:10.1103/PhysRevB.10.3038
- [123] J. R. CARSON: ‘A generalization of the reciprocal theorem.’ *Bell. Syst. Tech. J.* **3** (3), pp. 393–399, 1924
- [124] A. V. AKIMOV, A. MUKHERJEE, C. L. YU, D. E. CHANG, A. S. ZIBROV, P. R. HEMMER, H. PARK, M. D. LUKIN: ‘Generation of single optical plasmons in metallic nanowires coupled to quantum dots.’ *Nature* **450** (7168), pp. 402–406, 2007. doi:10.1038/nature06230
- [125] F. J. ZUCKER: ‘Surface-Wave Antennas.’ In: VOLAKIS [152], chap. 10
- [126] E. HECHT: *Optics*. Addison-Wesley, San Francisco, 4th ed., 2002
- [127] M. MÄDER, T. HÖCHE, J. W. GERLACH, S. PERLT, J. DORFMÜLLER, M. SALIBA, R. VOGELGESANG, K. KERN, B. RAUSCHENBACH: ‘Plasmonic Activity of Large-Area Gold Nanodot Arrays on Arbitrary Substrates.’ *Nano Lett.* **10** (1), pp. 47–51, 2010. doi:10.1021/nl903633z
- [128] Z. LI, F. HAO, Y. HUANG, Y. FANG, P. NORDLANDER, H. XU: ‘Directional Light Emission from Propagating Surface Plasmons of Silver Nanowires.’ *Nano Lett.* **9** (12), pp. 4383–4386, 2009. doi:10.1021/nl902651e
- [129] J. G. VAN BLADEL: *Electromagnetic Fields*. IEEE/Wiley-Interscience, Hoboken, 2nd ed., 2007
- [130] W. DEMTRÖDER: *Experimentalphysik*, vol. 1: Mechanik und Wärme. Springer-Verlag, Berlin, Heidelberg, New York, 5th ed., 2008. doi:10.1007/978-3-540-79295-6
- [131] D. MESCHEDE: *Gerthsen Physik*. Springer-Verlag, Berlin, Heidelberg, New York, 23rd ed., 2006
- [132] C. WIESMANN, K. BERGENEK, N. LINDER, U. T. SCHWARZ: ‘Photonic crystal LEDs - designing light extraction.’ *Laser Photonics Rev.* **3** (3), pp. 262–286, 2009. doi:10.1002/lpor.200810053

- 
- [133] V. E. FERRY, L. A. SWEATLOCK, D. PACIFICI, H. A. ATWATER: ‘Plasmonic Nanostructure Design for Efficient Light Coupling into Solar Cells.’ *Nano Lett.* **8** (12), pp. 4391–4397, 2008. doi:10.1021/nl8022548
- [134] N. LIU, H. GUO, L. FU, S. KAISER, H. SCHWEIZER, H. GIESSEN: ‘Three-dimensional photonic metamaterials at optical frequencies.’ *Nat. Mater.* **7** (1), pp. 31–37, 2008. doi:10.1038/nmat2072
- [135] N. LIU, H. LIU, S. ZHU, H. GIESSEN: ‘Stereometamaterials.’ *Nat. Photonics* **3** (3), pp. 157–162, 2009. doi:10.1038/NPHOTON.2009.4
- [136] R. W. BOYD: *Nonlinear Optics*. Academic Press, San Diego, 2nd ed., 2003
- [137] J. PETSCHULAT, A. CHIPOULINE, E. PSHENAY-SEVERIN, A. TÜNNERMANN, T. PERTSCH, C. MENZEL, C. ROCKSTUHL, T. PAUL, F. LEDERER: ‘Analytical Modelling of Linear and Nonlinear Properties of Metamaterials Based on Multipole Expansion.’ *Proc. of SPIE* **7353** (73530D), pp. 1–13, 2009. doi:10.1117/12.821859
- [138] M. PELTON, J. AIZPURUA, G. W. BRYANT: ‘Metal-nanoparticle plasmonics.’ *Laser Photonics Rev.* **2** (3), pp. 136–159, 2008. doi:10.1002/lpor.200810003
- [139] S. PALOMBA, M. DANCKWERTS, L. NOVOTNY: ‘Nonlinear plasmonics with gold nanoparticle antennas.’ *J. Opt. A: Pure Appl. Opt.* **11** (11), p. 114030, 2009. doi:10.1088/1464-4258/11/11/114030
- [140] O. SCHWARTZ, D. ORON: ‘Background-Free Third Harmonic Imaging of Gold Nanorods.’ *Nano Lett.* **9** (12), pp. 4093–4097, 2009. doi:10.1021/nl902305w
- [141] S. A. MAIER: *Plasmonics*. Springer, New York, 2007
- [142] C. DIEDERICHs, J. TIGNON, G. DASBACH, C. CIUTI, A. LEMAITRE, J. BLOCH, P. ROUSSIGNOL, C. DELALANDE: ‘Parametric oscillation in vertical triple microcavities.’ *Nature* **440** (7086), pp. 904–907, 2006. doi:10.1038/nature04602
- [143] M. LIPPITZ, M. A. VAN DIJK, M. ORRIT: ‘Third-harmonic generation from single gold nanoparticles.’ *Nano Lett.* **5** (4), pp. 799–802, 2005. doi:10.1021/nl0502571
- [144] J. RINGER, R. QUIDANT, N. F. VAN HULST, S. PALOMBA, L. NOVOTNY: ‘Free-Space Excitation of Propagating Surface Plasmon Polaritons by Nonlinear Four-Wave Mixing.’ *Phys. Rev. Lett.* **103** (266802), pp. 1–4, 2009. doi:10.1103/PhysRevLett.103.266802

- [145] J. B. PENDRY, A. J. HOLDEN, D. J. ROBBINS, W. J. STEWART: ‘Magnetism from conductors and enhanced nonlinear phenomena.’ *IEEE Trans. Microw. Theory* **47** (11), pp. 2075–2084, 1999. doi:10.1109/22.798002
- [146] T. H. TAMINIAU, F. D. STEFANI, N. F. VAN HULST: ‘Enhanced directional excitation and emission of single emitters by a nano-optical Yagi-Uda antenna.’ *Opt. Express* **16** (14), pp. 10858–10866, 2008. doi:10.1364/OE.16.010858
- [147] J.-S. HUANG, T. FEICHTNER, P. BIAGIONI, B. HECHT: ‘Impedance Matching and Emission Properties of Nanoantennas in an Optical Nanocircuit.’ *Nano Lett.* **9** (5), pp. 1897–1902, 2009. doi:10.1021/nl803902t
- [148] N. A. MIRIN, K. BAO, P. NORDLANDER: ‘Fano Resonances in Plasmonic Nanoparticle Aggregates.’ *J. Phys. Chem. A* **113** (16), pp. 4028–4034, 2009. doi:10.1021/jp810411q
- [149] G. DELLA VALLE, T. SONDERGAARD, S. I. BOZHEVOLNYI: ‘High-Q plasmonic resonators based on metal split nanocylinders.’ *Phys. Rev. B* **80** (23), p. 235405, 2009. doi:10.1103/PhysRevB.80.235405
- [150] R. MERLIN: ‘Metamaterials and the Landau-Lifshitz permeability argument: Large permittivity begets high-frequency magnetism.’ *P. Natl. Acad. Sci. USA* **106** (6), pp. 1693–1698, 2009. doi:10.1073/pnas.0808478106
- [151] I. N. BRONSTEIN, K. A. SEMENDJAJEW, G. MUSIOL, H. MÜHLIG: *Taschenbuch der Mathematik*. Verlag Harri Deutsch, Frankfurt am Main, 6th ed., 2005
- [152] J. L. VOLAKIS (editor): *Antenna Engineering Handbook*. McGraw-Hill, New York, 2007

# Curriculum Vitae

## Name

Name	Jens Dorf Müller
Date of Birth	March 26, 1978
Place of Birth	Damme, Niedersachsen, Germany
Nationality	German

## School Education

1984-1988	Primary School, Damme, Germany
1988-1993	Franz-Marc-Gymnasium, Markt Schwaben, Germany
1993-1997	Hanns-Seidel-Gymnasium, Hösbach, Germany

## Military Service

1997-1998	Stab Technische Gruppe, Lufttransportgeschwader 61, Penzing, Germany
-----------	--

## University Education

1998-2006	Studies of Physics at the University of Konstanz, Germany
2002	Exchange Student at the University of Adelaide, Australia Stipend from the “Landesprogramm Baden-Württemberg”

## Professional Experience

2005-2006	Diploma Thesis in the Group of Prof. Kern at the Max Planck Institute for Solid State Research, Stuttgart, Germany Title: “Implementation of an Apertureless Scanning Near-Field Optical Microscope for the Infrared Spectrum”
2006-2010	PhD Student in the Group of Prof. Kern at the Max Planck Institute for Solid State Research, Stuttgart, Germany Topic: “Microscopy and spectroscopy of nm sized resonant structures at visible to mid-infrared wavelengths”



# Publications

- [1] E. J. H. LEE, K. BALASUBRAMANIAN, J. DORFMÜLLER, R. VOGELGESANG, N. FU, A. MEWS, M. BURGHARD, K. KERN: ‘Electronic-band-structure mapping of nanotube transistors by scanning photocurrent microscopy.’ *Small* **3** (12), pp. 2038–2042, 2007. doi:10.1002/sml.200700418
- [2] R. ESTEBAN, R. VOGELGESANG, J. DORFMÜLLER, A. DMITRIEV, C. ROCKSTUHL, C. ETRICH, K. KERN: ‘Direct Near-Field Optical Imaging of Higher Order Plasmonic Resonances.’ *Nano Lett.* **8** (10), pp. 3155–3159, 2008. doi:10.1021/nl801396r
- [3] T. ZENTGRAF, J. DORFMÜLLER, C. ROCKSTUHL, C. ETRICH, R. VOGELGESANG, K. KERN, T. PERTSCH, F. LEDERER, H. GIESSEN: ‘Amplitude-and phase-resolved optical near fields of split-ring-resonator-based metamaterials.’ *Opt. Lett.* **33** (8), pp. 848–850, 2008. doi:10.1364/OL.33.000848
- [4] R. VOGELGESANG, J. DORFMÜLLER, R. ESTEBAN, R. T. WEITZ, A. DMITRIEV, K. KERN: ‘Plasmonic nanostructures in aperture-less scanning near-field optical microscopy (aSNOM).’ *Phys. Status Solidi B* **245** (10), pp. 2255–2260, 2008. doi:10.1002/pssb.200879617
- [5] J. DORFMÜLLER, R. VOGELGESANG, R. T. WEITZ, C. ROCKSTUHL, C. ETRICH, T. PERTSCH, F. LEDERER, K. KERN: ‘Fabry-Pérot Resonances in One-Dimensional Plasmonic Nanostructures.’ *Nano Lett.* **9** (6), pp. 2372–2377, 2009. doi:10.1021/nl900900r
- [6] M. MÄDER, T. HÖCHE, J. W. GERLACH, S. PERLT, J. DORFMÜLLER, M. SALIBA, R. VOGELGESANG, K. KERN, B. RAUSCHENBACH: ‘Plasmonic Activity of Large-Area Gold Nanodot Arrays on Arbitrary Substrates.’ *Nano Lett.* **10** (1), pp. 47–51, 2010. doi:10.1021/nl903633z
- [7] C. ROCKSTUHL, C. ETRICH, C. HELGERT, C. MENZEL, T. PAUL, S. FAHR, T. PERTSCH, J. DORFMÜLLER, R. ESTEBAN, W. KHUNSIN, R. VOGELGESANG, K. KERN, A. DMITRIEV, K. BITTKAU, T. BECKERS, R. CARIUS, F. LEDERER: ‘Large scale simulations in the realm of nanooptics.’ *Proc. SPIE* **7604** (76040D), 2010. doi:10.1117/12.841700

- [8] J. DORFMÜLLER, R. VOGELGESANG, W. KHUNSIN, C. ROCKSTUHL, C. ET-RICH, K. KERN: ‘Plasmonic Nanowire Antennas: Experiment, Simulation, and Theory.’ *Nano Lett.* **10** (9), pp. 3596–3603, 2010. doi:10.1021/nl101921y

# Acknowledgements

Although a PhD thesis is written by a single author, there are much more people who contribute to its success. I would like to thank the following people without whom this work would not have been possible:

**Prof. Klaus Kern** for giving me the opportunity to write my PhD thesis in his group at the Max Planck Institute for Solid State Research.

**Dr. Ralf Vogelgesang** for much more than supervising my PhD thesis. His continuous support motivated me, his thorough understanding of diverse physical problems guided my research and his little pushes forward encouraged me to follow my own ideas.

**Prof. Nicolas Grandjean, Prof. Olivier Martin, Prof. Bert Hecht and Dr. Alexander Dmitriev** for agreeing to be part of my PhD jury.

**Dr. Thomas Weitz** for providing me with high quality lithographic samples.

**Dr. Worawut Khunsin** for completing the full angular spectrum needed for the emission patterns and for taking over much of the lab work to enable me to write this thesis.

**Dr. Ruben Esteban**, without whom's work on the aSNOM the success in plasmonic eigenmode imaging would not have been possible.

**Moritz Eblinger** and **Stephanie Essig** for reading early versions of my thesis and telling me where to improve it.

**Marcus Rommel** and **Michael Saliba** for their curiosity that often made me scrutinize my believes.

My office mates **Dr. Stephan Rauschenbach, Dr. Georgios Katsaros, Dr. Cristina Gomez-Navarro, Thomas Dufaux** and **Sören Krotzky**. The mixture of people with diverse research topics and characters always made our office special and encouraged discussions.

My collaborators **Dr. Carsten Rockstuhl, Dr. Alexander Dmitriev, Dr. Christoph Etrich** and **Marisa Mäder**. The successful and long standing collaborations always gave new input to my research.

---

My parents, **Klaus** and **Silvia Dorf Müller**, and my sisters **Gabi Dorf Müller** and **Anne Hilscher** who always supported me in my decisions and encouraged me to find my own way.

My grandmother **Ruth Dorf Müller** for supporting me during my PhD studies.

My girlfriend **Hyeyeon Ryu** for supporting me and for forgiving my many long working hours.

My **dear friends** for their encouragement. Alex Langner, Theresa Lutz, Maximilian Assig, Sören Neubeck, Mike Tannert, Alex Krake, Elisabeth Ohnesorge, Daniela Schimanski, Brigitte Schultz, Martin Göbel, Tobias Weißbach, Alexander Weber. You always reminded me that there are also other things in life that are important.